CDF/ANAL/ELECTROWEAK/CDFR/8668

Direct Measurement of the W Boson Width

Valeria Bartsch, Daniel Beecher, Ilija Bizjak, Mark Lancaster, Sarah Malik, Emily Nurse, Troy Vine, David Waters

University College London, UK

Abstract

The width of the W boson has been directly measured in approximately 350 pb^{-1} of $\mathrm{p\bar{p}}$ data at $\sqrt{s} = 1.96$ TeV collected by the CDF II detector. The measurement, performed in both electron and muon decay channels, relies on a fit to the tail of the transverse mass distribution in order to extract the width of the W boson Breit-Wigner resonance lineshape. The techniques employed to simulate the signal, estimate the backgrounds and extract the width are presented in detail in this note. The resulting direct measurement of the W width, combining both decay channels, is 2032 ± 73 MeV.

Contents

1 Introduction

The width of the W boson, Γ_W, is a fundamental parameter of the Standard Model, within which it is predicted to be 2091 $\pm$ 2 MeV [1]. Measuring Γ_W provides a test of this prediction, deviations of which suggest non-Standard Model W decay modes. In addition, an uncertainty in Γ_W translates to an uncertainty in the measured W mass, M_W. We describe in this note a direct measurement of Γ_W from a fit to the W transverse mass (M_T) distribution in the high M_T tail. The measurement is made in both the W $\rightarrow \mu\nu$ and W $\rightarrow$ eν decay channels since they both provide clean experimental signatures. The neutrino is not detected in CDF, thus its momentum cannot be measured. The neutrino transverse momentum is found by summing the transverse energy, $E_T = E \times \sin\theta$, of the calorimeter towers and measuring the missing transverse energy, $\not{E}_T$. The transverse mass is then found by:

$$M_T = \sqrt{2p_T^\ell \not{E}_T[1 - \cos(\phi_\ell - \phi_\nu)]}, \tag{1}$$

where ${p_T}^\ell$ is the transverse momentum of the charged lepton and ϕ_ℓ and ϕ_ν are the azimuthal angles of the lepton and $\not{E}_T$ respectively. A Monte Carlo event generator is used to create M_T templates with different Γ_W input values which are used to fit to the M_T distributions in the data. The templates are normalised to the data in the region $50 < M_T < M_T^{\mathrm{cut}}$ GeV and the fit is performed in the region $M_T^{\mathrm{cut}} < M_T < 200$ GeV, where M_T^{cut} is optimised to give the smallest total uncertainty.

It is necessary to simulate the interaction of the generated final state particles in the CDF detector. A dedicated fast simulation has been developed for this analysis, utilising both Z $\rightarrow \ell^+\ell^-$ control samples and the full CDF simulation (CdfSim) to tune the detector response to particles.

The layout of the note is as follows. Firstly the candidate event selection is described. Then the Monte Carlo generator is introduced and the simulation of the CDF detector and its response to particles is explained. Backgrounds in the data samples are then addressed and lastly the results of the Γ_W fits are given and the uncertainties are summarised.

Each of the above effects lead to systematic uncertainties on Γ_W. Unless otherwise stated the systematic uncertainty from each effect is found using the Monte Carlo. A Monte Carlo 'data' M_T histogram is created with everything set to its default value. Templates are then created with the effect in question varying within its uncertainty. The templates are fitted to the Monte Carlo 'data' plot and the shift in the fitted Γ_W value compared to the inputted value is taken as a systematic uncertainty on Γ_W. The uncertainty for each effect is given for five values of M_T^{cut}: 80, 85, 90, 100 and 110 GeV.

2 Event Selection

Four data samples are selected: W $\rightarrow \mu\nu$ and W $\rightarrow$ eν events to make the Γ_W measurement and Z $\rightarrow \mu^+\mu^-$ and Z $\rightarrow e^+e^-$ events to calibrate the detector. The W and Z bosons have large masses (80.41 and 91.187 GeV respectively [1]) and thus their decay products tend to have a large p_T. W bosons are identified by an electron or muon with large p_T and a large $\not\!\!E_T$ (due to the neutrino) and Z events are identified by a high p_T $\mu^+\mu^-$ or e$^+$e$^-$ pair. The event selection for the four samples is described in detail in the following.

2.1 Muon Channel

Z $\rightarrow \mu^+\mu^-$ events are selected by requiring one 'tight' muon, identified in the central trackers, the calorimeter and the muon chambers and one 'loose' muon, identified in the central trackers and calorimeter only. The requirements of a 'loose' muon are listed in Table 1. A 'tight' muon must satisfy all the 'loose' requirements as well as the additional requirements listed in Table 2. The muon cut variables and why they are used in the event selection are described in the following.

- p_T^{BC}: Transverse momentum of the beam-constrained muon track reconstructed with COT hits only. Suppresses background.
- z_0: Track impact parameter in z. Ensures tracks are in a well instrumented region of the detector.
- silicon hits: If the run is marked as 'good' for the silicon detector, the track is required to have silicon hits. Suppresses decay in-flight background (since the efficiency of silicon hits in decay in-flight tracks is very low). The silicon hits are not used in the construction of p_T^{BC}.
- $\mathrm{N}_{\mathrm{seg}}^{\mathrm{axial}}$: Number of axial COT super-layers. Ensures good quality tracks and suppresses decay in-flight background.
- $\mathrm{N}_{\mathrm{seg}}^{\mathrm{stereo}}$: Number of stereo COT super-layers. Ensures good quality tracks and suppresses decay in-flight background.
- $\mathrm{N}_{\mathrm{hits}}^{\mathrm{axial1}}$: Number of hits in the 1st axial COT super-layer. Suppresses decay in-flight background.
- $\mathrm{R}_{\mathrm{COT}}$: COT exit radius. Ensures that the track and muon stub are in a well instrumented region of the detector.
- d_0: Track impact parameter in $r - \phi$. Suppresses decay in-flight background.

- χ^2_{track}/dof: Track fit χ^2. Suppresses decay in-flight background.
- E_{em}: Energy in the electromagnetic calorimeter. Suppresses multi-jet background.
- E_{had}: Energy in the hadronic calorimeter. Suppresses multi-jet background.
- CMP dx: Track-stub matching in the CMP. Suppresses decay in-flight background. Trigger cut.
- CMU dx: Track-stub matching in the CMU. Suppresses decay in-flight background. Trigger cut.
- CMX dx: Track-stub matching in the CMX. Suppresses decay in-flight background. Trigger cut.
- Fiducial: Defined in Section 5. Ensures muon stub is in a well instrumented region of the detector.

In addition to the two muons the event selection criteria listed in Table 3 are also required for $Z \to \mu^+\mu^-$ events. $W \to \mu\nu$ events are selected by requiring one 'tight' muon as well as the additional criteria listed in Table 4. The event cut variables and why they are used in the event selection are described in the following.

- $M_{\ell\ell}$: The di-lepton invariant mass. Suppresses background.
- Recoil: The vector sum of the energy in the calorimeter towers (described in detail in Section 11). Suppresses multi-jet background. Selects events with better $\not{E}_T$ resolution.
- $\not{E}_T$: The missing transverse energy in the detector, due to the neutrino. Suppresses background.
- M_T: The transverse mass. Suppresses background.

The 'Z veto' is designed to reject Z events from the W sample. For muons it is a veto on any other track in the event with:

- $p_T > 20$ GeV.
- $|\Delta z_0| < 5$ cm, where Δz_0 is the distance in z between the muon track and the other track.
- COT hits.
- either:

– $\Sigma_{cone0.4}(p_T) < 2$ GeV or
– $\Sigma_{cone0.4}(p_T) < 10$ GeV and $E_{\mathrm{em}} < 2$ GeV and $E_{\mathrm{had}} < 5.6 + 0.014 \times p_T$ GeV

where the track isolation variable, $\Sigma_{cone0.4}(p_T)$, is the sum p_T of tracks within a cone of $\Delta R < 0.4$ and within $|\Delta z_0| < 5$ cm of the muon track. The effect of the Z veto on Γ_W is investigated with CdfSim and is found to be negligible.

A dedicated cosmic tagger [2] is run on the $Z \rightarrow \mu^+\mu^-$ and $W \rightarrow \mu\nu$ events. Starting with a reconstructed 'seed' track the tagger re-fits the hits belonging to this track with the five helix parameters and a floating global time shift. Based on the best fit values an incoming or outgoing hypothesis is assigned to the seed track. The re-fitted seed track is then used to search for hits belonging to the second cosmic leg on the opposite side of the COT. If enough hits are found a similar fit procedure is performed to identify the opposite-side track. If both legs are found, a simultaneous fit is performed to combine all hits from the seed and opposite-side legs into a single helix. The event is tagged as a cosmic if the top(bottom) leg is recognised as incoming(outgoing) and the χ^2 of the simultaneous fit is < 300. The event is also tagged as a cosmic if $|\Sigma\eta_{\mu\mu}| < 0.03$ and $\Delta\phi_{\mu\mu} > 3.13$, where $\Sigma\eta_{\mu\mu}$ is the sum of the two track η values and $\Delta\phi_{\mu\mu}$ is the difference between the track ϕ values, indicating that the two tracks are collinear. The $\Sigma\eta_{\mu\mu}$ and $\Delta\phi_{\mu\mu}$ cuts are simulated in the $Z \rightarrow \mu^+\mu^-$ fast Monte Carlo. The cosmic cuts cannot be simulated in the $W \rightarrow \mu\nu$ fast Monte Carlo but they are simulated with CdfSim and the effect on Γ_W is found to be negligible.

Variable	Cut value	Simulated
p_T^{BC}	> 25 GeV	$\surd$
$\|z_0\|$	< 60 cm	$\surd$
silicon hits	For runs where silicon is 'good'	$\times$
$N_{\mathrm{seg}}^{\mathrm{axial}}$	≥ 3 with ≥ 7 hits	$\times$
$N_{\mathrm{seg}}^{\mathrm{stereo}}$	≥ 3 with ≥ 7 hits	$\times$
$N_{\mathrm{hits}}^{\mathrm{axial1}}$	≥ 5 (no silicon tracks only)	$\times$
R_{COT}	< 137 cm	$\surd$
d_0	$< 0.04(0.2)$ for silicon(no silicon)	$\times$
χ^2_{track}/dof	$< 3(2)$ for silicon(no silicon)	$\times$
E_{em}	< 2 GeV	$\surd$
E_{had}	$< 5.6 + 0.014 \times p_T$ GeV	$\times$

Table 1: Loose muon cuts. The third column indicates whether the cut is simulated.

Variable	Cut value	Simulated
CMUP or CMX stub	present	$\times$
$\lvert$CMP $dx\rvert$	< 6 cm	$\times$
$\lvert$CMU $dx\rvert$	< 3 cm	$\times$
$\lvert$CMX $dx\rvert$	< 5 cm	$\times$
fiducial	true	$\surd$

Table 2: Tight muon cuts. The third column indicates whether the cut is simulated.

Variable	Cut value	Simulated
$M_{\ell\ell}$	> 80 GeV and < 100 GeV	$\surd$
Lepton charge	Opposite sign	$\surd$
Recoil	< 20 GeV	$\surd$

Table 3: Z cuts. The third column indicates whether the cut is simulated.

Variable	Cut value	Simulated
$\not\!\!E_T$	> 25 GeV	$\surd$
M_T	> 50 GeV and < 200 GeV	$\surd$
Recoil	< 20 GeV	$\surd$
Z veto		$\times$

Table 4: W cuts. The third column indicates whether the cut is simulated.

2.2 Electron Channel

Z $\rightarrow e^+e^-$ events are selected by requiring two 'tight' electrons identified in the COT and the calorimeter. The requirements of a 'tight' electron are listed in Table 5. The electron cut variables that were not already defined in the previous section are described in the following.

- E_T: $E \times \sin\theta$, where E is the energy measured in the calorimeter and θ is the polar angle of the electron track. Suppresses background.
- Fiducial:
  - Only select electrons in towers 0-8 as tower 9 is more subject to leakage into the hadronic calorimeter.
  - $|\mathrm{CES}\, z| > 12$ cm, where CES z is the local z coordinate of the calorimeter tower. Avoids the crack in the calorimeter where the two halves meet.
  - $|\mathrm{CES}\, x| < 18$ cm, where CES x is the local x coordinate of the calorimeter tower. Avoids the cracks between calorimeter wedges.

  Ensures that the electron is in a well instrumented region of the detector.
- E/p: The ratio of E_T to p_T^{BC}. Suppresses multi-jet background.
- $\mathrm{E_{had}}/\mathrm{E_{em}}$: The ratio of the hadronic calorimeter energy to the electromagnetic calorimeter energy for the electron cluster. Suppresses multi-jet background.
- L_{shr}: The lateral shower profile for electrons. Compares the energy in calorimeter towers adjacent to the seed tower for data and test beam electrons. Suppresses multi-jet background. Trigger cut.
- Δz: The distance in the $r - z$ plane between the extrapolated COT track and the CES cluster. Suppresses multi-jet background. Trigger cut.
- Δx: The distance in the $r - \phi$ plane between the extrapolated COT track and the CES cluster. Suppresses multi-jet background. Trigger cut.

In addition to the two electrons the event selection criteria listed in Table 3 are also required to pass. W $\rightarrow$ eν events are selected by requiring one 'tight' electron as well as the additional criteria listed in Table 4. The 'Z veto' for electrons is a veto on any other track in the event that satisfies the following criteria:

- $p_T > 20$ GeV

Variable	Cut value	Simulated
E_T	> 25 GeV	$\surd$
$\lvert z_0 \rvert$	< 60 cm	$\surd$
Fiducial	true	$\surd$
E/p	> 0.8 and < 1.3	$\surd$
$\mathrm{E_{had}/E_{em}}$	< 0.07	$\surd$
L_{shr}	< 0.3	$\times$
$\lvert \Delta z \rvert$	< 8 cm	$\times$
$\lvert \Delta x \rvert$	< 10 cm	$\times$
$\mathrm{N_{seg}^{axial}}$	≥ 3 with ≥ 7 hits	$\times$
$\mathrm{N_{seg}^{stereo}}$	≥ 3 with ≥ 7 hit	$\times$

Table 5: Tight electron cuts

- $\Delta z_0 < 5$ cm
- COT hits
- $\Sigma_{cone0.4}(p_T) < 5$ GeV
- Points to an un-instrumented region of the calorimeter: $|\mathrm{CES}\, x| > 18$ cm or $|\mathrm{CES}\, z| < 9$ cm.

The effect of the Z veto on the fitted Γ_W is investigated with CdfSim and is found to be negligible.

The trigger requirements of candidate events are described in Section 5. After all the above described selection criteria we find 6271 Z $\rightarrow \mu^+\mu^-$ and 108,808 W $\rightarrow \mu\nu$ candidate events in 330 pb^{-1} and 2909 Z $\rightarrow e^+e^-$ and 127,432 W $\rightarrow$ eν candidate events in 370 pb^{-1}.

3 Event Generation

W $\rightarrow \mu\nu$, W $\rightarrow$ eν, Z $\rightarrow \mu^+\mu^-$ and Z $\rightarrow e^+e^-$ events are generated with the Toygen [3] Monte Carlo event generator which is interfaced with Parton Distribution Functions (PDFs). Toygen is interfaced with the Berends and Kleiss program [4] which adds up to one photon (real and virtual corrections) from QED radiation from the $W^\pm$ and the final state charged leptons. Initial state photon radiation is ignored. The generated processes are purely electroweak with no QCD corrections. This means that gluon radiation from the incoming quarks is not simulated and the bosons are created with zero p_T. A p_T is then added to the boson as is described in section 3.3.

3.1 Parton Distribution Functions

The momentum distributions of the quarks and gluons inside the proton are required as input for simulation of the Monte Carlo samples. These values can only be approximated and therefore introduce a systematic uncertainty on Γ_W. This is found using the uncertainties of the PDF parameterisations due to the data used to constrain them as well as theoretical uncertainties due to higher order corrections in the PDF evolution. The PDF parameterisations used are CTEQ6 and MRST[5, 6].

CTEQ(MRST) uses 20(15) parameters to describe the parton distribution functions. These are determined by minimising the χ^2 of a global fit to experimental data. The CTEQ(MRST) group has found 20(15) orthogonal parameters which diagonalise the covariance matrix and therefore the total error can be expressed by the error of the single parameters[5, 6]. For each parameter, samples corresponding to $\pm 90\%$ confidence level have been produced using the 40(30) PDF error sets provided by CTEQ(MRST).

Figures 1(a) and 1(b) show the fitted Γ_W value for each PDF error set for CTEQ and MRST respectively. The line is the fitted Γ_W for the nominal PDF set. The plot does not have any error bars because the same events have been generated and re-weighted for each PDF error set.

With the help of this plot the total symmetric error can be calculated with the following equation:

$$\Delta\Gamma_W = 0.5 \times \sqrt{\sum_{i=1}^{N}[\Delta\Gamma_W^{i,\mathrm{up}} - \Delta\Gamma_W^{i,\mathrm{down}}]^2} \tag{2}$$

and the total asymmetric errors can be calculated from the following equations:

$$\Delta\Gamma_W^{\mathrm{up}} = \sqrt{\sum_{i=1}^{N} max[\Delta\Gamma_W^{i,\mathrm{up}}, \Delta\Gamma_W^{i,\mathrm{down}}, 0]^2} \tag{3}$$

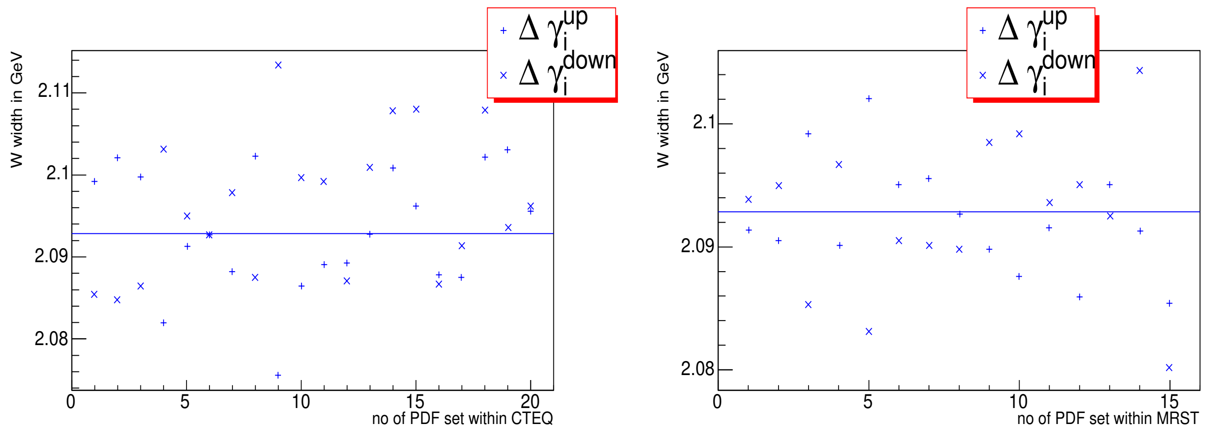

(a) (b)

Figure 1: Fitted Γ_W for the different PDF error sets using 20 million W $\rightarrow \mu\nu$ events with $M_T^{\rm cut}$ = 90 GeV for (a) CTEQ6M and (b) MRST.

$$\Delta\Gamma_W^{i,\rm down} = -\sqrt{\sum_{i=1}^{N} min[\Delta\Gamma_W^{i,\rm up}, \Delta\Gamma_W^{i,\rm down}, 0]^2} \tag{4}$$

The uncertainties on Γ_W are divided by 1.6 in order to give a 1σ uncertainty since the error sets correspond to 2σ variations [7]. The CTEQ and MRST errors are summarised in Table 6 for the different $M_T^{\rm cut}$ values. The MRST errors are consistently lower than the CTEQ values. For this analysis the symmetric CTEQ errors have been used.

$M_T^{\rm cut}$ [GeV]	$\Delta\Gamma_W$: CTEQ						$\Delta\Gamma_W$: MRST	
	electrons			muons			electrons	muons
	$\Delta\Gamma_W^{\rm sym}$	$\Delta\Gamma_W^{\rm up}$	$\Delta\Gamma_W^{\rm down}$	$\Delta\Gamma_W$	$\Delta\Gamma_W^{\rm up}$	$\Delta\Gamma_W^{\rm down}$	$\Delta\Gamma_W^{\rm sym}$	$\Delta\Gamma_W^{\rm sym}$
80	15 MeV	19 MeV	14 MeV	16 MeV	19 MeV	14 MeV	10 MeV	10 MeV
85	17 MeV	21 MeV	17 MeV	18 MeV	21 MeV	16 MeV	12 MeV	12 MeV
90	16 MeV	15 MeV	21 MeV	16 MeV	20 MeV	15 MeV	11 MeV	11 MeV
100	19 MeV	25 MeV	18 MeV	21 MeV	26 MeV	18 MeV	11 MeV	11 MeV
110	24 MeV	30 MeV	21 MeV	25 MeV	31 MeV	22 MeV	13 MeV	13 MeV

Table 6: Systematic uncertainties on Γ_W due to the PDFs.

In addition to the PDF uncertainties from the parameters in the functional forms, theoretical uncertainties from higher orders of perturbation theory are investigated by comparing Γ_W when the NLO and NNLO MRST 2004 PDFs [8] are used. Since the default inputted PDFs are NLO, this shift is included as an additional systematic uncertainty, which is the same for the electron and muon decay channels and is summarised in Table 7 for the different M_T^{cut} values.

M_T^{cut}	$\Delta\Gamma_W^{\mathrm{NNLO}}$
80	14 MeV
85	14 MeV
90	12 MeV
100	10 MeV
110	9 MeV

Table 7: Systematic uncertainties on Γ_W due to higher order corrections in the PDFs.

3.2 Electroweak corrections

3.2.1 QED

Photon radiation from the W propogator and outgoing leptons changes the M_T distribution in W events and the $M_{\ell\ell}$ distribution in Z events. This can lead to a bias on Γ_W due to the direct effect on the M_T distribution and due to shifts in the extracted calorimeter and tracking scales and resolutions. The measurement of the calorimeter and tracking scales and resolutions is described in detail later in Sections 7 and 9.

In this analysis QED is simulated using the Berends and Kleiss program [4] which adds up to one photon (real and virtual corrections) from the $W^{\pm}$ and the final state charged leptons. It is also possible to interface the Toygen generator with the Photos [9] program which treats up to two photons from the final state charged leptons but is accurate in the soft and collinear emission limits only.

Photos is used to estimate the effect of two photon emission on the M_T line-shape and on the calorimeter and tracking scales and resolutions. M_T, $M_{\ell\ell}$ and E/p templates are generated using Photos. They are then fitted to M_T, $M_{\ell\ell}$ and E/p Monte Carlo 'data' distributions from Photos events where two photon events are excluded. Thus we are fitting Photos with up to two photons to Photos with up to one photon, which gives the expected shift due to the second photon.

Table 8 summarises the expected shift in the fitted lepton scales and resolutions due to the second photon. Since the fitted scales and resolutions affect the fitted Γ_W value, these shifts are propagated through to find the expected shift in Γ_W.

Tables 9 and 10 summarise the shift in Γ_W due to the shifts in the fitted lepton scales and resolutions and due to the direct effect on the M_T line-shape from the 1 photon approximation.

Parameter	Shift in fitted value
S^{mom}	-0.00041
S^{res}	+0.019
S^{CEM}[from M_{ee}]	-0.00040
S^{CEM}[from E/p]	0
S^{CEM}[combined]	-0.00013
κ^{uncorr}[from M_{ee}]	+0.075%
κ^{uncorr}[from E/p]	+0.040%
κ^{uncorr}[combined]	+0.048%

Table 8: Shifts in the lepton resolutions and scales due to second order QED corrections.

$M_T^{\rm cut}$ [GeV]	$\Delta\Gamma_W$[fit]	$\Delta\Gamma_W$[S$^{\rm mom}$]	$\Delta\Gamma_W$[S$^{\rm res}$]	$\Delta\Gamma_W$[total]
80	-10 MeV	+28 MeV	-14 MeV	4 MeV
85	-10 MeV	+26 MeV	-13 MeV	3 MeV
90	-7 MeV	+16 MeV	-10 MeV	1 MeV
100	-3 MeV	+7.6 MeV	-5.4 MeV	1 MeV
110	-1 MeV	+4.8 MeV	-2.4 MeV	1 MeV

Table 9: Systematic uncertainties on Γ_W due to QED (muons). $\Delta\Gamma_W$[total] is the vector addition of the preceding columns.

$M_T^{\rm cut}$ [GeV]	$\Delta\Gamma_W$[fit]	$\Delta\Gamma_W$[S$^{\rm CEM}$]	$\Delta\Gamma_W$[$\kappa^{\rm uncorr}$]	$\Delta\Gamma_W$[total]
80	-17 MeV	+9 MeV	-7 MeV	15 MeV
85	-15 MeV	+8 MeV	-6 MeV	13 MeV
90	-9 MeV	+5 MeV	-4 MeV	8 MeV
100	-0.2 MeV	+2 MeV	-1 MeV	1 MeV
110	-2 MeV	+1 MeV	0 MeV	1 MeV

Table 10: Systematic uncertainties on Γ_W due to QED (electrons). $\Delta\Gamma_W$[total] is the vector addition of the preceding columns.

3.2.2 Electroweak box diagrams

The Berends and Kleiss program neglects non-resonant corrections to the $p\bar{p} \to \ell\nu$ process, which arise predominantly from the W/Z box diagrams shown in Figure 2. While these diagrams give a negligible contribution to the cross-section in the peak region, they become non-negligible in the high M_T fit region [10]. In order to investigate the size of the effect on the Γ_W measurement we used the WGRAD program [10], which includes all NLO electroweak corrections and can be run in modes with and without non-resonant contributions. Since including these contributions cause the generator to run extremely slowly we used a very simplified and fast detector model with all kinematic and acceptance cuts, a Gaussian smearing of the lepton momenta and $\not{E}_T$, merging of electrons and photons and the MIP cut in the muon final state. Figure 3 shows the ratio of the M_T distributions with and without the non-resonant corrections included for the electron and muon channels. The effect on the width was found by re-weighting a Monte Carlo "data" M_T histogram by the ratio and fitting to the nominal M_T templates. The final width result is corrected for according to the shift, which is summarised in Table 11 for the different fit regions for electrons and muons. Since the effect depends on the detector resolution, the $\not{E}_T$ smearing was varied such that the simplified detector model matches the fast simulation within error bars, as shown in Figure 4. The variation in the width shift as the $\not{E}_T$ smearing is varied is attributed as a systematic uncertainty and is also shown in Table 11 for the different fit regions.

	Electron channel		Muon channel	
$M_T^{\rm cut}$ [GeV]	Γ_W correction	$\Delta\Gamma_W$	Γ_W correction	$\Delta\Gamma_W$
80	+8 MeV	2 MeV	+11 MeV	2 MeV
85	+10 MeV	5 MeV	+12 MeV	5 MeV
90	+11 MeV	6 MeV	+12 MeV	6 MeV
100	+15 MeV	6 MeV	+17 MeV	6 MeV
110	+20 MeV	6 MeV	+23 MeV	6 MeV

Table 11: The shift in Γ_W due to non-resonant electroweak corrections for the electron and muon decay channels. The uncertainty on the shift comes from varying the $\not{E}_T$ resolution, as described in the text.

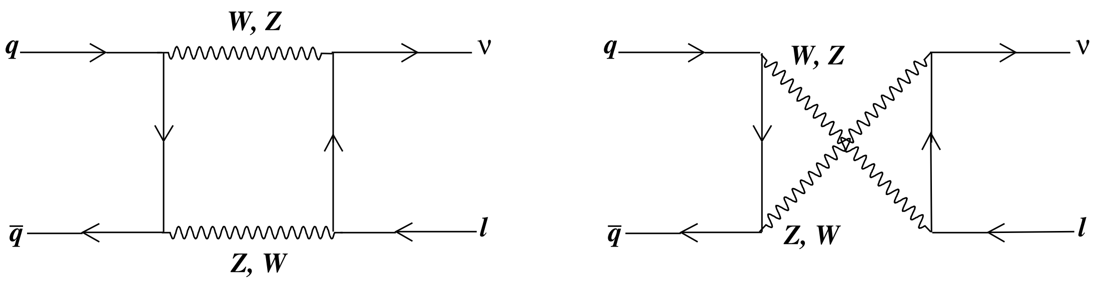

Figure 2: Feynman diagrams for the W,Z box diagrams in the $p\bar{p} \to \ell\nu$ process.

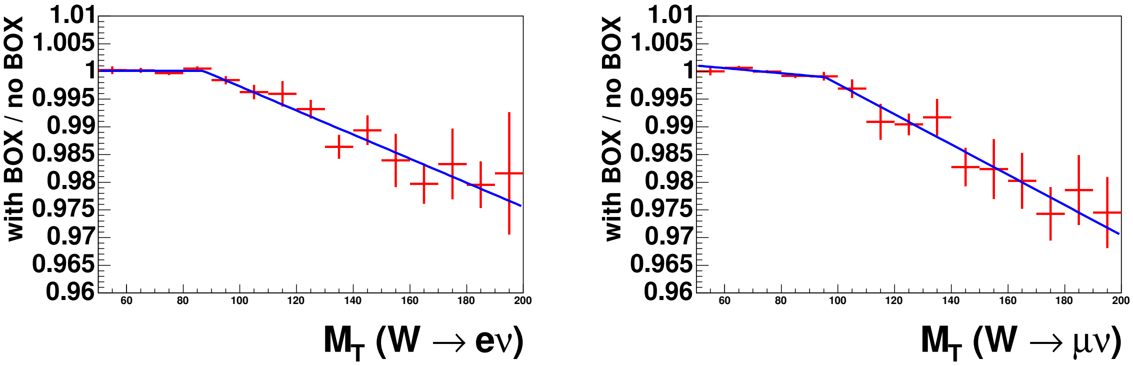

Figure 3: The ratio of the M_T distributions with and with-out the non-resonant contributions for electrons (left) and muons (right).

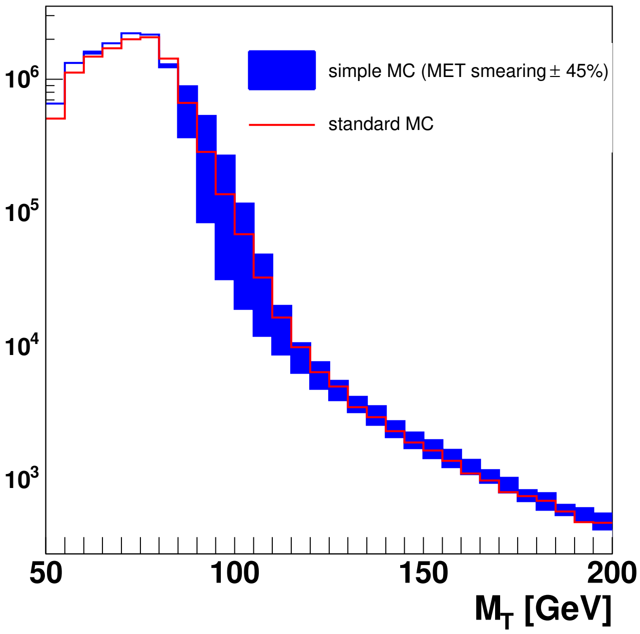

Figure 4: The M_T distribution in the standard simulation compared to that in the simplified simulation. The latter has a variation of the $\not{E}_T$ smearing, indicated by the blue band, to cover the disagreement with the standard simulation in the fit region.

3.3 Determination of W P_T

The W p_T distribution cannot be determined unambiguously from the W data alone since its determination relies on an accurate recoil model which in turn relies on the W p_T distribution. The W p_T distribution is thus generally determined by using the relatively well measured Z p_T distribution and using a theoretical ansatz to go from the Z to W p_T distribution. In general there are two associated theoretical problems : the low p_T region is dominated by the emission of low p_T gluons whose contribution to the cross section is calculated using a resummation technique and which owing to the low p_T of the gluons necessarily has a non-perturbative component. There is no defined prescription for the non-perturbative component and it is generally parameterised as an ad-hoc function whose parameters must be derived from experiment. Depending on the form of the function, some of the non-perturbative parameters can have a reliance on data outside the scope of this analysis and also have a dependence on PDFs. This can clearly make a reliable error estimate difficult owing to the dependency on other datasets. A second problem is presented by the need for the perturbative calculation, valid at high p_T ($p_T \gtrsim$ 20-30 GeV), to match smoothly with the resummed calculation valid at low p_T.

The RESBOS [11] generator is based on a NLO resummed calculation in impact parameter space which uses the so-called BLNY parameterisation [12] to describe the non-perturbative effects at low p_T. The BLNY functional form has 4 free parameters g_1, g_2, g_3 and $b_{\max}$ and an $x_1 x_2$ dependence to control the variation of p_T with $\hat{s}$. The RESBOS authors have performed fits to R209, E288, E605 fixed target Drell-Yan data ($5 < \sqrt{\hat{s}} < 18$ GeV) and also to the DØ run-1B p_T^Z measurements [13] and the CDF run-0 and run-1B p_T^Z measurements [14, 15]. These fits have a χ^2 of 176/260 with g_1, g_2 and g_3 found to be $0.21^{+0.01}_{-0.01}$ GeV^2, $0.68^{+0.01}_{-0.02}$ GeV^2 and $-0.6^{+0.05}_{-0.04}$ respectively.

We have not chosen to use the RESBOS generator directly but a program that computes the same resummed calculation in b-space using the BLNY form. Previous studies [16] have shown that g_2 has the greatest effect on $\frac{d\sigma}{dp_T}$ and can be extracted from data. The effect of g_1 and g_3 is expected to be smaller but cannot readily be extracted from CDF Drell-Yan, requiring a greater range in $\hat{s}$ that one gets from low-energy fixed-target Drell-Yan.

The W p_T distribution and its uncertainty is extracted in the following way:

1. A binary file of event weights and lepton p_T is generated with a high-statistics sample of fast-MC events with the global fit parameters for g_1, g_2 and g_3. Since the resolutions of the muon and electron p_T measurements are different, separate electron and muon binary files are created. These files account for the effects of selection cuts as well as the lepton resolution. This binary file can be re-weighted to produce events with a different choice of initial g_1, g_2 and g_3.

2. We scan the χ^2 of the fits to electrons and muons (we add the χ^2 of the electron and

muon distributions together, since we expect the underlying true p_T^Z distributions to be the same in each case) and fit a parabola to the range of χ^2 to find the minimum. We chose to obtain g_2 from data in this fashion but to use the global fit values of g_1 and g_3. Figure 5 shows the lack of sensitivity of CDF data to g_3, compared with the range set by the BLNY global fit.

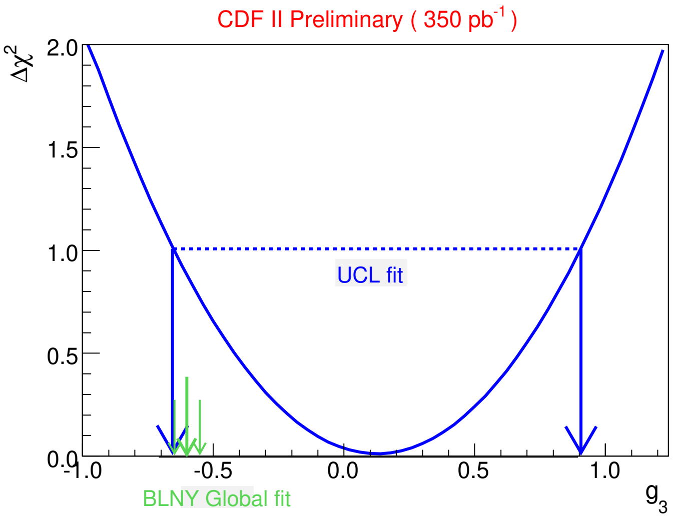

Figure 5: The range of χ^2 from CDF data compared with the BLNY global fit range in g_3.

3. In the MC the p_T^Z function is weighted to allow for the fact that the fit is performed to data averaged over all Z rapidity (mean $|Y| = 0.3$) but events need to be generated differential in both p_T and rapidity. This weighting function is taken from a theoretical calculation of $\frac{d\sigma}{dp_T}(Y = 0.3)/\frac{d^2\sigma}{dY\,dp_T}(Y = Y)$.

4. In the MC the p_T^Z distribution differential in p_T, rapidity and $\hat{s}$ is re-weighted to a p_T^W distribution differential in p_T and rapidity using a theoretical calculation of $\frac{d^3\sigma}{dY\,dp_T d\hat{S}}(W)/\frac{d^2\sigma}{dY\,dp_T}(Z)$.

The p_T^W distribution thus depends on the p_T^Z fits, the Z rapidity weighting function calculation and the W/Z p_T ratio calculation. This method has very small theoretical uncertainties, which can be readily evaluated. The ratio of W/Z p_T is far better known than either of the individual p_T distributions [17, 18] with a very weak dependence on the shape of the individual distributions and similarly the Z rapidity weighting function has only a very weak PDF dependence.

The best fit measured p_T distributions for both the $\mathrm{Z} \rightarrow e^+e^-$ and the $\mathrm{Z} \rightarrow \mu^+\mu^-$ samples are shown in Figure 6.

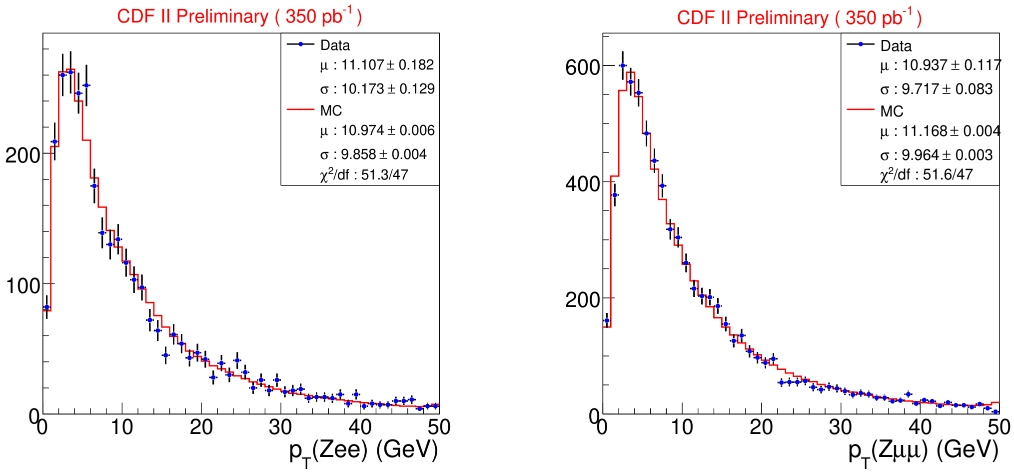

(a) $\mathrm{Z} \rightarrow e^+e^-$

(b) $\mathrm{Z} \rightarrow \mu^+\mu^-$

Figure 6: The measured P_T^Z distributions compared to the best-fit “smeared” MC prediction.

The best fit values of g_2 when fitting to either $\mathrm{Z} \rightarrow e^+e^-$ (0.62 ± 0.08 GeV^2) or $\mathrm{Z} \rightarrow \mu^+\mu^-$ (0.68 ± 0.05 GeV^2) data are compatible with one another; therefore, we add the χ^2 of both distributions and fit for a single value of g_2. We found this to be 0.660 ± 0.042 GeV^2. The χ^2 of the fits are compatible and are outlined in Table 12.

	g_2	χ^2_{e}	χ^2_{μ}	$\chi^2_{\mathrm{e}+\mu}$
g_2^{e}	0.62	50.8/48	52.6/48	103.4/96
$g_2^{\mathrm{e}+\mu}$	0.66	51.3/48	51.6/48	102.9/96
g_2^{μ}	0.68	51.7/48	51.4/48	103.1/96

Table 12: The χ^2 fits of g_2^{e}, g_2^{μ} and $g_2^{\mathrm{e}+\mu}$ to $\mathrm{Z} \rightarrow e^+e^-$ and $\mathrm{Z} \rightarrow \mu^+\mu^-$ data.

Since the BLNY parameters only affect the non-perturbative region of the p_T distribution their uncertainty may not capture the entire uncertainty which would arise from the finite Z statistics. Therefore, when estimating the uncertainty, we introduce a linear distortion function :

$$f\left(B, p_T\right) = 1 + B \times p_T \ ,$$

which is applied to the p_T distribution so that :

$$\left(\frac{d\sigma}{dp_T}\right)_{\text{total}} = \left(\frac{d\sigma}{dp_T}\right)_{\text{RESBOS}} \times f(B, p_T).$$

We perform a two-dimensional fit for g_2 and B, the best fit parameters and covariance matrix are : g_2= 0.64 GeV^2, B = -1.4 $\times$ 10^{-3} GeV^{-1},

$$\begin{pmatrix} 0.044^2 & -1.38 \times 10^{-7} \\ -1.38 \times 10^{-7} & 0.001^2 \end{pmatrix}.$$

The g_2 used for evaluating the systematic is compatible with $g_2^{\mathrm{e}+\mu}$ used in the simulation and the distortion factor, B, is compatible with zero. Figure 7 shows the samplings of the g_2-B covariance matrix with the 1σ and 2σ contours, and has the BLNY global fit value of g_2 superimposed.

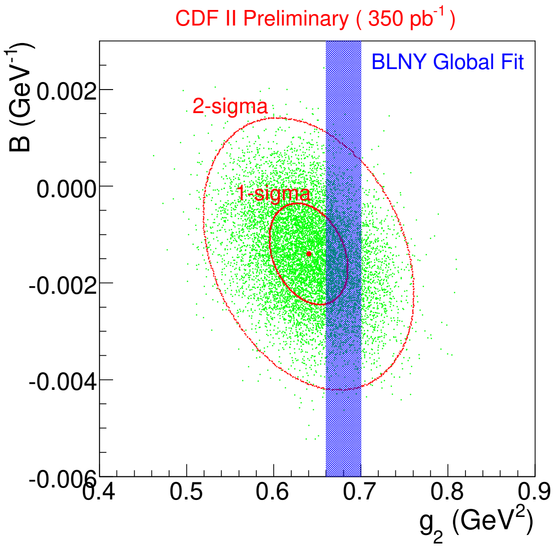

Figure 7: Samplings of the g_2-B covariance matrix, the 1σ and 2σ contours, and the BLNY global fit value of g_2 superimposed.

We sample the covariance matrix a number of times to obtain different generator level p_T distributions arising from the finite Z statistics. For each of the p_T distributions obtained from the covariance matrix, we create a re-weighting function in p_T which can transform an event generated with the nominal Monte Carlo to one generated with the alternative p_T distribution. A M_T distribution is produced for each alternative p_T

distribution. We fit for Γ_W with templates using the nominal MC to each of the M_T distributions. A Gaussian fit to the shifts in the fitted Γ_W from the nominal value is taken to be the systematic effect, $\Delta\Gamma_W^{g_2,B}$.

We vary the BLNY global fit g_1 and g_3 by one σ_{BLNY} at 95% confidence and fit to the nominal Monte Carlo. The error in the three BLNY global fit parameters [11] was estimated by defining a $(\chi^2_{\mathrm{bestfit}} + 1)$ ellipsoid; thus, we scale σ_{g_1} and σ_{g_3} by $\sqrt{7.82}$ to obtain the uncertainty corresponding to the BLNY global fit uncertainty in g_1 and g_3 at 95% confidence. We generate four new p_T distributions by sequentially lowering and raising a parameter to the extent of its error: $(g_1 + \sigma_{g_1},\, g_2,\, g_3)$, $(g_1 - \sigma_{g_1},\, g_2,\, g_3)$, $(g_1,\, g_2,\, g_3 + \sigma_{g_3})$ and $(g_1,\, g_2,\, g_3 - \sigma_{g_3})$. We use the ratio of these p_T distributions to the nominal distribution to re-weight Monte Carlo transverse mass templates differential in Γ_W, and fit to nominal Monte Carlo pseudo-data. The shift of the fitted Γ_W from the nominal value is taken to be the systematic effects from g_1 and g_3, $\Delta\Gamma_W^{g_1}$ and $\Delta\Gamma_W^{g_3}$.

We assume the independence of g_1, g_2-B and g_3 and add in quadrature. $\Delta\Gamma_W$ was found to be 100% correlated between the two decay channels and we assign one systematic for the channels combined.

The second component of the p_T^W systematic arises from uncertainties in the Z-rapidity and W/Z p_T weighting functions. The first function, accounting for the rapidity dependence of the p_T^Z distribution, is obtained using a calculation of the ratio : $\frac{d\sigma}{dp_T}(Y = 0.3)/\frac{d\sigma}{dp_T}(Y = Y_i)$ performed at 20 Y_i values and is stored to yield a bin-by-bin re-weighting function differential in p_T and Y. The PDF dependence of a similar function was investigated in run-1 [16] using a variation in PDFs larger than is now compatible with the latest fits. The effect on the width is < 1 MeV and is neglected.

The second weighting function, converting p_T^Z to p_T^W, is obtained in an analogous way but using the calculated ratio: $\frac{d^2\sigma}{dp_T d\hat{S}}(W)[Y = Y_i]/\frac{d\sigma}{dp_T}(Z)[Y = Y_i]$ instead at the 20 Y_i and 32 $\sqrt{\hat{s}_i}$ values. Examples of the different $\frac{d\sigma}{dp_T}$ are shown in Figure 8.

Three possible effects which might cause the p_T^Z to p_T^W ratio to change were investigated in [16]. The PDF dependence, the calculation mode (impact parameter space vs p_T space), and the form of the non-perturbative function. The maximum shift in the width observed was 1.5 MeV.

The impact of α_s on the p_T^Z to p_T^W ratio was investigated by re-weighting the nominal Monte Carlo to the p_T^Z to p_T^W ratio obtained from the MRS-R1 PDF set where the predominant difference from our Monte Carlo is the change in α_s. p_T distributions for various values of g_2 were generated using MRS-R1 and compared with the nominal p_T description of Z bosons at the generator level in our Monte Carlo; a g_2 of 0.85 gave the closest description. The p_T^Z to p_T^W ratio using this g_2 was evaluated for MRS-R1 and ratio of the two ratios was used to re-weight the Monte Carlo and generate transverse mass pseudo-data. We fit nominal transverse mass distributions differential in Γ_W to the

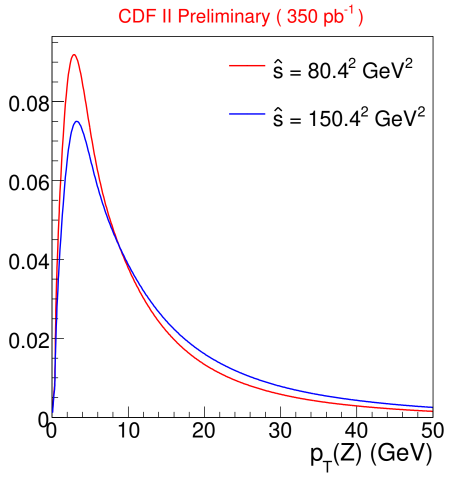

Figure 8: Examples of $\frac{d\sigma}{dp_T}$ for two different values of $\hat{s}$.

pseudo-data and shift in Γ_W observed was less than 1 MeV.

A conservative systematic of 2 MeV from the weighting functions is thus added in quadrature to that arising from the uncertainty in the fits to Z data.

The final p_T^W systematic when we add the Z fit error and the weighting functions errors in quadrature is shown in Table 13 for various M_T fit regions. This error is 100% correlated between the two channels.

$M_T^{\rm cut}$ [GeV]	$\Delta\Gamma_{\rm W}^{\rm g_1}$	$\Delta\Gamma_{\rm W}^{\rm g_2,B}$	$\Delta\Gamma_{\rm W}^{\rm g_3}$	$\Delta\Gamma_{\rm W}^{\rm other}$	$\Delta\Gamma_{\rm W}$[total]
80	2 MeV	7 MeV	2 MeV	2 MeV	8 MeV
85	2 MeV	7 MeV	2 MeV	2 MeV	8 MeV
90	2 MeV	6 MeV	2 MeV	2 MeV	7 MeV
100	2 MeV	6 MeV	2 MeV	2 MeV	7 MeV
110	2 MeV	5 MeV	2 MeV	2 MeV	6 MeV

Table 13: The p_T^W systematic for three transverse mass cuts. This error is 100% correlated between the two channels.

4 Simulation

Generator level electrons, muons and photons are propagated from an event z_0, distributed according to the data [19]. The material description up to and including the COT inner can is taken from `SiliMap` [20], with the particle interactions described below simulated in each of the 32 `SiliMap` radial layers. Beyond that, relevant particle interactions in the detector are either parameterised based on the results of running the full `GEANT-3` based detector simulation CdfSim, or else taken directly from the data as described.

4.1 Muon Interactions

The dominant energy loss mechanism for muons is ionisation. The standard Bethe-Bloch equation works well for muons in the energy range under consideration [21] :

$$-\frac{dE}{dx} = \frac{K}{\beta^2}\left[\frac{1}{2}\ln\frac{2m_ec^2\beta^2\gamma^2T_{max}}{I^2} - \beta^2 - \frac{\delta}{2}\right] ,$$

where the overall constant factor K and the ionisation potential I are provided for each material layer by `SiliMap`. The full expression for the maximum kinetic energy transfer T_{max} is used [22] :

$$T_{max} = \frac{2m_ec^2\beta^2\gamma^2}{1 + 2\gamma m_e/m_\mu + (m_e/m_\mu)^2} .$$

The density effect correction δ is calculated using Sternheimer's parameterisation assuming that the material traversed is silicon [23].

Ionisation energy loss by muons in the COT is neglected. The energy deposited in the calorimeter towers traversed by the muon is not calculated from first principles, but taken from a parameterisation of cosmic ray data. An underlying event energy is added to the muon calorimeter cut as well as the energy of QED photons that end up in the same tower as the muon. The $\mathrm{E_{em}}$ cut of 2 GeV is simulated.

4.2 Electron Interactions

The most important energy loss mechanism for electrons in the inner tracker material is Bremsstrahlung. The probability for photon radiation in a material layer is given by [24] :

$$P_\gamma = dX_0 \times \frac{4}{3}\left[\ln(y_{max}/y_{min}) - (y_{max} - y_{min}) + \frac{3}{8}(y_{max} - y_{min})^2\right] ,$$

where $y_{min} = 0.001$ and $y_{max} = 1.0$ are the minimum and maximum fraction of the electron's energy transferred to the radiated photon respectively. The fractional radiation length traversed, dX_0, is provided by `SiliMap`. The radiation lengths are scaled by a global factor, $S^{\rm mat}$, obtained by fitting the simulation to the E/p distribution in W $\rightarrow$ eν data, as described in Section 8. A radiated photon is drawn from the y distribution [25] :

$$\frac{d\sigma}{dy} \sim \frac{1}{y}\left(\frac{4}{3} - \frac{4y}{3} + y^2\right) .$$

Bremsstrahlung by electrons in the COT is much less important and is treated somewhat differently. The average energy lost through Bremsstrahlung in the first half of the COT ($40.58 < r < 88.038$ cm) is measured in CdfSim for 40 GeV electrons at $|\eta| = 0$, and applied to electrons in the fast simulation. Energy losses further out in the COT will have a very small impact on the measured electron track p_T.

Ionisation energy loss by electrons is also simulated. The approach taken is basically identical to that described in [26], although using the same value for the density effect correction parameter δ as described above for muons. Ionisation energy loss by electrons in the COT is neglected.

Electrons exiting the COT will lose energy in the Time-of-Flight (ToF) detector and the solenoid. The energy entering the CEM is a fraction of the incident energy and is distributed between electrons, positrons and photons differently as a function of the incident particle energy. This collection of particles deposits most of its energy in the active volume of the CEM, but loses a certain fraction through leakage into the rear hadronic compartment. In general there may be correlations between the energy lost in the ToF/solenoid and the leakage fraction. We simulate this for each electron leaving the COT by drawing from an energy-dependent distribution of CEM-deposited energy fractions derived from CdfSim, illustrated in Figure 9. This models the fluctuations as well as the mean energy loss.

4.3 Photon Interactions

The most important process to simulate for photons in the inner tracker material is pair production. We use the high energy limit for the photon conversion probability in a thin material layer [27] :

$$P_{e^+e^-} = (7/9)dX_0 ,$$

where the fractional radiation length traversed, dX_0, is again provided by `SiliMap`. The radiation lengths are scaled by a global factor, $S^{\rm mat}$, obtained by fitting the simulation to the E/p distribution in W $\rightarrow$ eν data, as described in Section 8. The conversion electron energy fraction x is distributed according to [28] :

$$\frac{d\sigma}{dx} \sim 1 - \frac{4}{3}x(1-x) .$$

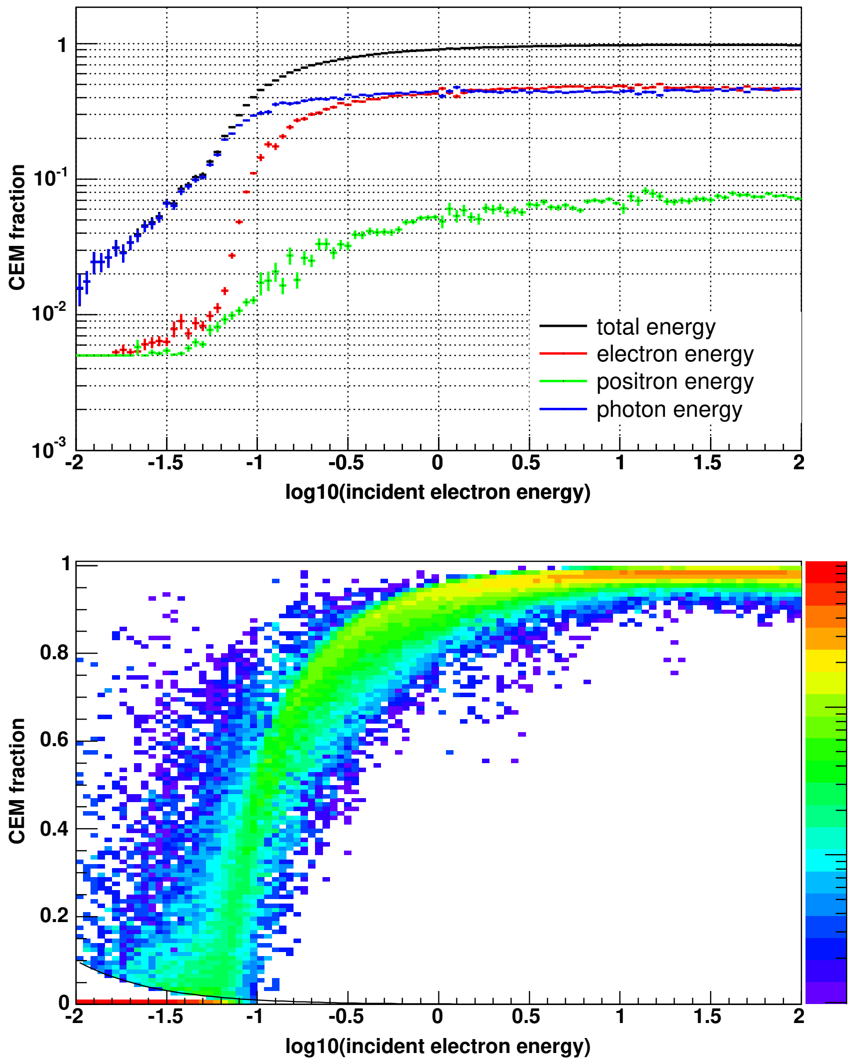

Figure 9: Top: the energy fraction deposited in the CEM as a function of the incident electron energy. At high energies the deposited energy fraction approaches $\sim 98\%$, split roughly equally between electrons and photons. At low energies the incident electron is almost completely absorbed in the ToF and solenoid; the only energy reaching the CEM is in the form of radiated photons. Bottom: the distribution of visible energy fractions, sampled in the fast simulation for each electron exiting the COT. The curve in the bottom left of the plot depicts a deposited energy of 1 MeV, the resolution of CdfSim.

Photon conversions in the COT gas are currently not simulated.

Photon energy loss in the ToF/solenoid and leakage into the CHA is modelled using the same technique described above for electrons. The distribution of CEM-deposited energy fractions derived from CdfSim for photons is illustrated in Figure 10.

4.4 Calorimeter Simulation

Electron, positron and photon energies are allocated to towers according to the CEM geometry. Particles falling in the central crack ($|z| < 4.2$ cm) or Φ cracks ($|x| > 23.1$ cm) do not deposit visible energy [29]. After taking into account energy losses in the ToF detector and the solenoid, as well as longitudinal energy leakage and CEM nonlinearity (see Section 10), the energy of each individual particle is added to the tower sum. The CDF clustering algorithm is simulated and the corresponding 2-tower energy sum defines the measured electron energy (after simulating the calorimeter response and resolution, as described in Section 9). A two-tower underlying event energy is also added to the simulated cluster energy. The highest-p_T fiducial track matching the cluster, regardless of whether or not it corresponds to the original generator level electron, defines the track properties of the simulation reconstructed electron.

4.5 Simulation of the $\mathrm{E_{had}/E_{em}}$ Cut

The electron $\mathrm{E_{had}/E_{em}}$ cut is simulated by keeping track of the energy leakage into the hadronic calorimeter. This energy is scaled by 0.8 which is the response of the hadronic calorimeter [30]. The energy, E, is smeared by

$$\frac{\sigma_E}{E} = 20\%/\sqrt{E}$$

since this value provides a reasonable description of the $\mathrm{E_{had}/E_{em}}$ distribution. Figure 11 shows the $\mathrm{E_{had}/E_{em}}$ distribution in the fast simulation and the data in $\mathrm{Z} \rightarrow e^+e^-$ events.

4.6 Simulation Systematic Uncertainty

The fast simulation proceeds iteratively, up to a user-defined number of iterations. By default the simulation runs up to 2 iterations, which means that Bremsstrahlung photons are allowed to convert, but Bremsstrahlung from the resulting conversion electrons is not simulated. In special simulation runs we have run up to 3 and 4 iterations, and we find a maximum shift in the fitted width value of 8 MeV.

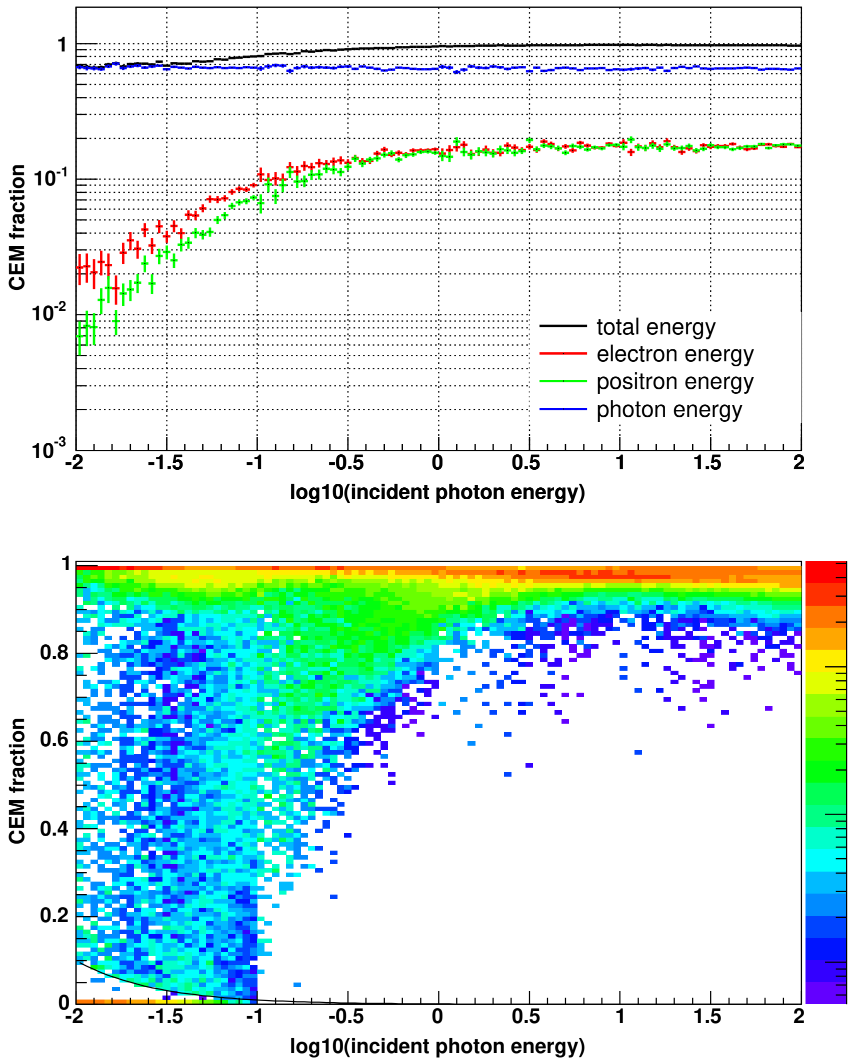

Figure 10: Top: the energy fraction deposited in the CEM as a function of the incident photon energy. At high energies the deposited energy fraction approaches $\sim 98\%$. The fraction never drops below 70% at all energies due to the fraction of photons that traverse the ToF and coil without converting. Bottom: the distribution of visible energy fractions, sampled in the fast simulation for each photon exiting the COT. The distribution is very broad at low energies, with converted photons losing a large fraction of their energy before entering the CEM.

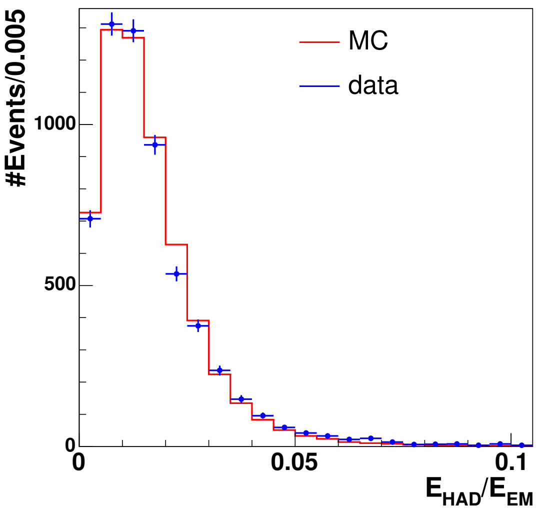

Figure 11: The $\mathrm{E_{had}/E_{em}}$ distribution in $\mathrm{Z} \to e^+e^-$ events in the fast simulation and the data.

As discussed above, the Bremsstrahlung emission spectrum covers the fixed range $0.001 < y < 1.0$ in our simulation. In fact, at low photon energies the spectrum experiences an energy-dependent cut-off due to the Migdal effect at $y_{\rm min}^{\rm LPM} \sim E^e/E^{\rm LPM}$, where E^e is the incident electron energy and $E^{\rm LPM} = 72$ TeV for silicon [31]. Therefore for the bulk of electrons from W decay with an energy of ~ 40 GeV, $y_{\rm min}$ is approximately 0.0006 while for 100 GeV electrons at high transverse mass, $y_{\rm min}$ increases to 0.0014. In order to investigate the effect of not modelling in detail this Migdal suppression, we generate separate simulation samples with a fixed $y_{\rm min}$ spanning the range $[0.0005 \to 0.002]$. We find at most an 8 MeV shift in the fitted width with respect to the default simulation.

For low energy photons, Compton scattering starts to become an appreciable fraction of the total interaction cross section. In silicon, the Compton scattering cross section rises from $\sim 10\%$ of the total at 100 MeV to $\sim 60\%$ at 10 MeV. Our default simulation neglects Compton scattering and assumes a flat conversion cross section for all photon energies. In order to check this assumption, we have performed special simulation runs in which we substitute Compton scattering for pair production for a fraction $F(E^\gamma)$ of photon interactions. $F(E^\gamma)$ is taken from cross section data for photons on silicon [32]. The Compton scattered photon emerges with a fraction, y_C, of its incident energy. We define the y_C distribution to be the high energy limit of the Klein-Nishina formula, $d\sigma/dy_C \propto 1/y_C{+}y$, and sample down to the kinematic limit $y_C^{\rm min} = 1/(1{+}2E^\gamma/m_e)$ [33]. Cross-fitting samples generated with and without Compton scattering included generates a 7 MeV shift in the fitted W width.

Combining these three uncertainties, we arrive at a 13 MeV systematic due to the details of our electron simulation. Note that this may be an overestimate, since our various tuned parameters (notably the material scale, the energy scale and the nonlinearity) may be absorbing much of the residual difference between our default simulation and the data.

5 Acceptances and Efficiencies

The lepton kinematic distributions are sculpted by requiring candidate leptons to be selected from 'well behaved' instrumented regions. This is modelled by extrapolating the trajectory of the lepton through the simulated geometrical volume of the detector to determine if such a region is traversed. Leptons meeting this requirement are considered fiducial. Additionally, the efficiency of a fiducial lepton being selected as a candidate varies from region to region. These efficiencies are measured in the data using

$$\epsilon = \frac{N_{pass}}{N_{total}} \tag{5}$$

with the estimated binomial uncertainty given by

$$\sigma_\epsilon = \sqrt{\frac{\epsilon(1-\epsilon)}{N_{total}}} \tag{6}$$

where N_{pass} is the number of leptons in a subset of a sample of N_{total} leptons where the subset is formed by selecting leptons that pass the requirement for which the efficiency is being measured.

5.1 Lepton Trigger Path Selection

Candidate events are selected so that at least one candidate lepton has passed a trigger path listed in Table 14. The efficiency of the trigger path is measured and used in the simulation.

`ELECTRON_CENTRAL_18`
`MUON_CMX18`
`MUON_CMUP18`

Table 14: Trigger path of candidate leptons (version information omitted).

5.2 Electron Trigger Efficiency

For W $\rightarrow e\nu$ and Z $\rightarrow e^+e^-$ event selection, at least one electron candidate is required to have passed the `ELECTRON_CENTRAL_18` trigger path. The efficiency of this trigger path varies with the electron candidate kinematics. Most W $\rightarrow e\nu$ candidate events have also passed the `W_NOTRACK` trigger path, as it has the same calorimetry requirements on the electron as `ELECTRON_CENTRAL_18` but does not require an associated track. The sample of events that meet all requirements when the required trigger path is `W_NOTRACK` and the subset that have additionally passed the `ELECTRON_CENTRAL_18` trigger path are used, together with Equation 5, to get the efficiency of finding the track in the `ELECTRON_CENTRAL_18` trigger path.

Of the 125,818 candidate events that pass the `W_NOTRACK` trigger path, 121,825 have additionally passed the `ELECTRON_CENTRAL_18` trigger.

The efficiency is measured as a function of the pseudo-rapidity. The tracks are reconstructed from COT hits only and are required to pass through the $p\bar{p}$ interaction point (beam-constrained). The efficiency as a function of track pseudo-rapidity, η_{trk}, can be parameterised as

$$\epsilon(\eta_{trk}) = a_0 + a_1 e^{-\eta^2/2\sigma_1^2} + a_2 e^{-\eta^2/2\sigma_2^2} \tag{7}$$

From the fit to data in bins of η_{trk}, shown in Figure 12, the best fit values of the parameters are shown in Table 15.

Coefficient	Value
a_0	0.988
a_1	-0.100
a_2	0.080
σ_1	0.266
σ_2	0.102

Table 15: Coefficients for fit to efficiency as a function of η_{trk}

It is shown in [34] that there is a 'turn-on' curve for the trigger efficiency for electron transverse energy below 30 GeV due to the Level-2 calorimeter requirements ([35] finds that there is no Level-1 or Level-3 dependence on transverse energy). This is parameterised using

$$\epsilon(E_T) = 0.9988 - 3319.0 \cdot \exp(-0.5512 \cdot E_T) \tag{8}$$

The systematic uncertainty for this approach is estimated by taking the shift in the width value from having a flat efficiency and using the above curve.

5.3 Muon Acceptance

The geometrical acceptance of the candidate muons are determined using the `MuonFiducialTool`, which extrapolates a helix through a full simulation of the muon drift chambers. The three muon sub-systems span two pseudo-rapidity ranges with the CMP chamber behind the centrally located CMU chamber and the CMX chamber located more forward. Candidate muons are therefore considered fiducial if they have both the CMU

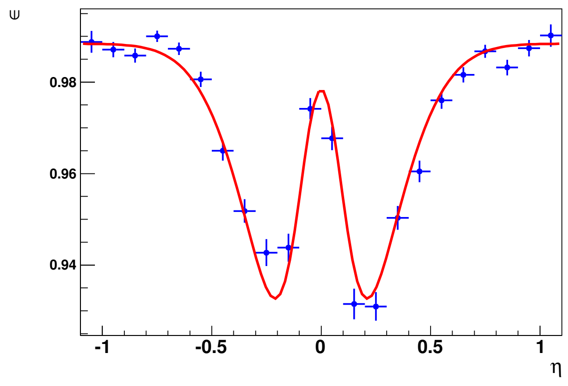

Figure 12: Trigger efficiency as a function of electron η_{trk}.

and the CMP requirements satisfied or the CMX requirement as shown in Table 16. For this analysis, the Bluebeam, Miniskirt and Keystone regions are excluded.

Chamber	x-fid	z-fid
CMX	$<$ 0 cm	$<$ -3 cm
CMP	$<$ 0 cm	$<$ -3 cm
CMU	$<$ 0 cm	$<$ 0 cm

Table 16: Shortest distance of fiducial candidates from instrumented region

5.4 Muon Trigger Efficiencies

Muon candidates must have passed at least one of the `MUON_CMX18` and `MUON_CMUP18` trigger paths. The efficiency of each trigger path can be measured in $Z \to \mu^+\mu^-$candidate events by selecting events containing two tight muons, where one is fiducial in the CMX chamber and the other in the CMUP. The trigger efficiency is then obtained, using Equations 5 and 6, from the sample that has further passed the other trigger path to the one being measured and the subset that have passed both.

It is found that 985 events pass both triggers, 1102 pass `MUON_CMX18` and 1014 passed `MUON_CMUP18`. Table 17 shows the efficiencies obtained. The method used here is different from that used elsewhere as the information from Level-1 is not included. It is shown in [36] that both methods give consistent measurements, and the results found here are in agreement with those presented elsewhere, for example in [37] which uses a similar run range and in [38] which uses an integrated luminosity of 1030 pb^{-1}.

Trigger path	Efficiency	Uncertainty
`MUON_CMX18`	0.971	0.005
`MUON_CMUP18`	0.894	0.009

Table 17: Muon trigger efficiencies

5.5 Muon Reconstruction Efficiencies

The efficiency of the muons leaving a detectable track, or 'stub', in the muon drift chambers matched with a COT track, as defined in Table 2, is measured in $Z \rightarrow \mu^+\mu^-$ candidate events for the CMX and CMUP sub-detectors. For events that have two fiducial muons in the sub-detector being measured, each muon with a stub is selected as a trigger leg. From the sample comprising the other muon in the event, the test leg, and the subset which meet the stub requirement, the reconstruction efficiency is obtained using Equations 5 and 6. The results are shown in Table 18 and are consistent with measurements made in [37].

Muon chamber	N_{pass}	N_{total}	Efficiency	Uncertainty
CMX	792	802	0.988	0.004
CMUP	2082	2394	0.870	0.007

Table 18: Muon stub efficiencies

5.6 Electron Track Hit Efficiency

The hit efficiency for electron track selection is measured in $W \rightarrow e\nu$ events. Using a sample of electrons selected without any track hit requirements and the subset for which the track hit requirements are met, the track hit efficiency is obtained using Equation 5. This is shown in Figure 13(a) as a function of pseudo-rapidity and is fitted with Equation 7 with the fit parameters given in Table 19.

5.7 Muon Track Hit Efficiency

The muon track hit selection efficiency is taken from $Z \rightarrow \mu^+\mu^-$candidate events as, unlike $W \rightarrow \mu\nu$ events, removing the track hit requirement will not bias the measurement due

Coefficient	Value
a_0	0.957
a_1	-3.000
a_2	2.991
σ_1	0.393
σ_2	0.395

Table 19: Coefficients for electron track hit efficiency fit.

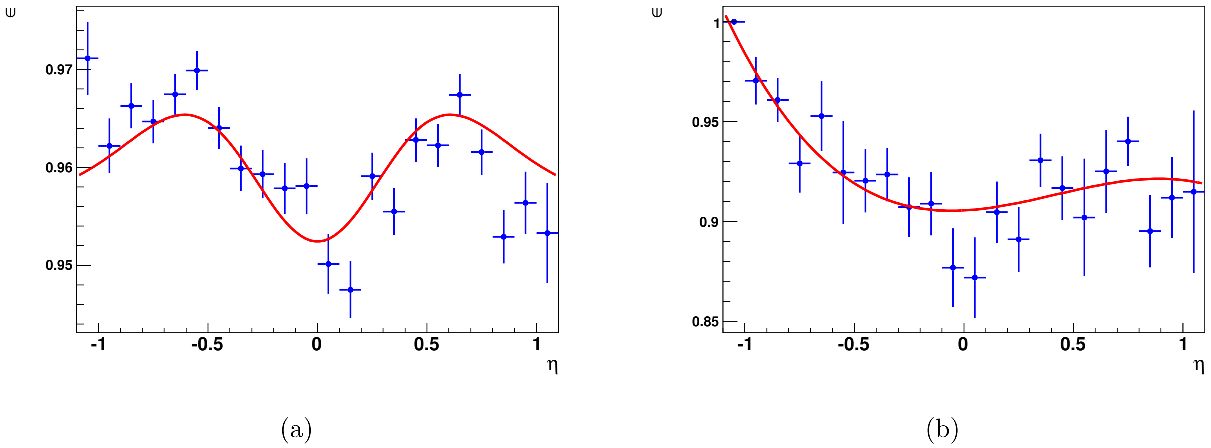

Figure 13: The fitted (a) electron and (b) muon hit efficiency as a function of η_{trk}.

to increased decay in-flight background contamination. The efficiency is obtained using 'tight' muons as trigger legs, and then selecting a sample of 'test' legs that meet all requirements except the track hit requirement and the subset that further meet the track hit requirement. The results, using Equations 5 and 6, are shown in Figure 13(b) fitted with a third order polynomial. The coefficients from the fit are shown in Table 20.

Coefficient	Value
p_0	0.907
p_1	0.013
p_2	0.047
p_3	-0.047

Table 20: Coefficients for muon track hit efficiency fit.

5.8 Electron Kinematic Systematic

Using the method and efficiencies described above, the electron η and ϕ distributions shown, compared to the data, in Figure 14 are obtained. The error bars shown are the statistical uncertainties only. To estimate the uncertainty on the width due to the method used to simulate the detector acceptance and efficiencies, Monte Carlo pseudo-data is re-weighted and the shift in the fitted width due to the re-weighting is taken as the systematic uncertainty. The templates and the different re-weighted pseudo-data are generated in the same job to remove shifts in the fitted width due to statistical fluctuations. For η and ϕ, the Monte Carlo is re-weighted so that the distributions, binned as shown in Figure 14, are identical to the data. For the trigger efficiency with transverse energy distribution, the difference between the flat hypothesis and the efficiency curve given by Equation 8, which is the default used to generate the templates, is taken as the systematic uncertainty. The results are the same for all M_T^{cut} values and are summarised in Table 21. The combined value is obtained by adding the individual values in quadrature.

systematic:	$\Delta\Gamma_{\mathrm{W}}$
$\Delta\Gamma_W[\eta]$	3 MeV
$\Delta\Gamma_W[\phi]$	1 MeV
$\Delta\Gamma_W[E_T]$	1 MeV
$\Delta\Gamma_W[\text{total}]$	3 MeV

Table 21: Electron systematic uncertainty on the width for all fit regions.

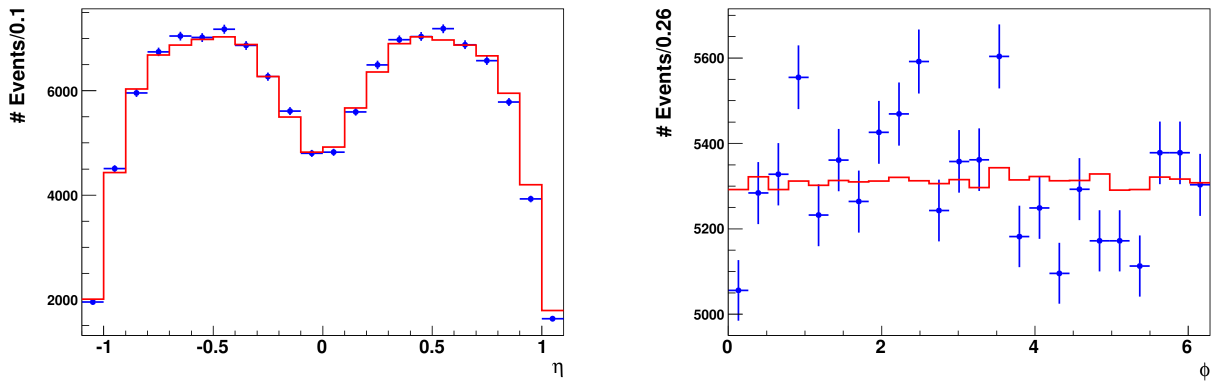

(a) (b)

Figure 14: The electron (a) pseudo-rapidity and (b) azimuthal distribution.

5.9 Muon Kinematic Systematic

Using the same method as for the electrons, the distributions shown in Figure 15 are re-weighted and the shift on the width is determined. The results are summarised for the different M_T^{cut} values in Table 22.

M_T^{cut} [GeV]	$\Delta\Gamma_W[\eta]$	$\Delta\Gamma_W[\phi]$	$\Delta\Gamma_W$[total]
80	2 MeV	3 MeV	4 MeV
85	2 MeV	3 MeV	4 MeV
90	2 MeV	3 MeV	4 MeV
100	3 MeV	3 MeV	4 MeV
110	3 MeV	3 MeV	4 MeV

Table 22: Muon systematic uncertainty on the width.

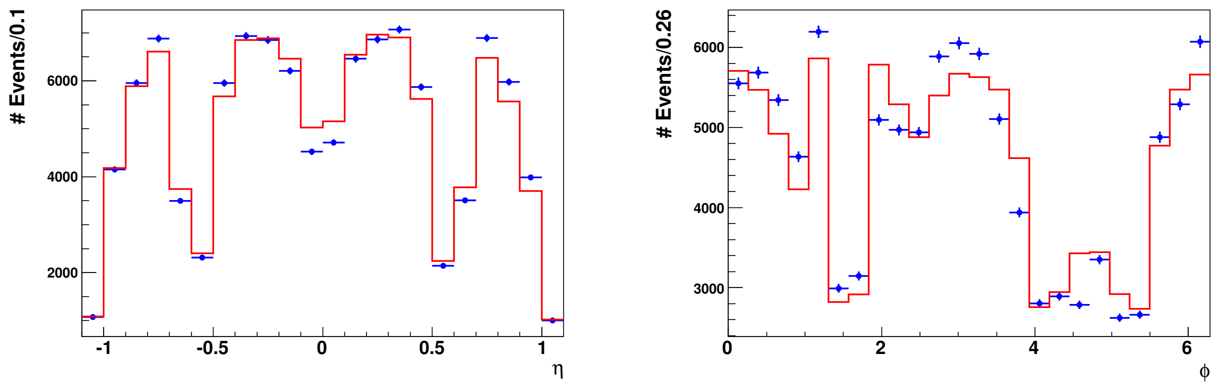

(a)

(b)

Figure 15: The muon (a) pseudo-rapidity and (b) azimuthal distribution.

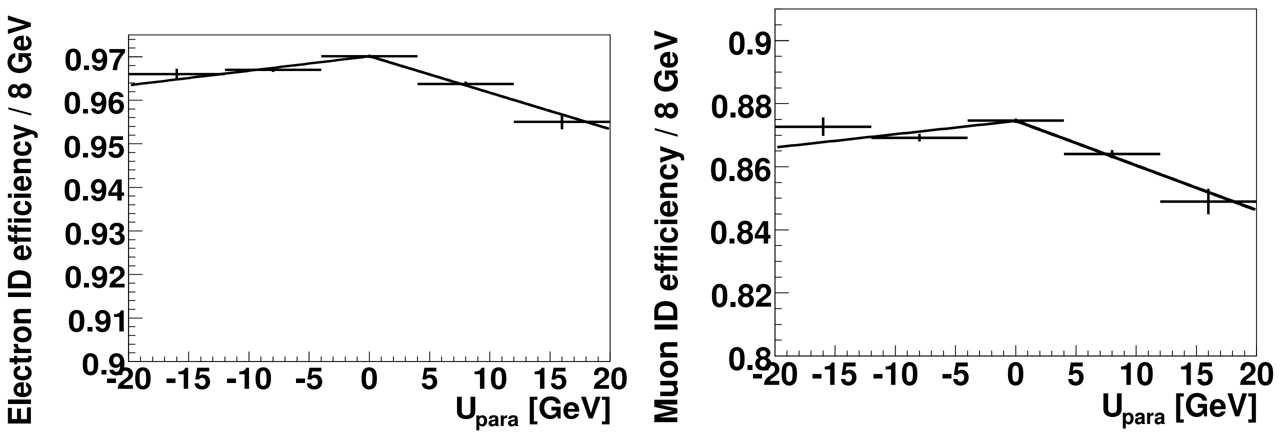

(a)

(b)

Figure 16: (a) The electron identification efficiency as a function of $U_{||}$. (b) The muon identification efficiency as a function of $U_{||}$.

6 Lepton Identification Efficiencies

The efficiency of the lepton identification cuts can vary as a function of kinematic variables. For cuts that we do not simulate this can bias the M_T distribution in the data. The following section considers variations in the efficiencies as a function of $U_{||}$ and lepton p_T. The identification variables included in the efficiency measurement for electrons are: $\mathrm{E_{had}/E_{em}}$, L_{shr}, Δz, Δx, $\mathrm{N_{seg}^{axial}}$and $\mathrm{N_{seg}^{stereo}}$. The identification variables included in the efficiency measurement for muons are: silicon hits, $\mathrm{N_{seg}^{axial}}$, $\mathrm{N_{seg}^{stereo}}$, $\mathrm{N_{hits}^{axial1}}$, d_0, χ^2_{track}/dof and $\mathrm{E_{had}}$.

6.1 Lepton Identification Efficiencies Versus $U_{||}$

The more activity in the event the less efficient the cuts are, in particular if the activity is in the direction of the lepton. The efficiencies are measured in CdfSim as a function of $U_{||}$ and input into the fast simulation. Figure 16 shows the measured efficiency for electrons and muons.

The efficiency, $\epsilon_{\mathrm{ID}}(U_{||})$, is parameterised as:

$$\epsilon_{\mathrm{ID}}(U_{||}) = 1 + (\mathrm{A} \times U_{||}) : \text{for } U_{||} < 0 \text{ GeV} \tag{9}$$

$$\epsilon_{\mathrm{ID}}(U_{||}) = 1 + (\mathrm{B} \times U_{||}) : \text{for } U_{||} > 0 \text{ GeV.} \tag{10}$$

where $\epsilon_{\rm ID}(U_{||})$ has been set to 1 at 0 GeV to maximise the event generation efficiency. Table 23 summarises the values obtained for A and B for electrons and muons using W CdfSim, Z CdfSim and Z data. The values obtained from W CdfSim are used in the simulation. The values obtained from Z CdfSim and Z data are consistent with each other and the statistical limitation of this consistency check is taken as a systematic uncertainty on the values obtained from W CdfSim. The shift in Γ_W obtained by varying these parameters is summarised in Table 24.

	A ($\times 10^{-4}$)	B ($\times 10^{-4}$)
Z $\rightarrow e^+e^-$ data	7.1 ± 7.8	-5.6 ± 8.6
Z $\rightarrow e^+e^-$ CdfSim	5.5 ± 1.6	-8.6 ± 1.8
W $\rightarrow$ eν CdfSim	$3.4 \pm 1.0_{\rm STAT} \pm 3.7_{\rm SYST}$	$-8.7 \pm 4.6_{\rm STAT} \pm 13.4_{\rm SYST}$
Z $\rightarrow \mu^+\mu^-$ data	2.6 ± 8.0	-26.0 ± 9.3
Z $\rightarrow \mu^+\mu^-$ CdfSim	1.3 ± 1.4	-17.2 ± 1.8
W $\rightarrow \mu\nu$ CdfSim	$4.8 \pm 2.9_{\rm STAT} \pm 14.8_{\rm SYST}$	$-16.0 \pm 5.8_{\rm STAT} \pm 5.7_{\rm SYST}$

Table 23: Fitted parameter values obtained for the $\epsilon_{\rm ID}$ efficiency versus $U_{||}$.

$M_T^{\rm cut}$ [GeV]	$\Delta\Gamma_W$: electrons	$\Delta\Gamma_W$: muons
80	2 MeV	7 MeV
85	2 MeV	7 MeV
90	2 MeV	6 MeV
100	1 MeV	2 MeV
110	0 MeV	1 MeV

Table 24: Systematic uncertainties on Γ_W due to $\epsilon_{\rm ID}(U_{||})$.

6.2 Lepton Identification Efficiencies Versus p_T

Some lepton identification variables may depend on the energy of the lepton. Figure 17(a) shows the efficiency of the electron identification cuts as a function of E_T in the region $25 < E_T < 75$ GeV measured in W $\rightarrow$ eν CdfSim. All of the above cuts but $\rm E_{had}/E_{em}$ are included, since the E_T dependence of $\rm E_{had}/E_{em}$ is modelled in our simulation. Figure 17(b) shows the efficiency in the region $50 < E_T < 100$ GeV measured in RS Graviton CdfSim, generated with a mass between 100 GeV and 950 GeV [39]. W $\rightarrow$ eν CdfSim cannot be used as there are not enough events in the region $E_T > 60$ GeV. The L_{shr}, Δz and Δx cuts are included in this efficiency. The electron identification efficiency is parameterised

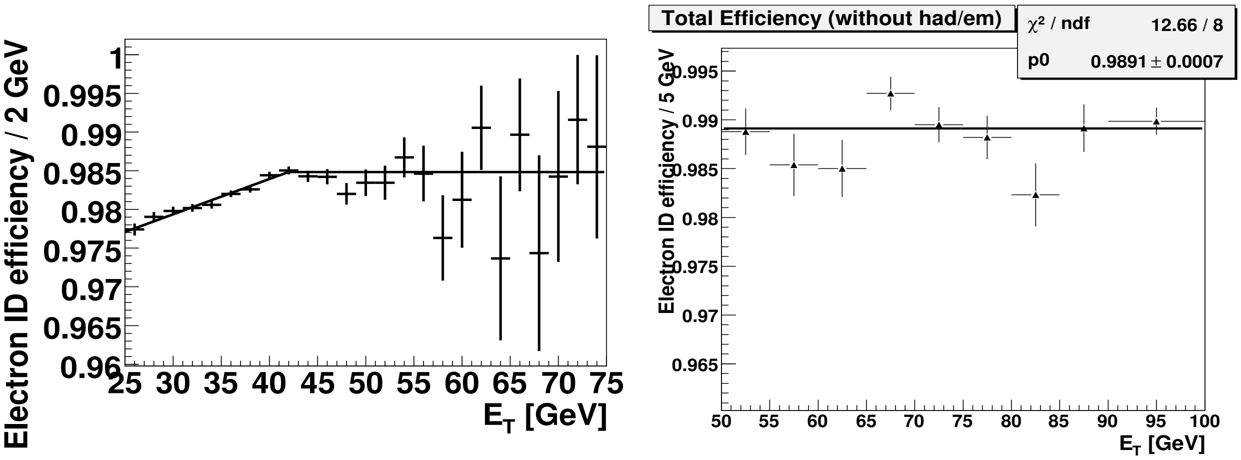

(a) (b)

Figure 17: The electron identification efficiency as a function of E_T in (a) the low E_T region (obtained from W $\rightarrow$ eν CdfSim) and (b) the high E_T region (obtained from RS Graviton CdfSim [39]).

as:

$$\epsilon_{\mathrm{ID}}(E_T) = \mathrm{C} + (\mathrm{D} \times E_T) : \text{for } E_T < 42.0 \text{ GeV} \tag{11}$$

$$\epsilon_{\mathrm{ID}}(E_T) = 1.0 : \text{for } E_T > 42.0 \text{ GeV} \tag{12}$$

and input into the fast simulation. Table 25 summarises the values obtained for D (which is the relevant parameter for the efficiency variation) using W CdfSim, Z CdfSim and Z data (for the Z fits the pivot point in the parameterisation is 48.0 GeV due to the larger mass of the Z boson). The values obtained from W CdfSim are used in the simulation. The values obtained from Z CdfSim and Z data are consistent with each other and the statistical limitation of this consistency check is taken as a systematic uncertainty on the values obtained from W CdfSim. The shift in Γ_W obtained by varying these parameters is summarised in Table 26 at the end of this section.

	D $\times 10^{-4}$
Z $\rightarrow e^+e^-$ data	7.1 ± 5.6
Z $\rightarrow e^+e^-$ CdfSim	7.2 ± 0.1
W $\rightarrow$ eν CdfSim	$4.6 \pm 0.4_{\mathrm{STAT}} \pm 3.6_{\mathrm{SYST}}$

Table 25: Fitted parameter values obtained for the ϵ_{ID} efficiency versus E_T.

As mentioned above, the E_{had}/E_{em} cut efficiency was not included in the parameterisation since its E_T dependence is assumed to be modelled in the fast simulation. In order to see if this assumption is valid Figure 18(a) shows the efficiency as a function of E_T in the region $25 < E_T < 75$ GeV measured in the fast simulation compared to that measured in the data and in CdfSim for W $\rightarrow e\nu$ events. Compared to CdfSim and the data the fast simulation under-estimates the increase in the efficiency in the region $E_T > 35$ GeV. The following scale factor is applied to the efficiency in the fast simulation in order to bring the distributions into agreement:

$$S_{hadem} = 0.9964 : \text{ for } E_T < 39.0 \text{ GeV} \tag{13}$$

$$S_{hadem} = 0.9964 + 0.0036 \times (E_T - 39.0) : \text{ for } 39.0 < E_T < 40.0 \text{ GeV} \tag{14}$$

$$S_{hadem} = 1.0 : \text{ for } E_T > 40.0 \text{ GeV} \tag{15}$$

The green histogram in Figure 18(a) shows the efficiency in the fast simulation after applying this scale factor. The scale factor is applied as a weight to the default fast simulation and the resulting shift in the the fitted Γ_W is taken as a systematic uncertainty. The shifts in Γ_W are summarised in Table 26.

Figure 18(b) shows the E_{had}/E_{em} efficiency in the region $50 < E_T < 100$ GeV measured in the fast simulation compared to that measured in RS Graviton CdfSim. The CdfSim distribution falls off faster than the fast simulation. Both distributions are fitted with a first order polynomial. The ratio between the fitted functions is applied as a weight to the fast simulation and the resulting shift in the the fitted Γ_W is taken as a systematic uncertainty. The default simulation has no weight applied in the high E_T region. The shifts in Γ_W are summarised in Table 26.

M_T^{cut} [GeV]	$\Delta\Gamma_W[\epsilon_{ID}]$	$\Delta\Gamma_W[S_{hadem}$: low $E_T]$	$\Delta\Gamma_W[S_{hadem}$: high $E_T]$	$\Delta\Gamma_W$[total]
80	6 MeV	12 MeV	1 MeV	13 MeV
85	6 MeV	12 MeV	1 MeV	13 MeV
90	4 MeV	9 MeV	1 MeV	10 MeV
100	3 MeV	7 MeV	2 MeV	8 MeV
110	3 MeV	7 MeV	3 MeV	8 MeV

Table 26: Systematic uncertainties on Γ_W due to $\epsilon_{ID}(E_T)$ in electrons.

Figure 19(a) shows the muon identification efficiency to be flat as a function of muon p_T in W $\rightarrow \mu\nu$ CdfSim. The cut $E_{had} < 5.6 + 0.014 \times p_T$ GeV, is specifically chosen to be p_T independent. This p_T dependent form was chosen by fitting the $< E_{had} >$ versus p_T distribution in W $\rightarrow \mu\nu$ CdfSim to a first order polynomial, as shown in Figure 19(b). The slope parameter has an 8% error. Varying the form of the E_{had} cut to reflect this error gives a 1 MeV shift in the fitted Γ_W for all fit ranges.

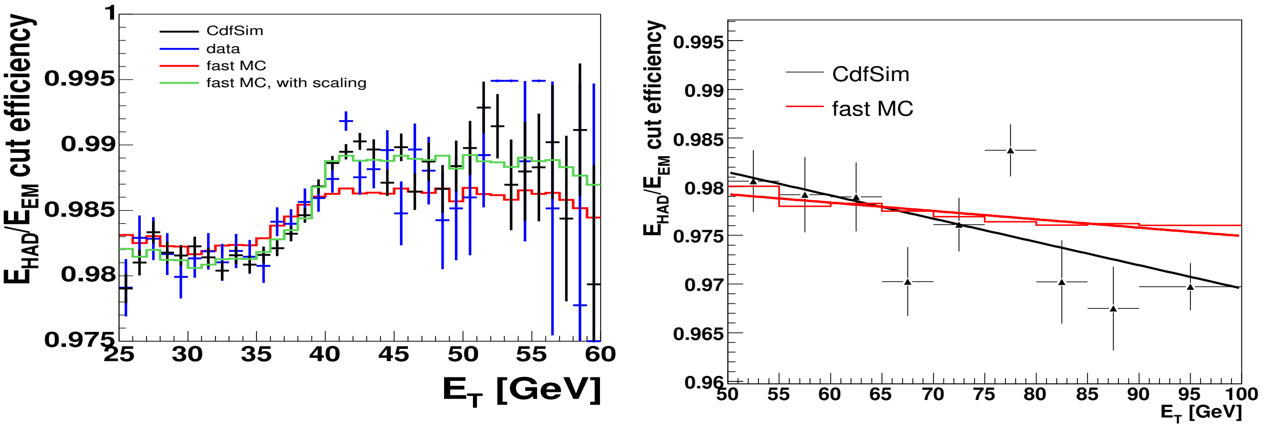

(a) (b)

Figure 18: The E_{had}/E_{em} cut efficiency as a function of E_T. The distributions have been scaled such that the average efficiency matches that in CdfSim since it is only the shape of the distribution that is important. (a) In the low E_T region for data, CdfSim and the fast Monte Carlo (the CdfSim distribution comes from $W \rightarrow e\nu$ Monte Carlo). The green histogram shows the efficiency measured in the fast simulation with the scale factor, S_{hadem}, applied as discussed in the text. (b) In the high E_T region for CdfSim and the fast Monte Carlo (the CdfSim distribution comes from RS Graviton CdfSim [39]). Both distributions have been fitted with a first order polynomial.

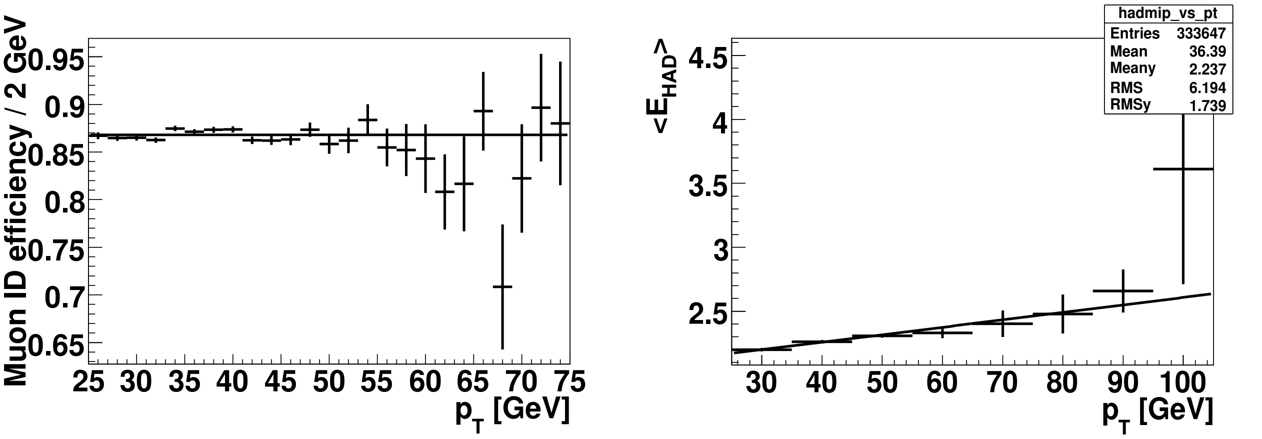

(a) (b)

Figure 19: (a) The muon identification efficiency as a function of p_T. (b) $<\mathrm{E}_{\mathrm{had}}>$ as a function of p_T.

7 Lepton Momentum Scales and Resolutions

The momentum of the charged leptons is measured in the COT. The fast simulation returns the true momenta of the leptons which must be smeared so that it resembles that measured in the data. The momenta will also need to be scaled due to inaccuracy of the magnetic field and the lepton energy loss model in the simulation.

W $\rightarrow \mu\nu$ CdfSim events are used to get the $\Delta\rho$ distribution of lepton tracks. Here $\Delta\rho$ is defined as $(\frac{q}{p_T})_{\mathrm{g}en} - (\frac{q}{p_T})_{\mathrm{r}econ}$, where $(\frac{q}{p_T})_{\mathrm{g}en}$ is the generator level charge over transverse momentum and $(\frac{q}{p_T})_{\mathrm{r}econ}$ is the reconstruction level charge over transverse momentum. The events used to obtain this distribution pass all the event selection criteria other than the M_T and muon track p_T cuts. The distribution is found separately for tracks with:

- Four $\mathrm{N}_{\mathrm{seg}}^{\mathrm{axial}}$ and four $\mathrm{N}_{\mathrm{seg}}^{\mathrm{stereo}}$ with at least 7 hits each.
- Four $\mathrm{N}_{\mathrm{seg}}^{\mathrm{axial}}$ and three $\mathrm{N}_{\mathrm{seg}}^{\mathrm{stereo}}$ with at least 7 hits each.
- Three $\mathrm{N}_{\mathrm{seg}}^{\mathrm{axial}}$ and four $\mathrm{N}_{\mathrm{seg}}^{\mathrm{stereo}}$ with at least 7 hits each.
- Three $\mathrm{N}_{\mathrm{seg}}^{\mathrm{axial}}$ and three $\mathrm{N}_{\mathrm{seg}}^{\mathrm{stereo}}$ with at least 7 hits each.

These distributions are shown in Figure 20. For each lepton track in the fast simulation the distribution of $\mathrm{N}_{\mathrm{seg}}^{\mathrm{axial}}$ and $\mathrm{N}_{\mathrm{seg}}^{\mathrm{stereo}}$ (taken from the Z $\rightarrow \mu^+\mu^-$ data) is sampled, putting the track in one of the four categories above. Then the appropriate $\Delta\rho$ distribution is sampled in order to obtain $\Delta\rho$ of the track. $\Delta\rho$ is then multiplied by a constant factor, $\mathrm{S}^{\mathrm{res}}$, the value of which is found by fitting the $M_{\mu\mu}$ distribution in Z $\rightarrow \mu^+\mu^-$ events in the simulation to that in the data. The momenta are then smeared as follows:

$$(\frac{q}{p_T})_{\mathrm{r}econ} = (\frac{q}{p_T})_{\mathrm{g}en} + (\mathrm{S}^{\mathrm{res}} \times \Delta\rho) \tag{16}$$

with $\mathrm{S}^{\mathrm{res}} = 1.100 \pm 0.039$ (i.e. the data requires 10% more smearing than CdfSim). The momenta are scaled by a multiplicative factor $\mathrm{S}^{\mathrm{mom}} = 0.99891 \pm 0.00043$ which is also found by fitting to $M_{\mu\mu}$. Figure 21 shows the best fitting Monte Carlo template and the data.

The track parameters ϕ and $\cot(\theta)$ are smeared with a Gaussian distribution with $\sigma_\phi = 0.002$ and $\sigma_{\cot(\theta)} = 0.011$, taken from $\phi_{\mathrm{g}en}$ - $\phi_{\mathrm{r}econ}$ and $\cot(\theta)_{gen}$ - $\cot(\theta)_{recon}$ distributions in CdfSim.

The uncertainty on Γ_W due to the uncertainty on the momentum scale and resolution is found by generating a Monte Carlo M_T distribution using the best fit scale and smear parameters and M_T templates with the parameters varying individually by -4σ,-2σ, 2σ and 4σ from their best fit values. The 1σ uncertainty in interpolated from this distribution. Table 27 summarises the obtained uncertainties for different fit regions.

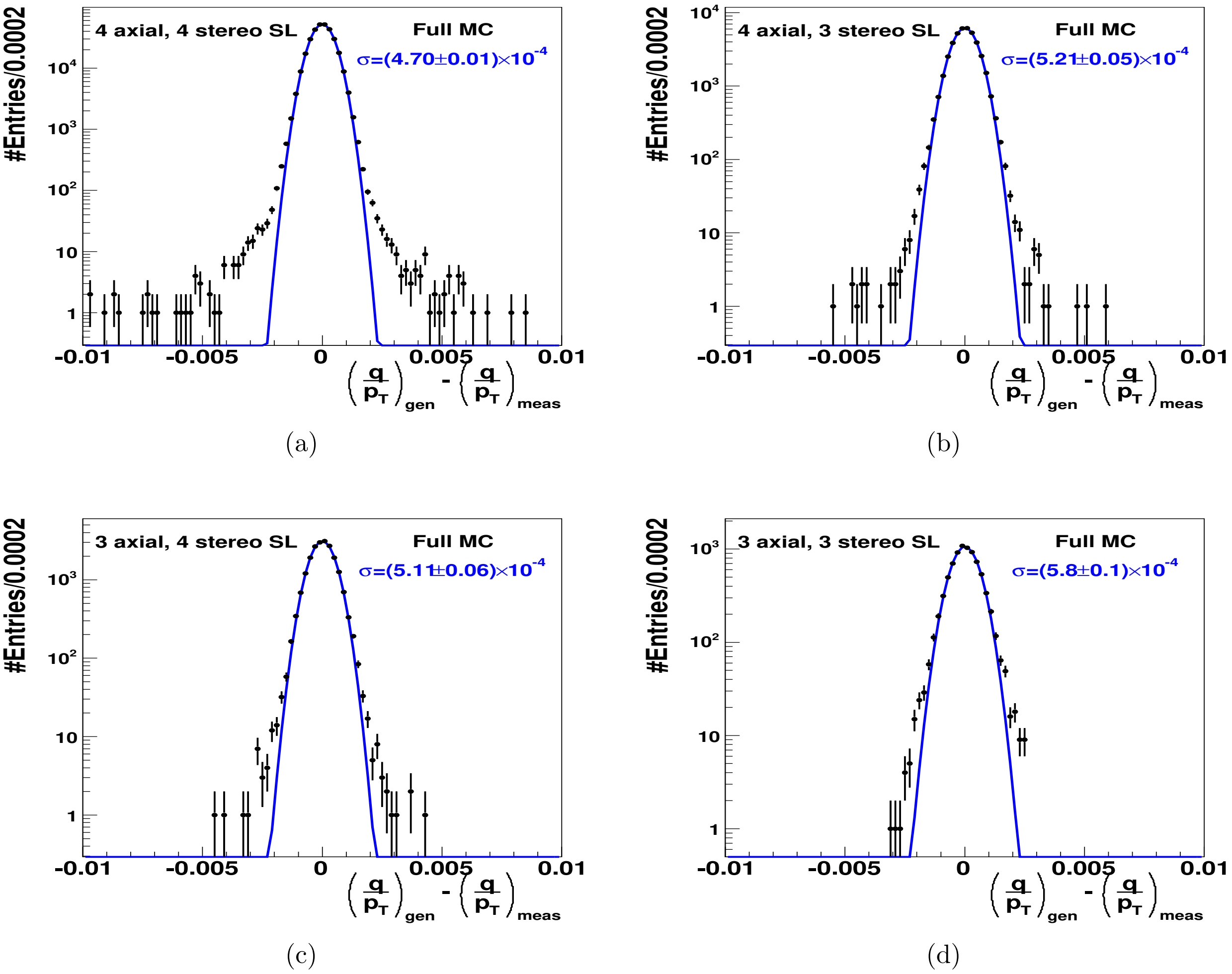

Figure 20: The $\Delta\rho$ distribution taken from $W \rightarrow \mu\nu$ CdfSim events for muon tracks with (a) four N^{axial}_{seg} and four N^{stereo}_{seg}, (b) four N^{axial}_{seg} and three N^{stereo}_{seg}, (c) three N^{axial}_{seg} and four N^{stereo}_{seg}, (d) three N^{axial}_{seg} and three N^{stereo}_{seg}. The distributions are fitted with a Gaussian function, it is clear that the momentum resolution has non-Gaussian components.

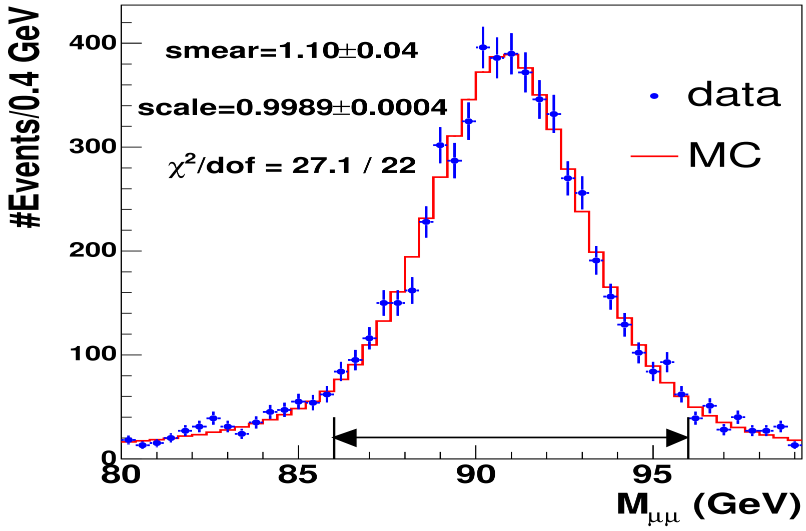

Figure 21: The distribution of $M_{\mu\mu}$ for the data and best fitting Monte Carlo template.

M_T^{cut} [GeV]	$\Delta\Gamma_W[\mathrm{S}^{\mathrm{mom}}]$	$\Delta\Gamma_W[\mathrm{S}^{\mathrm{res}}]$
80	29 MeV	29 MeV
85	27 MeV	27 MeV
90	17 MeV	21 MeV
100	8 MeV	11 MeV
110	5 MeV	5 MeV

Table 27: Systematic uncertainties on Γ_W due to the momentum scale and resolution.

The procedure described above assumes that CdfSim gets the shape of the $\Delta\rho$ distribution correct and only allows for a multiplicative factor to account for differences between CdfSim and the data. In order to account for any possible bias in this assumption the 'non-Gaussian' fraction is verified using the E/p distribution in W $\rightarrow$ eν events. The low and high E/p regions are affected by the 'non-Gaussian' fraction. The low E/p region is also affected by energy leakage into the hadronic calorimeter. Electrons with $E_T > 35$ GeV that pass a tighter $\mathrm{E_{had}/E_{em}}$ cut of 0.04 are used since they are less affected by leakage and more by the p_T resolution. These cuts also ensure a decreased level of multi-jet background. In addition electrons in Tower 8 are excluded from this study since it has been observed that they leak more into the hadronic calorimeter. The histograms shown in Figure 20 are split into two components: a Gaussian component found by fitting the distribution to a Gaussian in the region -0.001–0.001, and a non-Gaussian component which comprises of the 'the rest' of the histogram. For a given track one of these two histograms is sampled at a relative rate proportional to their respective integrals. The non-Gaussian fraction, F^{nGaus}, is a multiplicative factor applied to the rate at which the second histogram is sampled with respect to the Gaussian histogram. F^{nGaus} is varied in the simulation and $\mathrm{S^{res}}$ is re-tuned. The relationship $\mathrm{S^{res}}$= 1.14 - 0.04 $\times$ F^{nGaus} is obtained. In order to de-couple from the calorimeter resolution as much as possible the fit is performed in only five bins. Figure 22 shows the E/p distribution in data and the simulation after tuning for F^{nGaus}. The uncertainty on F^{nGaus} has components from κ (described in Section 9), S^{mat} (described in Section 8) and the multi-jet background (described in Section 12.5). Thus we obtain

$$F^{\mathrm{nGaus}} = 1.03 \pm 0.28_{\mathrm{STAT}} \pm 0.34_{\kappa} \pm 0.01_{S^{\mathrm{mat}}} \pm 0.08_{\mathrm{BCK}}. \tag{17}$$

Table 28 summarises the uncertainties on Γ_W due to F^{nGaus} for different fit regions.

M_T^{cut} [GeV]	$\Delta\Gamma_W[F^{\mathrm{nGaus}}]$
80	17 MeV
85	17 MeV
90	16 MeV
100	13 MeV
110	10 MeV

Table 28: Systematic uncertainties on Γ_W due to F^{nGaus}.

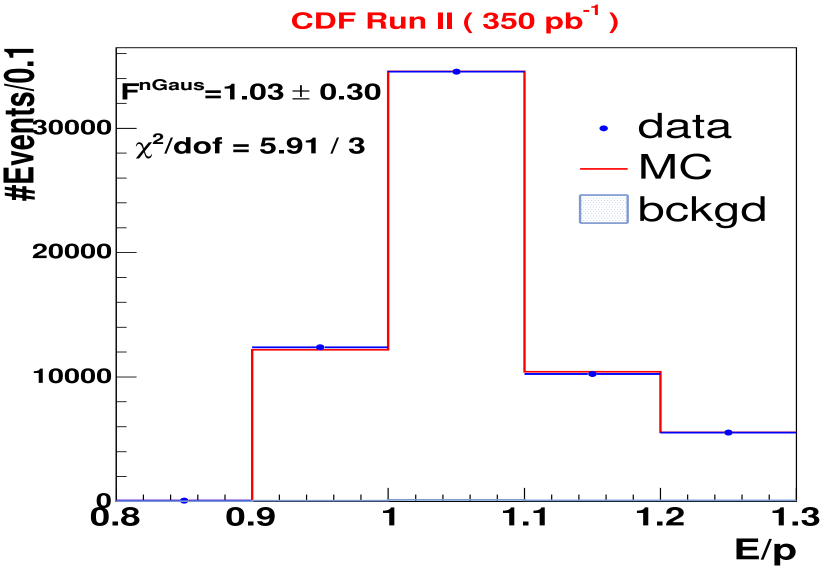

Figure 22: E/p in W $\rightarrow$ eν candidate events against the fast simulation after tuning for F^{nGaus}. It should be noted that the χ^2 of the distribution uses the statistical uncertainties only. If S^{mat} is decreased by 1σ form its best fit value the χ^2 becomes 2.3 for 3 degrees of freedom, suggesting that adding systematic uncertainties from sources such as S^{mat} (and also κ) would improve the χ^2 of the fit.

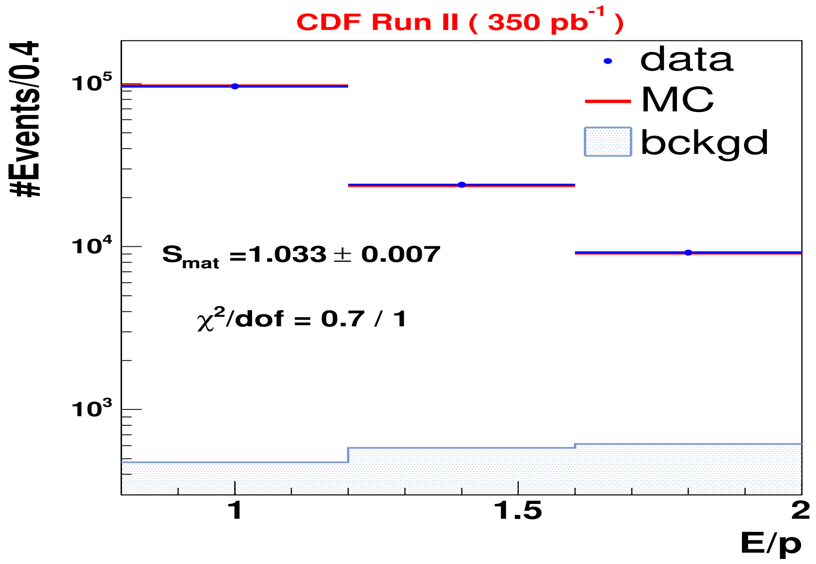

Figure 23: E/p in $W \to e\nu$ candidate events against the fast simulation after tuning for S^{mat}

8 Material Scale Factor

The fractional radiation length traversed by electrons and photons when passing through the inner tracker are provided by `SiliMap`, as described in Section 4. The radiation lengths are scaled by a global factor, S^{mat}, obtained by fitting the simulation to the E/p distribution in $W \to e\nu$ data. The fraction of events in the high E/p tail is sensitive to the amount of Bremsstrahlung in the inner tracker. A fit for S^{mat} to the E/p distribution in the region $0.8 < \mathrm{E/p} < 2.0$ with three bins is performed. Since the E/p cut of $0.8 < \mathrm{E/p} < 1.3$ has been relaxed for this purpose the $\not{E}_T$ cut is increased to 30 GeV in order to reduce the uncertainty due to the amount of multi-jet background. With these modified cuts the multi-jet background is found to be $(1.29 \pm 0.25)\%$. Figure 23 shows the E/p distribution after tuning for S^{mat}, which is found to be:

$$1.033 \pm 0.007_{\mathrm{STAT}} \pm 0.007_{\mathrm{BCK}}, \tag{18}$$

where the background uncertainty is from the multi-jet background only. Table 29 summarises the uncertainties on the width due to S^{mat} for different fit regions.

M_T^{cut} [GeV]	$\Delta\Gamma_W[\ S^{\mathrm{mat}}]$
80	3 MeV
85	3 MeV
90	2 MeV
100	1 MeV
110	0 MeV

Table 29: Systematic uncertainties on Γ_W due to S^{mat}.

9 CEM Response and Resolution

The energy of electrons is measured in the CEM. The fast simulation returns the energy of clustered electrons and photons with a correction due to the energy lost in the ToF and solenoid and leakage into the hadronic calorimeter as described in Section 4. This energy must be smeared and scaled so that it resembles that measured in the data. The CEM scale, S^{CEM}, is a multiplicative factor to the cluster energy, representing the calorimeter response to electrons. The CEM resolution is parameterised as

$$\sigma_E = 13.5\%/\sqrt{E_T} \oplus \kappa \tag{19}$$

where the 13.5% corresponds to the stochastic smearing term obtained from test beam data and κ is the constant term originating from variations in the calorimeter response, which is tuned to the data. Online individual PMT gains and an overall scale factor are applied in reconstructing the CEM energy, which is used at all levels of triggering. The CEM response to particles decreases with time due to the ageing of the scintillators. When needed the online scale is increased to take this variation into account. An offline run dependent correction is then made to the data at the production level to flatten the response as a function of time. This calibration, described in detail in [40], corrects the scale so as to flatten $< E/p >$ as a function of run in an 8 GeV electron trigger sample. The data are also corrected for variations in the CEM response as a function of position within the tower using the functions provided in [41] and [42]. The tower-by-tower corrections described in [42] are not used but are found from the data in this analysis by fitting for S^{CEM} in bins of East-West symmetrized tower number (0–8). κ has contributions from any residual variations in CEM response as a function of tower number, position within the tower and time. Variations as a function of time will provide a contribution to κ that is completely correlated between all electrons in the event and thus must be treated differently within our simulation. Figure 24 shows $\langle E/p \rangle$ of electrons in the $W \rightarrow e\nu$ data sample as a function of time, where a clear residual dependence is seen. The reason for this dependence is described in the following. The underlying event energy added to the two-tower cluster of reconstructed electrons increases with instantaneous luminosity and thus $\langle E/p \rangle$ increases with time. This cancels out a small contribution of the decline in response as a function of time seen in the 8 GeV electron calibration sample. Thus the run dependent offline correction applied at the production level is under-estimated. The electron towers in $W \rightarrow e\nu$ events also have an instantaneous luminosity dependent underlying energy added to them, but since the average E_T in the W sample is 38 GeV and that in the calibration sample is 11 GeV, the fractional contribution from underlying energy is less. The rms of the distribution in Figure 24 is 0.29%, suggesting that there is a correlated contribution to κ, $\kappa^{corr} = 0.29\%$. The remaining uncorrelated contribution to κ, κ^{uncorr}, and S^{CEM} are found independently by:

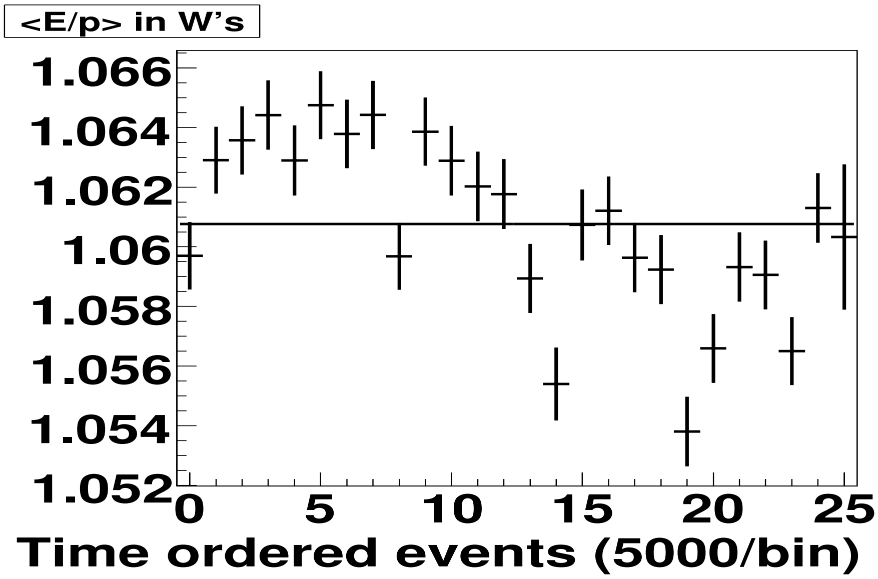

Figure 24: $\langle$E/p$\rangle$ in W $\rightarrow$ eν candidate events; time ordered bins.

1. Fitting templates varying as a function of κ^{uncorr} and S^{CEM} in the simulation to the E/p distribution in W $\rightarrow$ eν data.

2. Fitting templates varying as a function of κ^{uncorr} and S^{CEM} in the simulation to the M_{ee} distribution in Z $\rightarrow e^+e^-$ data.

Figure 25 shows the E/p distribution in data and the simulation after tuning for κ^{uncorr} and S^{CEM}. The uncertainty on both parameters has contributions from the track momentum scale and resolution and the material scale factor. Thus we obtain :

$$\kappa^{\text{uncorr}} = (0.947 \pm 0.049_{\text{STAT}} \pm 0.147_{\text{TRACK}} \pm 0.056_{S^{\text{mat}}})\% \tag{20}$$

and

$$\text{S}^{\text{CEM}} = 1.02356 \pm 0.00021_{\text{STAT}} \pm 0.00044_{\text{TRACK}} \pm 0.00017_{S^{\text{mat}}} \tag{21}$$

The value of κ^{uncorr} obtained from the E/p fit is dependent on the fit range. If a fit range of 0.96–1.1 is used instead of 0.9–1.1, we obtain $\kappa^{\text{uncorr}} = (0.64 \pm 0.11_{\text{STAT}})\%$.

Figure 26 shows the M_{ee} distribution in data and the simulation after tuning for κ^{uncorr} and S^{CEM}. We obtain :

$$\kappa^{\text{uncorr}} = (1.49 \pm 0.29)\% \tag{22}$$

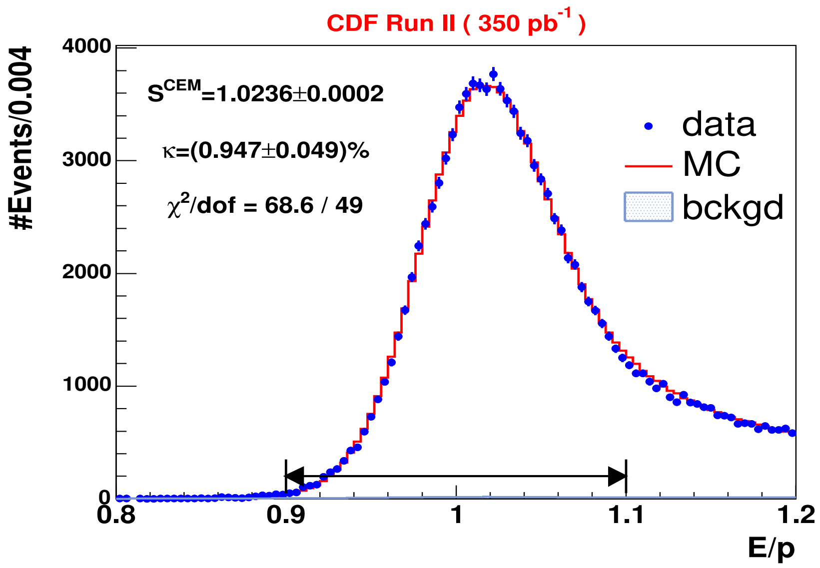

Figure 25: E/p in W $\rightarrow$ eν candidate events against the fast simulation after tuning for κ^{uncorr} and S^{CEM}.

and

$$\mathrm{S}^{\text{CEM}} = 1.02439 \pm 0.00078 \tag{23}$$

The values obtained for S^{CEM} are consistent with each other and are combined in a weighted average to give :

$$\mathrm{S}^{\text{CEM}} = 1.02382 \pm 0.00043 \tag{24}$$

The values for κ^{uncorr} are combined with a weighted average. The uncertainty on κ^{uncorr} is conservatively chosen to cover the values obtained from the M_{ee} fit and the E/p fit with both fit ranges, giving :

$$\kappa^{\text{uncorr}} = (1.08^{+0.41}_{-0.44})\% \tag{25}$$

The uncertainty on Γ_W due to the uncertainty on the calorimeter scale and resolution is found by generating a Monte Carlo M_T distribution using the best fit parameters and M_T templates with the parameters varying individually by -4σ,-2σ, 2σ and 4σ from their best fit values. The 1σ uncertainty in interpolated from this distribution. Table 30 summarises the obtained uncertainties for different fit regions.

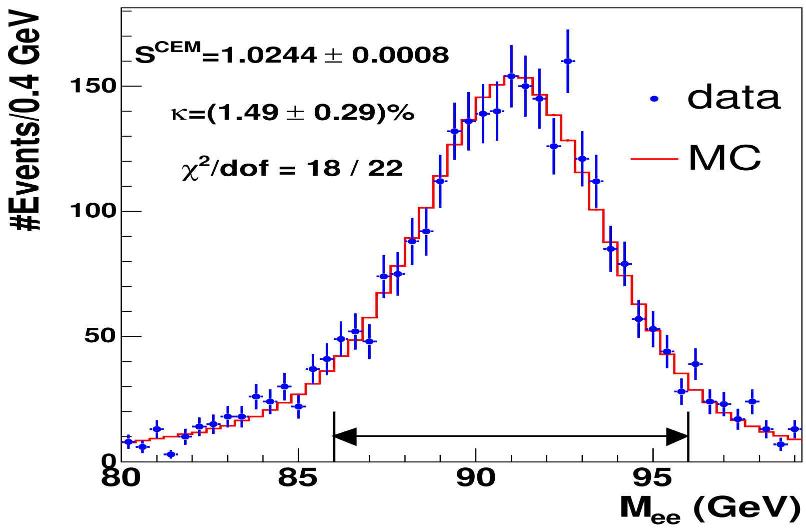

Figure 26: M_{ee} in Z $\rightarrow e^+e^-$ candidate events against the fast simulation after tuning for κ^{uncorr} and S^{CEM}.

M_T^{cut} [GeV]	$\Delta\Gamma_W[\text{S}^{\text{CEM}}]$	$\Delta\Gamma_W[\kappa]$
80	29 MeV	$-45, +46$ MeV
85	27 MeV	$-42, +43$ MeV
90	17 MeV	$+30, +31$ MeV
100	7 MeV	$-10, +11$ MeV
110	4 MeV	$+3, \ -4$ MeV

Table 30: Systematic uncertainties on Γ_W due to the calorimeter scale and resolution.

10 Calorimeter Non-linearity

The CEM may have a different effective energy scale for high- and low-energy electromagnetic energy deposits; we refer to this as the calorimeter non-linearity. Note that we simulate the important sources of an *effective* energy scale non-linearity: namely, the absorption of an incident electron's energy in the ToF and solenoid coil, and the longitudinal leakage of shower energy into the hadronic compartment. What we aim to parameterise here is the residual *intrinsic* non-linearity for energy deposits in the active volume of the CEM. There could be several physical sources for such a non-linearity; the most plausible is that light from higher energy showers, originating on average deeper in the calorimeter than light from lower energy showers, suffers less absorption in the ageing wavelength shifting fibres transporting the light to the PMT's. This would result in a higher energy scale for high-energy showers and indeed this is what we observe. Importantly, this source of non-linearity would affect each incident particle separately, and therefore ought to be applied in the simulation at the particle level rather than the reconstructed energy level.

10.1 The Non-linearity Fitting Procedure

We fit the distribution of E/p in bins of electron-E_T. Since the momentum scale is linear, the variation in E/p as a function of electron-E_T is sensitive to the calorimeter energy scale non-linearity. We construct the fitting procedure to explicitly obtain the per-particle non-linearity.

A reconstructed electron is comprised of several individual electrons and photons entering the calorimeter towers that make up the electron cluster. Allowing a first-order non-linearity, the observed transverse energy, E_T, is therefore given by :

$$E_T = \sum_i (a + b \times E_T^{e,\gamma}) E_T^{e,\gamma} \ ,$$

which can be written as :

$$E_T = a \sum_i E_T^{e,\gamma} + b \sum_i (E_T^{e,\gamma})^2 \ .$$

We perform large fast simulation runs where, for each simulated electron, we record the particle sums appearing in the above expression, as well as the reconstructed track-p_T. We are then able to explicitly re-compute in a fitting program the observed electron-E_T and (E/p) values as a function of scale and slope parameters.

10.2 Results of the Non-linearity Fit

The W data are fitted in the range $25 < E_T < 50$ GeV and the Z data in the range $30 < E_T < 55$ GeV. In order to decouple the non-linearity fit from material scale and resolution issues, the fit is performed in the reasonably tight range $0.9 < \mathrm{E/p} < 1.1$. To reduce backgrounds in the W sample to a negligible level, tight cuts $\not\!\!E_T > 30$ GeV and $U < 10$ GeV are applied; all other cuts are standard.

The E/p distributions in slices of electron-E_T are shown for the W data in Figure 27, along with the best fit simulation distributions. Along with the corresponding Z distributions, an aggregate χ^2 is defined combining all the slices. The fitter converges on the following best-fit non-linearity parameter values, corresponding to a $\chi^2/\mathrm{dof} = 180/193$:

$$a\,(\mathrm{SCALE}) = 0.9992 \pm 0.0002$$

$$b\,(\mathrm{SLOPE}) = 267 \pm 50 \times 10^{-6}\ \ \mathrm{GeV}^{-1}$$

where these 1-dimensional errors correspond to a $\Delta\chi^2 = 1$. The pivot point, chosen to be the mean electron-E_T in the combined W and Z sample of 36.9 GeV, largely decorrelates the scale and slope parameters, as can be seen in Figure 28. It can also be seen that the quoted uncertainties do indeed correspond to the expected χ^2 intervals in 1- and 2-dimensions. Another way of representing the fit result is to plot the ratio of mean E/p values between data and simulation, shown in Figure 29 for W and Z data. It can be clearly seen that the best fit non-linearity parameters flatten out this ratio across the entire range of electron-E_T.

10.3 Non-linearity Systematic Uncertainty

The systematic uncertainty on the scale is evaluated in Section 9. The non-linearity systematic is that due to the uncertainty on the fitted slope alone; therefore we propagate the 1-dimensional errors quoted above. By fitting large statistics Monte Carlo samples against one another, the derivatives and the corresponding shift in Γ_W shown in Table 31 are obtained for the different fit ranges.

M_T^{cut} [GeV]	$\mathrm{d}\Gamma_W/\mathrm{d}b$ [GeV^2]	$\Delta\Gamma_W$[non-lin]
80	230	12 MeV
85	250	13 MeV
90	230	12 MeV
100	190	10 MeV
110	120	6 MeV

Table 31: Variation of the fitted width with non-linearity slope, for different fit ranges.

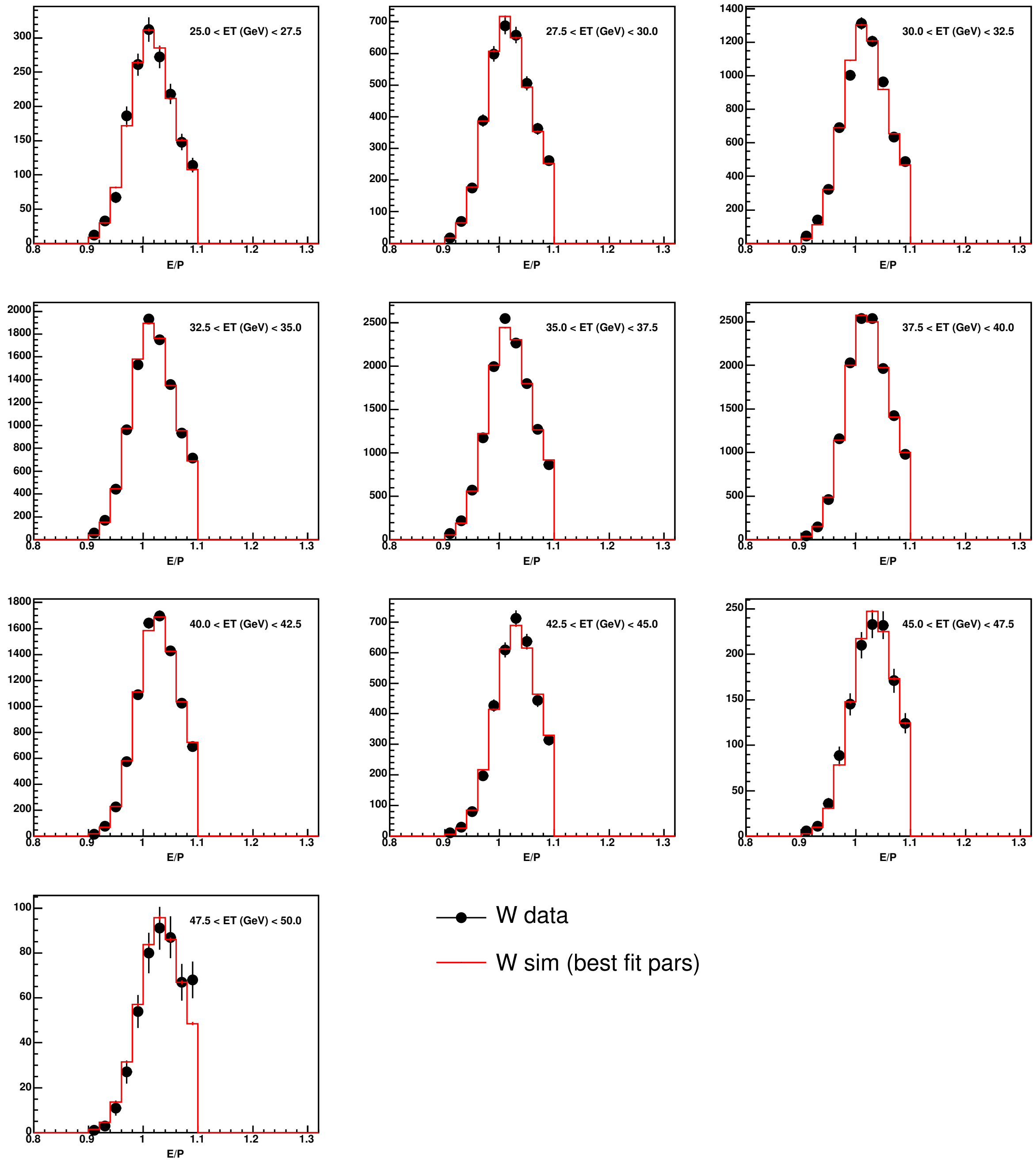

Figure 27: E/p distributions in slices of electron-E_T for W data with cuts described in the text. Good agreement with simulation is observed over a wide range of E_T for the best-fit non-linearity parameters.

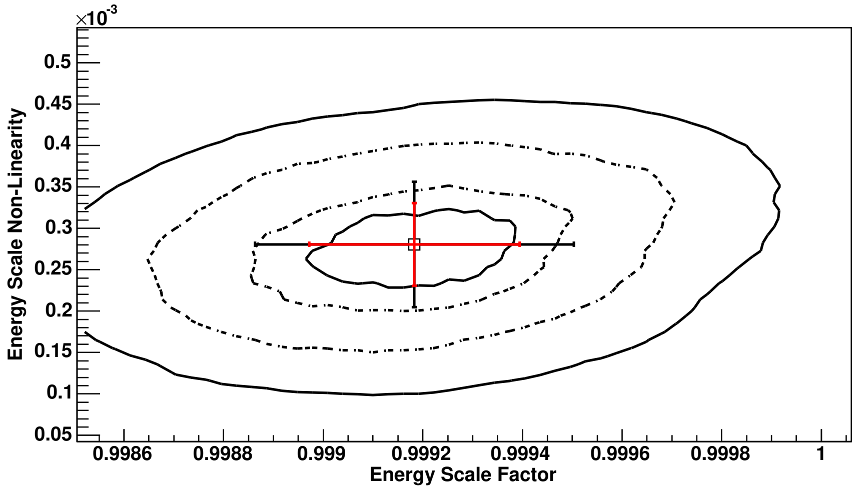

Figure 28: The results of the 2-dimensional fit for the CEM energy scale (horizontal axis) and non-linearity (vertical axis). The inner (outer) error bars denote the 1(2)-dimensional uncertainties on the fitted parameters. The ellipses indicate, from the centre outwards, contours of $\Delta\chi^2 = 1$, 2.30, 5.99 and 11.83.

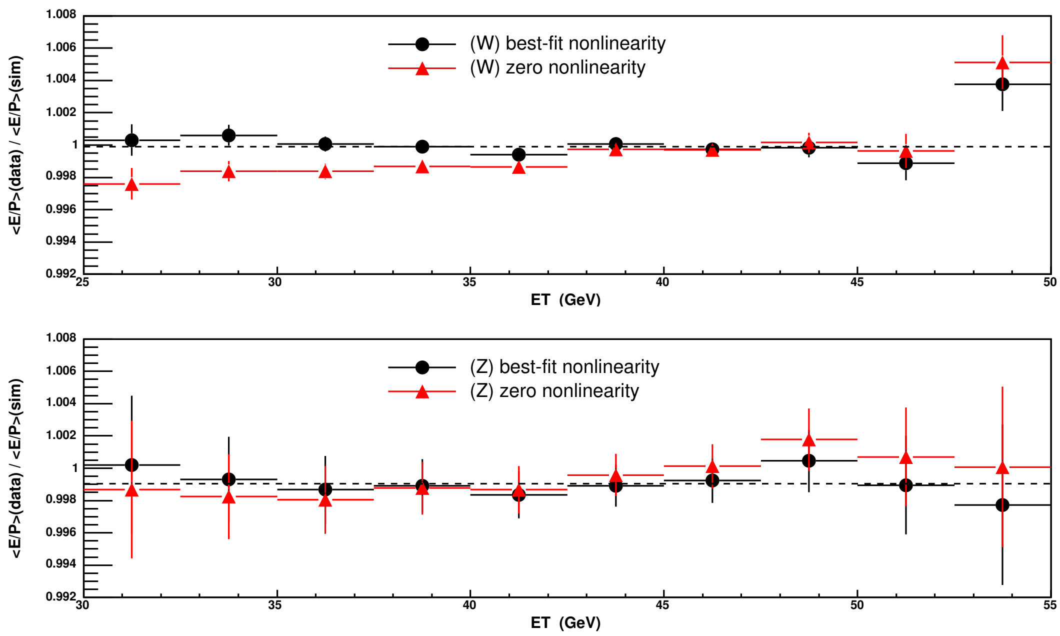

Figure 29: The ratio of mean E/p between data and simulation for W electrons (top) and Z electrons (bottom). The ratio obtained with the best-fit simulation non-linearity parameters is shown by the black points, and the ratio obtained with zero simulated non-linearity is shown by the red points. See text for further details.

11 Recoil Model

11.1 Introduction

The recoil refers to all calorimeter energy in the event not associated with the lepton. It receives contributions from initial state QCD radiation, final state QED radiation (and consequent conversions) from the charged lepton, conversions from the co-linear bremsstrahlung photons from interactions with the material, from (anti)-proton remnants and from concurrent minimum bias interactions. As such the recoil has a dependence on the boson p_T, the instantaneous luminosity, the detector material distribution and the treatment of QED photons and is a multi-faceted problem. Particle-level Monte Carlos such as PYTHIA and HERWIG are not accurate enough to model all these effects at the accuracy required for the width measurement and instead an aggregated model is tuned to the data. The model incorporates dependencies on luminosity and boson p_T and simulates all effects associated with QED photons (and conversions), the knockout region and any biases associated with the event selection cuts. In general the recoil is poorly measured; on average only 70% of the QCD radiation contribution is measured due to the effects of incomplete calorimeter coverage, tower thresholds and the magnetic field sweeping particles out of the active detector volume.

The underlying ethos of the recoil model is that broadly speaking we can consider the non-leptonic energy as being composed of two contributions. A 'hard' component from the initial state QCD radiation which has a strong dependence on the boson p_T and which we expect to be predominantly in the direction opposite to the total lepton p_T and a 'soft' component from the minimum bias events which has a strong dependence on luminosity and which we expect to be uniformly distributed in the azimuthal angle or with respect to the boson p_T. The recoil model is thus parameterised by considering projections of the recoil energy in directions which are predominantly sensitive to either the hard or soft component. We expect the resolutions of the two components to be somewhat different - the hard component will be more jet-like and have a stronger dependence on p_T compared to the soft minimum bias component. We use minimum bias and Z data to tune the recoil model parameters since we expect the recoil component in W events to be very similar to Z events.

11.1.1 Recoil Components

In the Z events we define two recoil components : U_1 which is the projection of the recoil along the p_T^Z direction (as reconstructed from the leptons) and is largely sensitive to the 'hard' component and U_2 which is the projection orthogonal to the p_T^Z direction which is largely sensitive to the 'soft' component. This is illustrated in Figure 30.

In the W events, where p_T^W cannot be reconstructed due to the missing neutrino, the recoil components are projected with respect to the reconstructed charged lepton direction: $U_{||}$ is the parallel and $U_{\perp}$ the perpendicular component to the direction of the lepton.

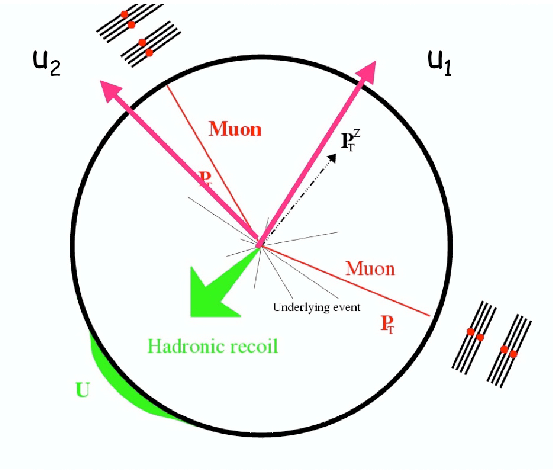

Figure 30: Definition of the two recoil components U_1, U_2 in the $Z \to \ell\ell$ decays used to tune the recoil parameters.

11.2 Knockout Region / Underlying Event Corrections

The energy deposited by the charged lepton is generally not confined to a single tower and there is significant leakage to neighbouring towers which is exacerbated by contributions from QED radiation. In defining the recoil energy care must be taken not to include any contributions from the charged lepton. This is achieved by defining a 'knockout region'. Towers that contain any significant lepton energy are removed from the recoil sum. The energy in these towers is replaced with an underlying event (UE) energy sampled from data distributions, taking into account any kinematic biases. The average energy in the towers immediately surrounding the charged lepton is shown in Figure 31. There is significant energy from the lepton (and QED photons) in 7(3) towers for electrons(muons). It is these towers (denoted by the thick lined boundary in the figure) that are removed from the recoil sum. Since the removal of these towers also removes the UE energy, this must be added back to the recoil sum. The UE energy is estimated for both the electromagnetic and hadronic calorimeters by sampling the energy of a 7-tower cluster in the region $\Delta\phi = 90^0$ from the lepton. Scale factors are then applied to the obtained energy to account for the dependence of UE on instantaneous luminosity, $U_{||}$ and η of the lepton seed tower.

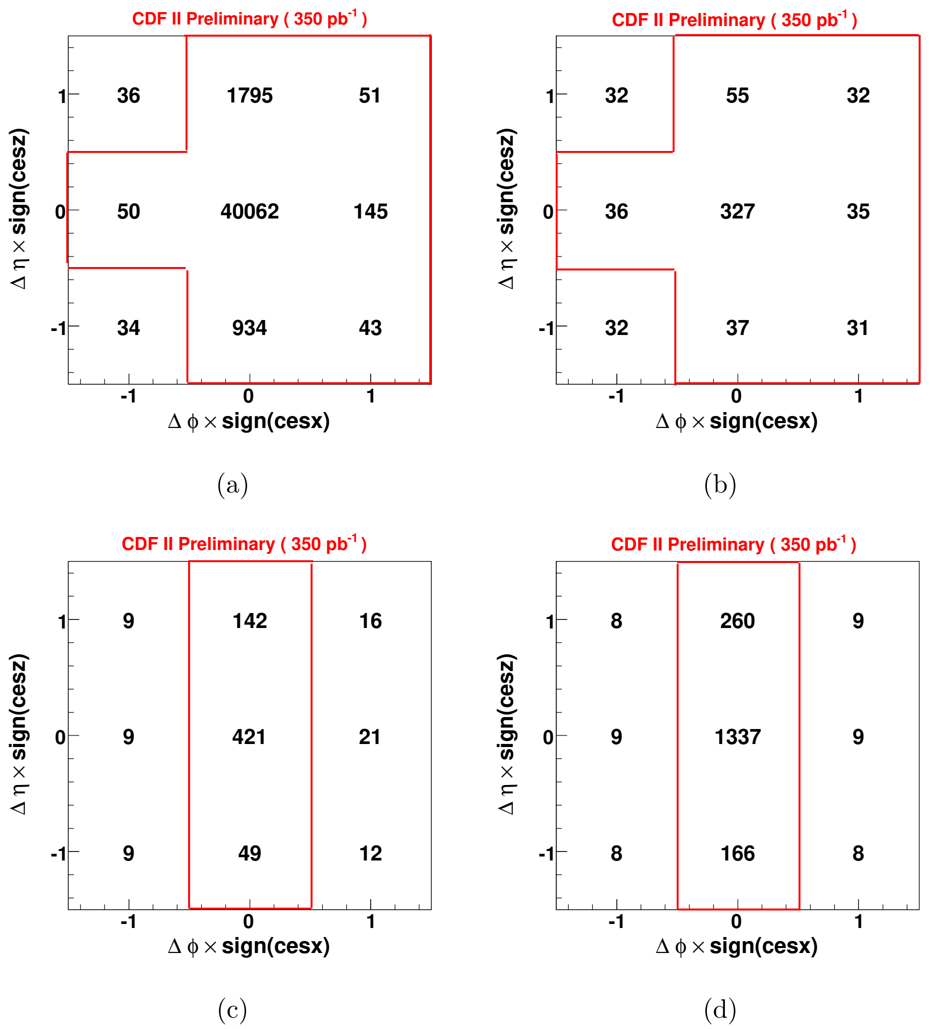

Figure 31: The energy in the towers immediately surrounding the charged lepton in the (a) electromagnetic and (b) hadronic calorimeters in $W \rightarrow e\nu$ events and the (c) electromagnetic and (d) hadronic calorimeters in $W \rightarrow \mu\nu$ events. The central tower is defined by the maximal energy deposition of the charged lepton, and the $+1$ $\Delta\eta$ tower is the tower closest in z to the lepton. $\Delta\phi$ is signed by the charge of the lepton. The knockout region, 7 towers for electrons and 3 towers for muons, is denoted by the thick red border line.

The UE dependence on luminosity, $U_{||}$ and η is obtained by considering a single 7-tower cluster with the central tower at the same η as the seed lepton tower but separated by 90^0 in ϕ. The dependence of the UE energy in this cluster on luminosity is shown in Figure 32.

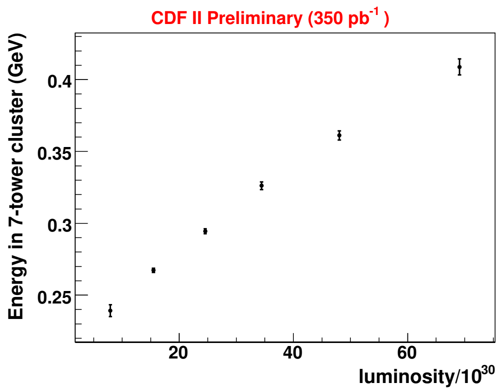

Figure 32: Underlying energy in a 7-tower cluster in a region orthogonal in ϕ but at the same η as the charged lepton as a function of instantaneous luminosity.

The UE energy as a function of $U_{||}$ is shown in Figure 33; we expect a larger UE energy in the lepton knockout region when the recoil is in the same direction as the charged lepton i.e. when $U_{||}$ is large and positive. The UE energy is reduced in towers 0, 7 and 8 and there is a weak dependence on rapidity for towers 1−6. The UE energy is thus added as a function of the ieta of the tower in accordance with Figure 34, where an ieta of 26 to 34 and 25 down to 17 correspond to tower numbers 0 to 8.

In the 7-tower electron knockout region the average UE added back is 233 MeV in the EM and 62 MeV in the HAD, the average 3 tower sums for the muon are 100 MeV (EM) and 27 MeV (HAD). The UE distributions are assumed to be the same in W $\rightarrow e\nu$ and W $\rightarrow \mu\nu$ events, hence those obtained from W$\rightarrow e\nu$ events are used for both samples.

The UE energy distributions are also used in the simulation. The deposited energy in the data has a contribution from the UE which increases with luminosity. Similarly the energy in the muon tower receives a luminosity dependent UE contribution such that on average the E_{em} cut is more likely to fail at high luminosity, particularly in events with a large QED contribution. Also the electron energy has a contribution from UE that is luminosity dependent. In order to capture the correlations with the recoil we add UE energy to the lepton towers in the simulation as a function of the ΣE_T of the recoil. ΣE_T increases with instantaneous luminosity and at high ΣE_T we expect the resolution on the recoil to be larger and at high luminosity we expect the UE contribution to the lepton cluster to increase. By adding UE as a function of ΣE_T we capture the correlation between

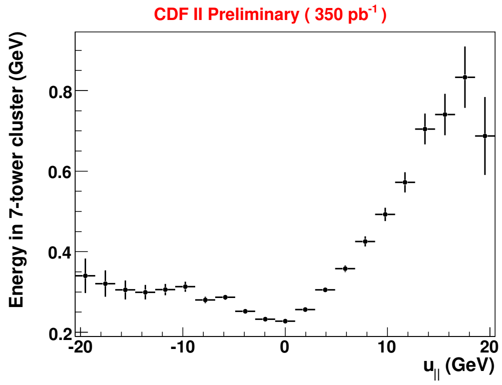

Figure 33: UE energy in 7-tower cluster as a function of $U_{||}$ where $U_{||}$ is defined with respect to this cluster.

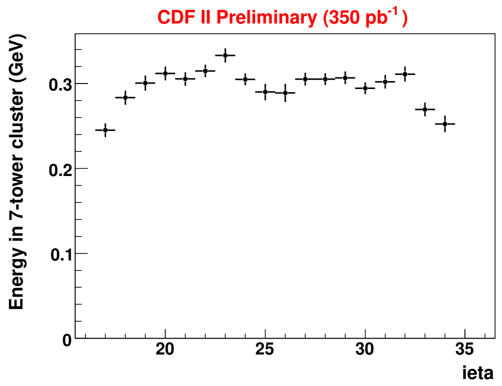

Figure 34: UE energy in 7-tower cluster as a function of the ieta of the seed tower of the charged lepton

increased recoil resolution and the dependence on luminosity of the UE contribution to the lepton energy.

In the fast simulation, care is taken to emulate the knockout region. All QED photons (and conversions) are propagated and removed from the recoil sum if they fall in the knockout region.

In the data, the recoil is obtained by summing over all the towers in the calorimeter with energy above 100 MeV, excluding those in the miniplug calorimeter. A relative scaling factor is applied to all towers to account for the difference in response in the central and plug calorimeters. Energies in the central towers are scaled by 1.05 and plug tower energies by 0.93 [43].

11.3 The Recoil Parameterisation

The parameterisation of the recoil is based on the assumptions that the mean of U_2 should be zero while that of U_1 should increase with the boson p_T, and the direction of the recoil is opposite the boson p_T but with a large spread as $p_T \to 0$. The soft component of the recoil resolution can be obtained from minimum bias events and we expect the resolution of U_2 to be largely described by this contribution, while allowing for an explicit boson p_T dependence. The precise functional form of the parameterisation is ad-hoc, where the 7 parameters give sufficient flexibility so that the reliance on the forms chosen is not significant. The recoil luminosity dependence is captured by parameterising the recoil resolution as a function of ΣE_T, which in turn is fitted to the Z data with the same luminosity profile as the W data. Since true boson p_T is the only boson p_T which is unambiguously defined in the simulation for both W and Z events, the functional forms have an explicit recoil dependence on the true boson p_T. However the recoil parameters must be determined from fits to data as a function of the measured boson p_T, where the simulation accounts for the detector effects.

The 'soft' component of the resolution, σ_{MB}, is determined from a 2-parameter (R_1, R_2) fit to minimum bias events, where:

$$\sigma_{MB} = R_1 \times (\Sigma E_T)^{R_2} \quad . \tag{26}$$

The ΣE_T distribution is determined from a 4-parameter fit to Z data. The form has an implicit luminosity dependence, while the dependence on (true) boson p_T is added explicitly:

$$\Sigma E_T = (Q_1 + Q_2 \times p_T) \times \Gamma(Q_3 + Q_4 \times p_T + 1) \quad . \tag{27}$$

We do not estimate the uncertainty of the parameters $R_{1,2}$ and $Q_{1,4}$ separately: they are the starting point of the resolution function which is ultimately constrained from U_1

and U_2 fits to the Z data, where the errors of the 7 recoil parameters from the Z fits account also for the uncertainty in $R_{1,2}$ and $Q_{1,4}$.

The recoil resolution is defined by 4 parameters, $P_4 - P_7$:

$$\sigma(U_1) = \sigma_{MB}(P_4 + P_5 \times p_T) \quad , \tag{28}$$

$$\sigma(U_2) = \sigma_{MB}(P_6 + P_7 \times p_T) \quad . \tag{29}$$

The recoil response, defined in terms of the mean U_1 value $\langle U_1 \rangle$, is defined by 3 parameters, $P_1 - P_3$:

$$\langle U_1 \rangle = (P_1 + P_2 \times p_T) \times \left(1 - e^{\,(-P_3 \times p_T)}\right) \quad . \tag{30}$$

The recoil components are thus generated as normally distributed quantities with p_T dependent mean and σ and an implicit dependence on luminosity through the ΣE_T parameterisation of σ_{MB} :

$$\begin{aligned} U_1 &= G(\langle U_1 \rangle(p_T) \quad , \sigma(U_1)(p_T, \Sigma E_T)) \quad , \\ U_2 &= G(\quad 0 \quad\quad , \sigma(U_2)(p_T, \Sigma E_T)) \quad . \end{aligned}$$

11.4 Recoil Fit Results

11.4.1 Minimum Bias Fits

Minimum bias data (with 100 MeV tower thresholds) is used to determine σ_{MB}. The fit yielding the parameters, R_1 and R_2, is shown in Figure 35. The fit parameters obtained are $R_1 = 0.3384$ and $R_2 = 0.5589$.

11.4.2 $\mathbf{\Sigma E_T}$ Fit

The ΣE_T distribution is parameterised in terms of the true boson p_T. The Z events are split into 10 equal event samples by p_T^Z. A total χ^2 from these 10 ΣE_T distributions and the overall ΣE_T distribution is minimised to determine Q_{1-4}. The Z $\rightarrow e^+e^-$ and Z $\rightarrow \mu^+\mu^-$ events are fitted separately since the electron and muon datasets have a different luminosity distribution. The Z $\rightarrow e^+e^-$ and Z $\rightarrow \mu^+\mu^-$ ΣE_T distributions and the simulation (using the best fit parameters) are shown in Figure 36. Throughout this chapter, the blue histogram represents the simulation and the data is represented by red points. The best fit parameters obtained are summarised in Table 32.

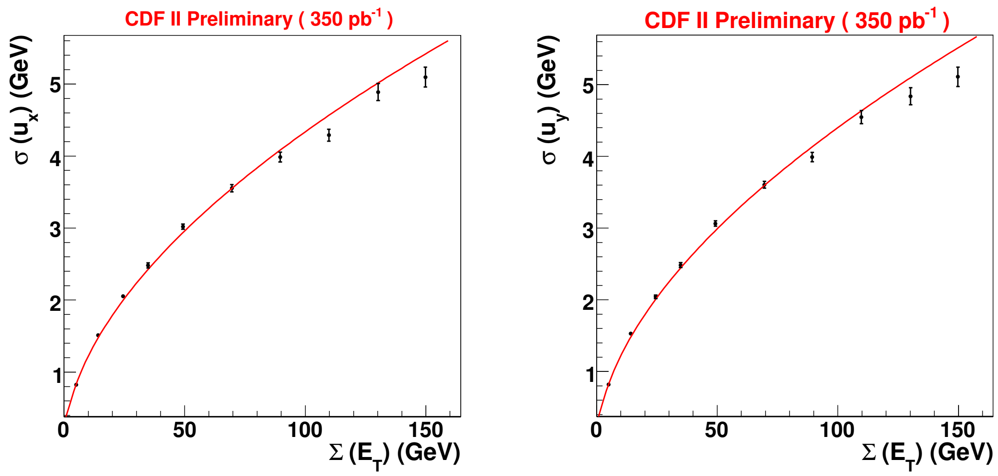

(a) (b)

Figure 35: The fit to the (a) $\sigma(U_x)$ and (b) $\sigma(U_y)$ distributions in minimum bias data.

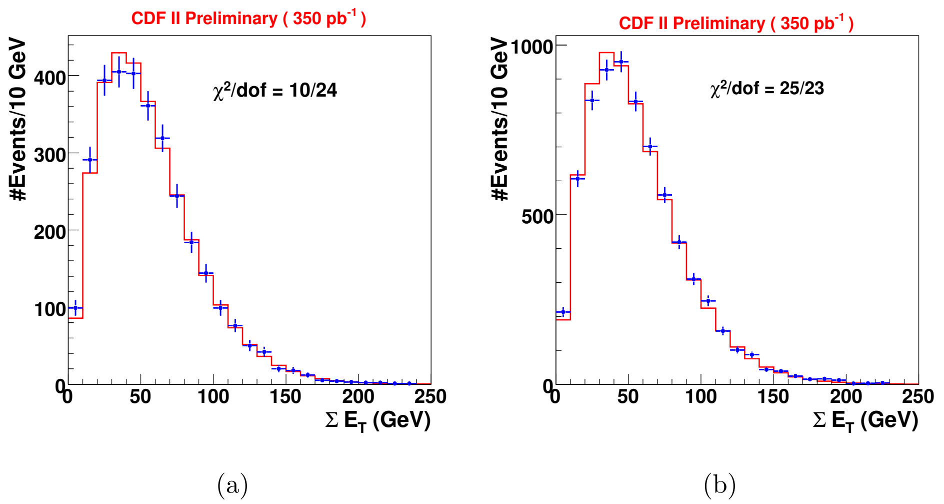

Figure 36: ΣE_T distributions for (a) Z $\rightarrow e^+e^-$ and (b) Z $\rightarrow \mu^+\mu^-$ compared to the simulation using the best fit parameters.

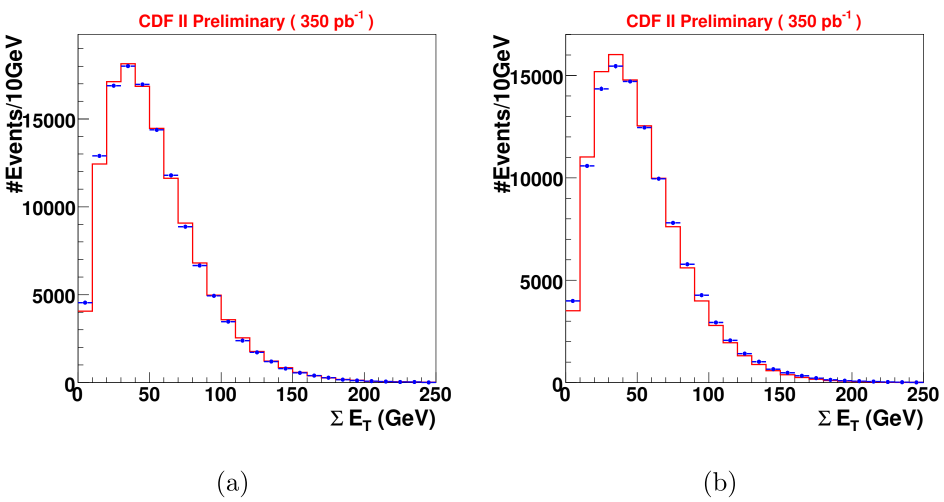

Figure 37: ΣE_T distributions for (a) W $\rightarrow$ eν and (b) W $\rightarrow \mu\nu$ compared to the simulation using the best fit parameters.

The ΣE_T of the W data compared to the simulation (based on the Z fits) is shown in Figure 37. Figure 38 shows the mean ΣE_T of Z events as a function of p_T^Z for the data and the simulation.

	$Z \to e^+e^-$	$Z \to \mu^+\mu^-$
Q_1	20.700	19.351
Q_2	-0.154	-0.141
Q_3	1.055	1.051
Q_4	0.085	0.100

Table 32: The ΣE_T parameters obtained by fitting $Z \to e^+e^-$ and $Z \to \mu^+\mu^-$ events.

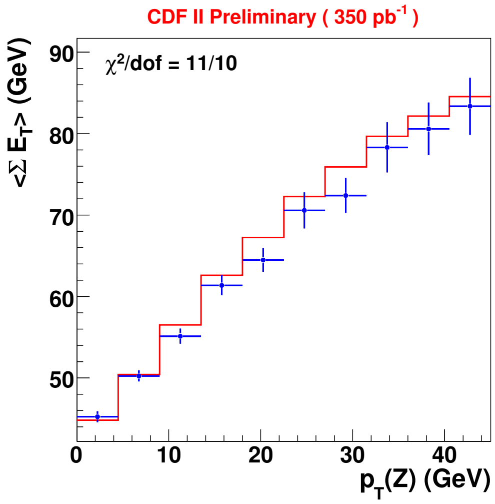

Figure 38: $\langle \Sigma E_T \rangle$ of the $Z \to \mu^+\mu^-$ data as a function of p_T^Z compared to the simulation.

11.4.3 Z Data Fits for the Response and Resolution Parameters

The recoil parameters are obtained by fitting Z data with high statistics binary files produced from the fast simulation that contain the true and measured boson p_T, where our fit procedure accounts for the effects of smearing and selection cuts. For a given P_{1-7} parameter choice $U_{1,2}$ values are produced as a function of the true boson p_T and rotated to form $U_{x,y}$. The total χ^2 from three Z distributions is minimised to determine $P_{1,7}$:

1. $\langle U_1 \rangle$ vs p_T^Z predominantly constrains the response parameters P_{1-3},

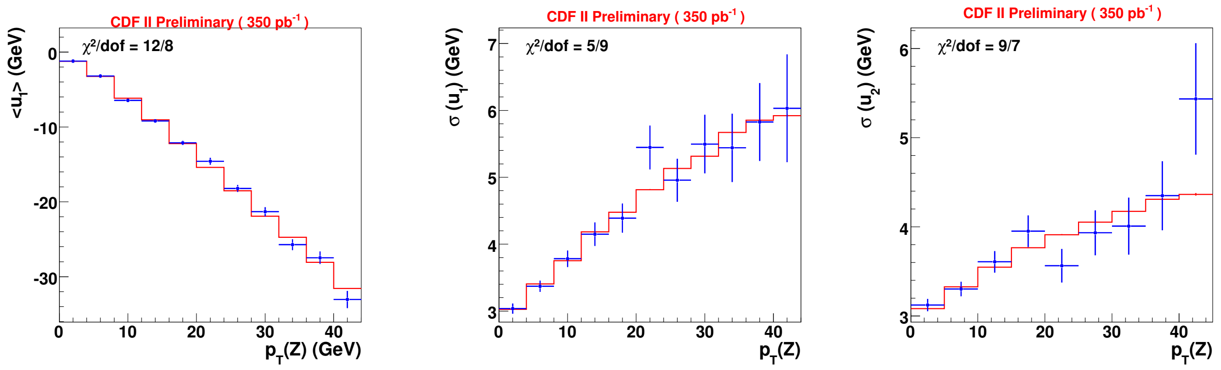

(a) (b) (c)

Figure 39: (a) $\langle U_1 \rangle$ vs p_T^Z, (b) $\sigma(U_1)$ vs p_T^Z and (c) $\sigma(U_2)$ vs p_T^Z for the $\mathrm{Z} \to e^+e^-$ data compared to the best fit simulation.

2. $\sigma(U_1)$ vs p_T^Z constrains the resolution parameters $P_{4,5}$ and

3. $\sigma(U_2)$ constrains the resolution parameters $P_{5,6}$.

The three fitted distributions are shown in Figure 39 for $\mathrm{Z} \to e^+e^-$ and Figure 40 for $\mathrm{Z} \to \mu^+\mu^-$. The total χ^2 for these distributions is 26/24 ($\mathrm{Z} \to e^+e^-$) and 29/24 ($\mathrm{Z} \to \mu^+\mu^-$). The number of degrees of freedom quoted is equal to the number of data points minus the number of fitted parameters. Figure 41 shows the variation in χ^2 of these distributions around the parameter minima.

The U, U_1, U_2 and $\Delta\phi(U, p_T^Z)$ (the angle between the recoil and p_T^Z) data distributions are compared to the simulation in Figure 43 for $\mathrm{Z} \to e^+e^-$ and Figure 44 for $\mathrm{Z} \to \mu^+\mu^-$. These distributions are not fitted to but are shown for validation only.

The obtained parameters with their uncertainties taken from the diagonal elements of the 7×7 covariance matrix are summarised in Table 33. The largest correlation is between the individual response and resolution parameters, while there is essentially no correlation between the U_1 parameters ($P_{1,5}$) and the U_2 parameters ($P_{6,7}$). Shown in Figure 42 is the example of the two U_2 resolution parameters P_6 and P_7, which are strongly anti-correlated. The statistical uncertainty of the fit propagated to Γ_W is determined taking into account the 7×7 covariance matrix of the parameters.

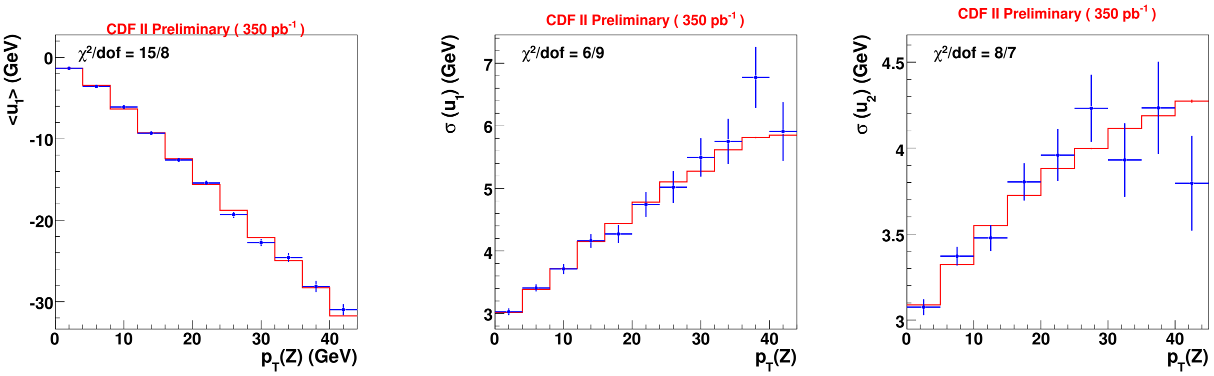

(a) (b) (c)

Figure 40: (a) $\langle U_1 \rangle$ vs p_T^Z, (b) $\sigma(U_1)$ vs p_T^Z and (c) $\sigma(U_2)$ vs p_T^Z for the $Z \to \mu^+\mu^-$ data compared to the best fit simulation.

	electrons			muons		
P1	-12.7	±	1.1	-13.1	±	1.5
P2	-0.589	±	0.02	-0.586	±	0.02
P3	0.043	±	0.003	0.042	±	0.004
P4	0.93	±	0.03	0.97	±	0.02
P5	0.019	±	0.003	0.016	±	0.002
P6	1.025	±	0.03	1.064	±	0.02
P7	0.0002	±	0.002	-0.002	±	0.001

Table 33: The recoil parameters and their statistical uncertainties obtained from the fits to the Z data.

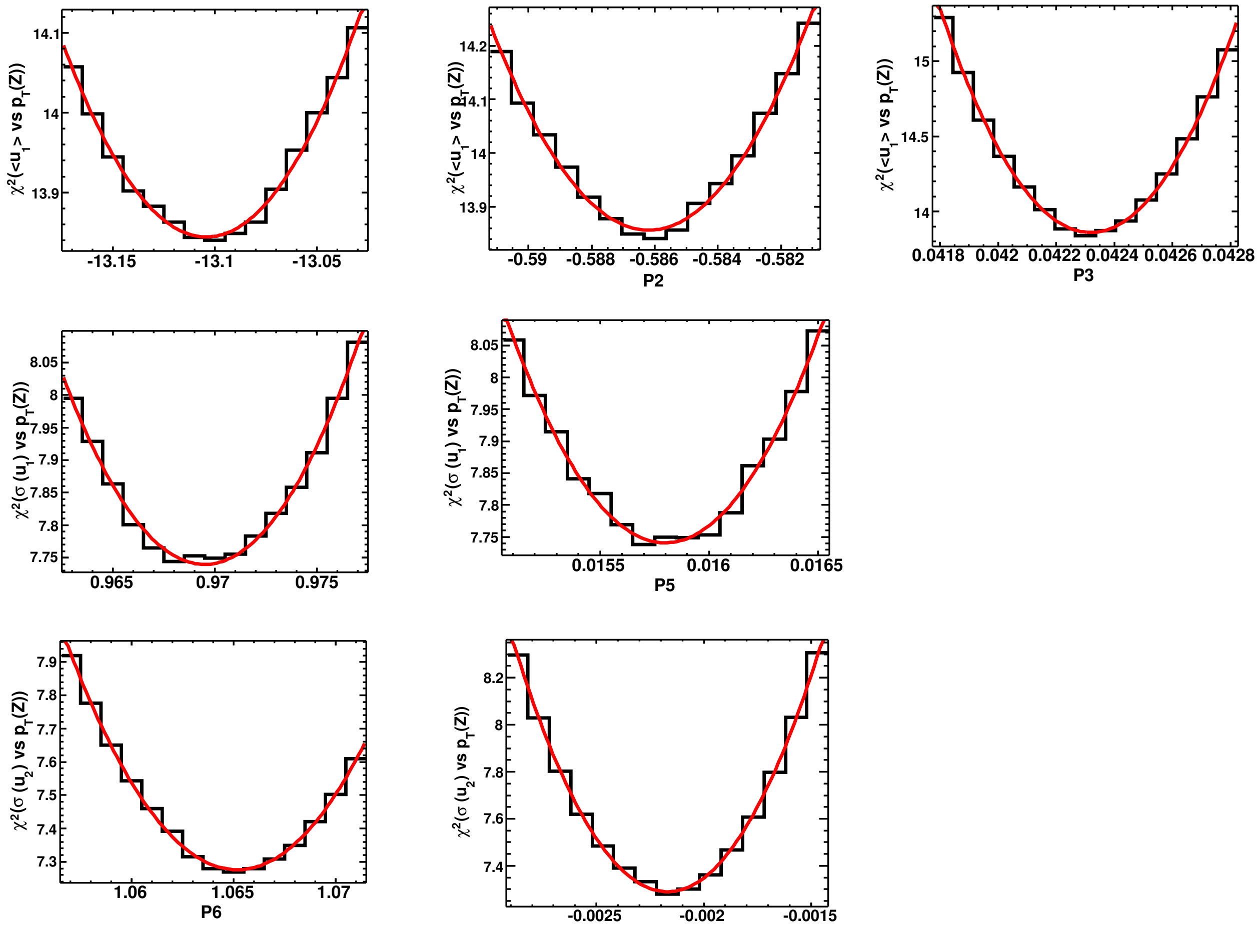

Figure 41: Variation of χ^2 of $\langle U_1 \rangle$ vs p_T^Z with P_1, P_2, P_3 (top), $\sigma(U_1)$ vs p_T^Z with P_4, P_5 (middle) and $\sigma(U_2)$ vs p_T^Z with P_6, P_7(bottom).

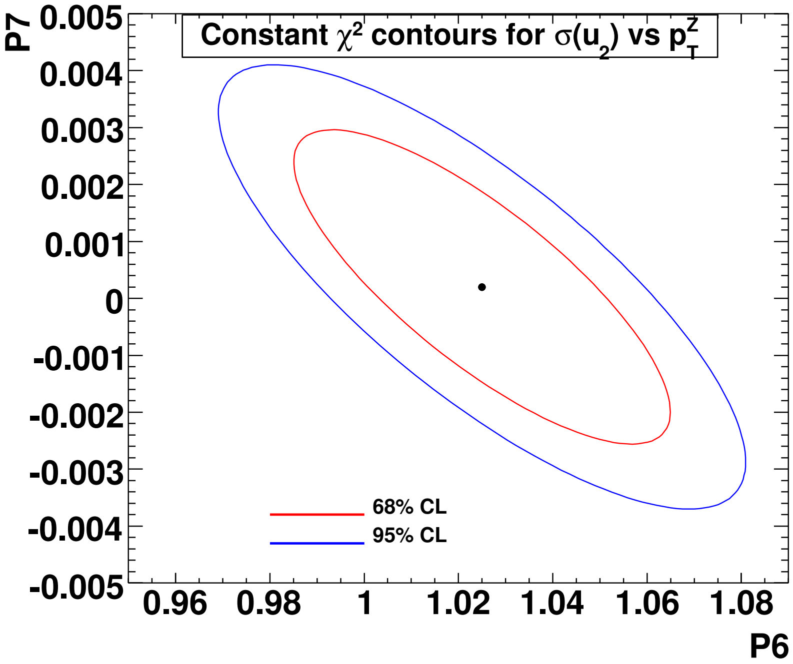

Figure 42: Constant χ^2 contours of the $\sigma(U_2)$ vs p_T^Z distribution in $\mathrm{Z} \rightarrow e^+e^-$ events as P_6 and P_7 are varied.

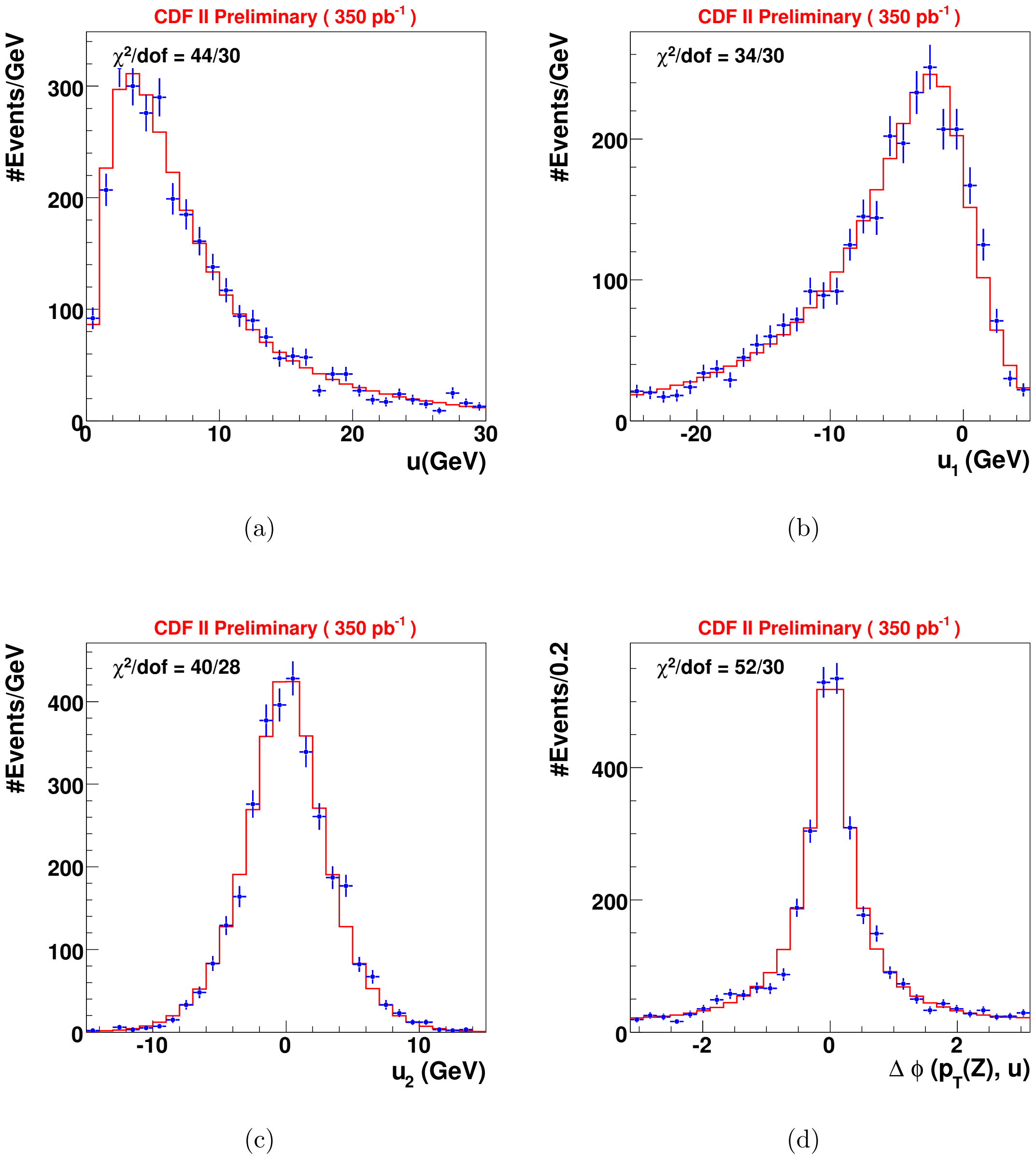

Figure 43: (a) U, (b) U_1, (c) U_2 and (d) $\Delta\phi(U, p_T^Z)$ for the Z $\rightarrow e^+e^-$ data compared to the best fit simulation.

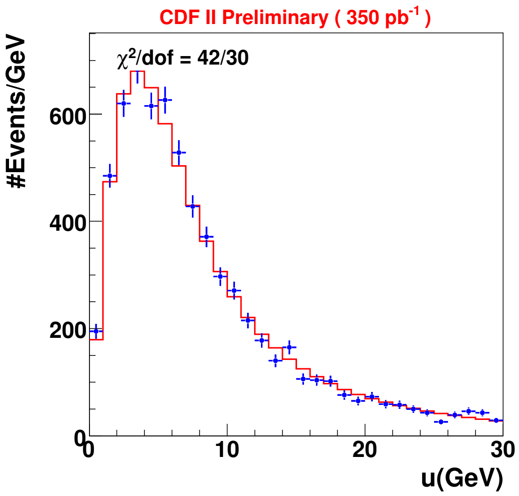

(a)

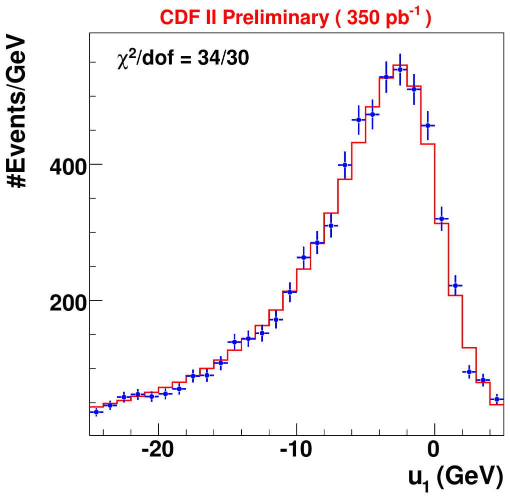

(b)

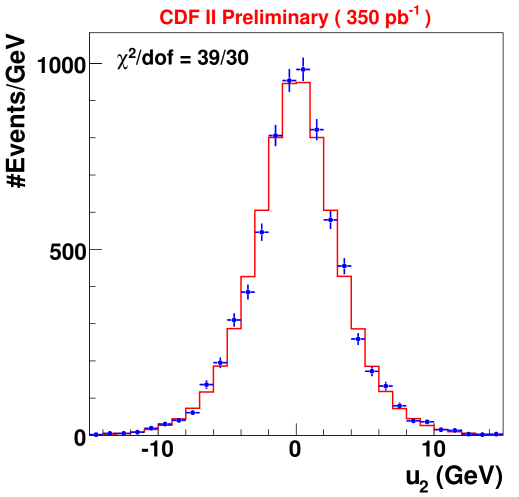

(c)

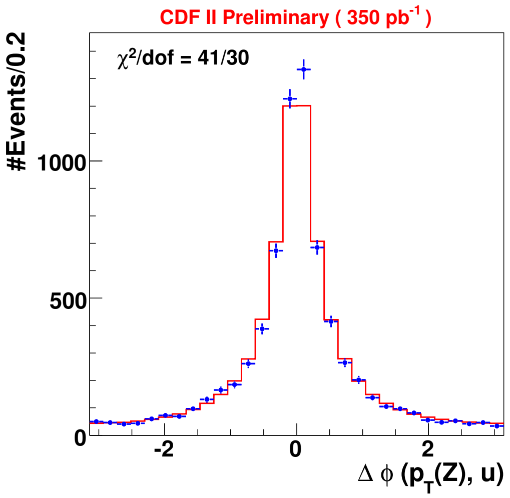

(d)

Figure 44: (a) U, (b) U_1, (c) U_2 and (d) $\Delta\phi(U, p_T^Z)$ for the Z $\rightarrow \mu^+\mu^-$ data compared to the best fit simulation.

The systematical uncertainty on Γ_W due to the uncertainty in the obtained recoil parameters is estimated by sampling the 7×7 covariance matrix 250 times to produce 250 M_T distributions. These are then fitted to the simulated data to obtain the distribution of the fitted Γ_W values. The distribution for a M_T^{cut} of 90 GeV is shown in Figure 45 for both the electron and muon fits. The uncertainties are listed in Table 34 for the different M_T^{cut} values.

M_T^{cut}[GeV]	$\Delta\Gamma_W$: electrons	$\Delta\Gamma_W$: muons
80	60 ± 3	53 ± 4 MeV
85	59 ± 3	51 ± 3 MeV
90	54 ± 3	49 ± 3 MeV
100	38 ± 2	30 ± 2 MeV
110	19 ± 1	14 ± 1 MeV

Table 34: The recoil systematic for five transverse mass cuts from the finite Z statistics.

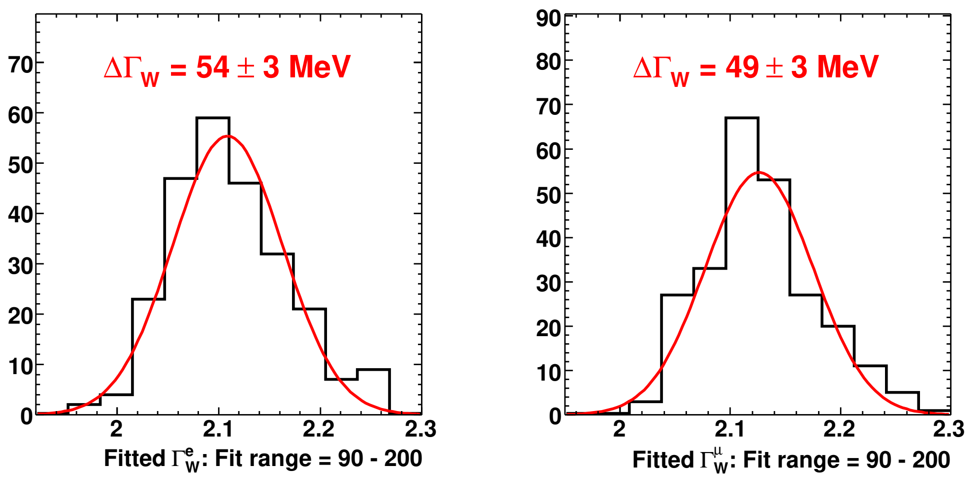

Figure 45: Distribution of fitted Γ_W values when the 7×7 recoil covariance matrix is sampled 250 times for $W \rightarrow e\nu$ (left) and $W \rightarrow \mu\nu$ (right). The distributions are fitted with a Gaussian.

11.5 Comparison to the W Data

The recoil model obtained by fitting to Z data is applied to the W sample. All background contributions are added to the simulation for comparisons between data and simulation. The $\not\!\!E_T$ distribution for W $\rightarrow$ eν and W $\rightarrow$ $\mu\nu$ data compared to the simulation is shown in Figure 46. Figures 47, 48 and 49 show the distributions of U, $U_{||}$ and $U_\perp$ for W $\rightarrow$ eν and W $\rightarrow$ $\mu\nu$ events. The variation of $\langle U_{||}\rangle$ with M_T, U and $\Delta\phi$ (U,ℓ) is shown in Figures 50, 51 and 52. The variation of the RMS of $U_\perp$ with U is shown in Figure 53. The distributions show good agreement between data and simulation.

The χ^2 for these distributions reflect the statistical uncertainty only. However, propagating systematic uncertainties from the p_T^Z distribution, backgrounds and the recoil parameterisation improves the χ^2 agreement of the plots. For instance, the χ^2/dof of the U distribution in W $\rightarrow$ eν events goes from 86/40 to 56/40 and that in W $\rightarrow$ $\mu\nu$ events goes from 52/40 to 37/40. By far the largest systematic uncertainty on the shape of the U distribution is the recoil parameter determination uncertainty (see Figure 54). It is obtained by sampling the covariance matrix of the parameters and estimating the spread (RMS) of the variations in each bin. The uncertainty on the determination of the p_T^Z parameters is also significant, while the uncertainty on the U shape due to backgrounds is negligible.

It can be shown that the statistical uncertainty on the U distribution in W $\rightarrow$ eν can be reduced by using a different choice of recoil parameters, ones that minimise the χ^2 of the U distribution whilst maintaining a good description of the recoil in Z $\rightarrow$ e^+e^- events. This set of 'U optimised' recoil parameters is obtained by selecting a set from the sampling of the Z $\rightarrow$ e^+e^- covariance that gives the best description of U. Figures 55 and 56 show that the 'U optimised' set of parameters reduces the overall χ^2 of the W distributions whilst still giving a reasonable description of the main Z $\rightarrow$ e^+e^- distributions.

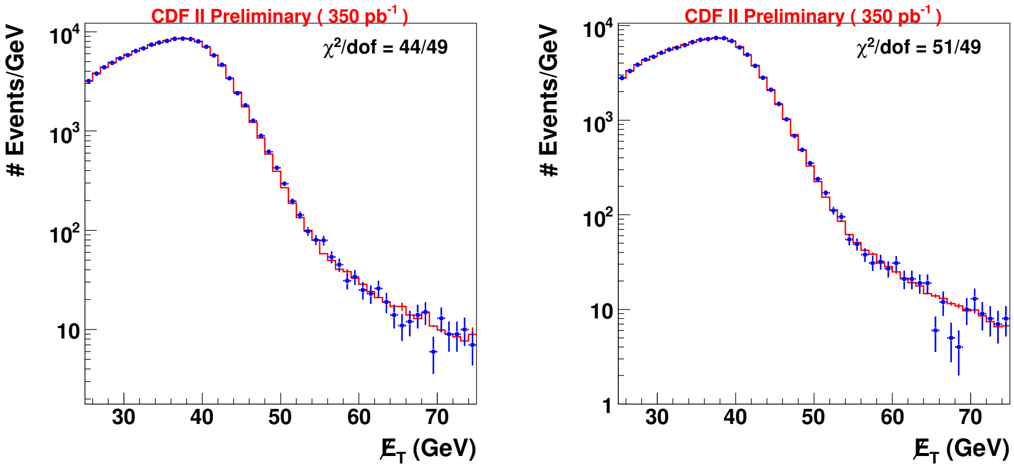

(a) (b)

Figure 46: $\not{E}_T$ for (a) W $\rightarrow e\nu$ and (b) W $\rightarrow \mu\nu$ data compared to the simulation.

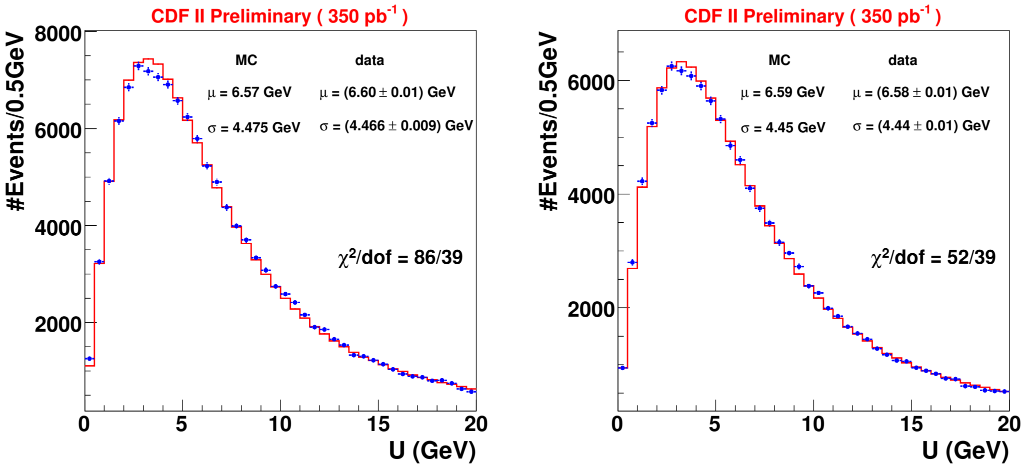

(a) (b)

Figure 47: U for (a) W $\rightarrow e\nu$ and (b) W $\rightarrow \mu\nu$ data compared to the simulation.

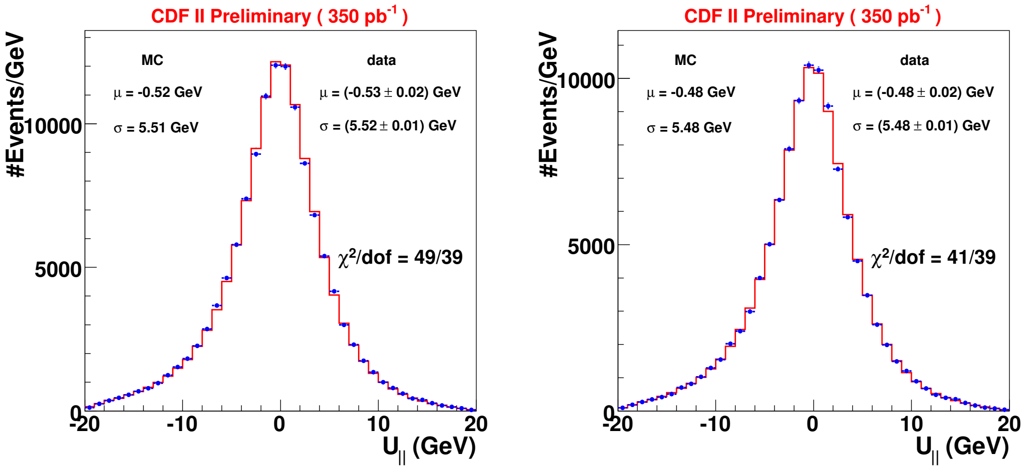

(a) (b)

Figure 48: $U_{||}$ for (a) W $\rightarrow$ eν and (b) W $\rightarrow \mu\nu$ data compared to the simulation.

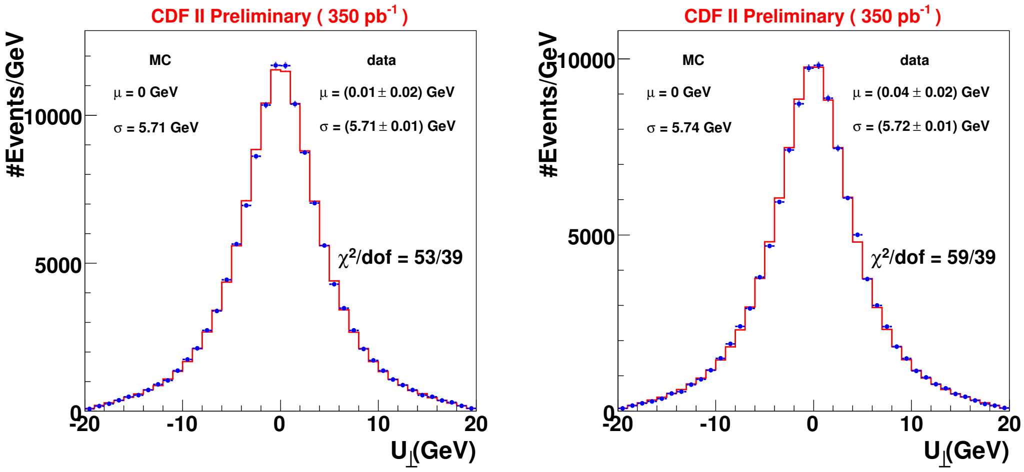

(a) (b)

Figure 49: $U_{\perp}$ for (a) W $\rightarrow$ eν and (b) W $\rightarrow \mu\nu$ data compared to the simulation.

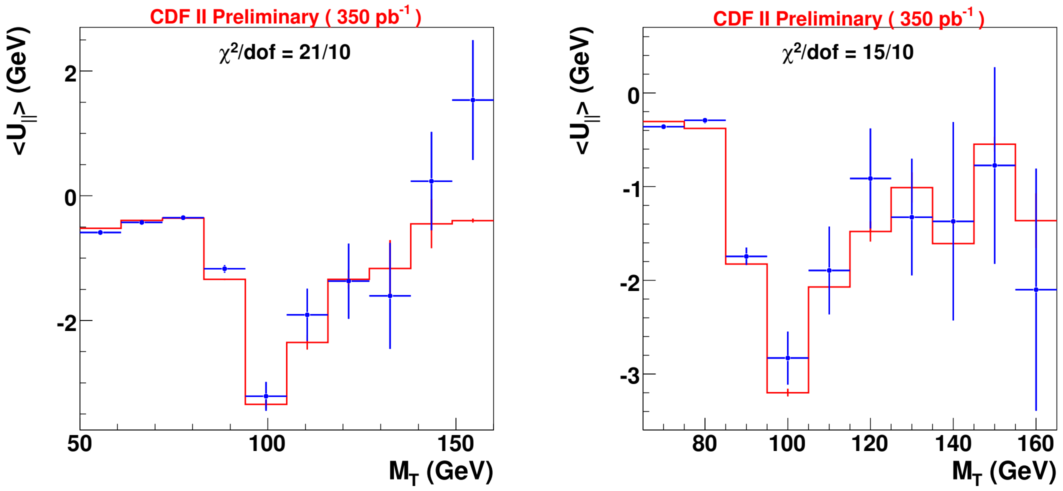

(a) (b)

Figure 50: Variation of the mean of $U_{||}$ with M_T for (a) W $\rightarrow e\nu$ and (b) W $\rightarrow \mu\nu$ data compared to the simulation.

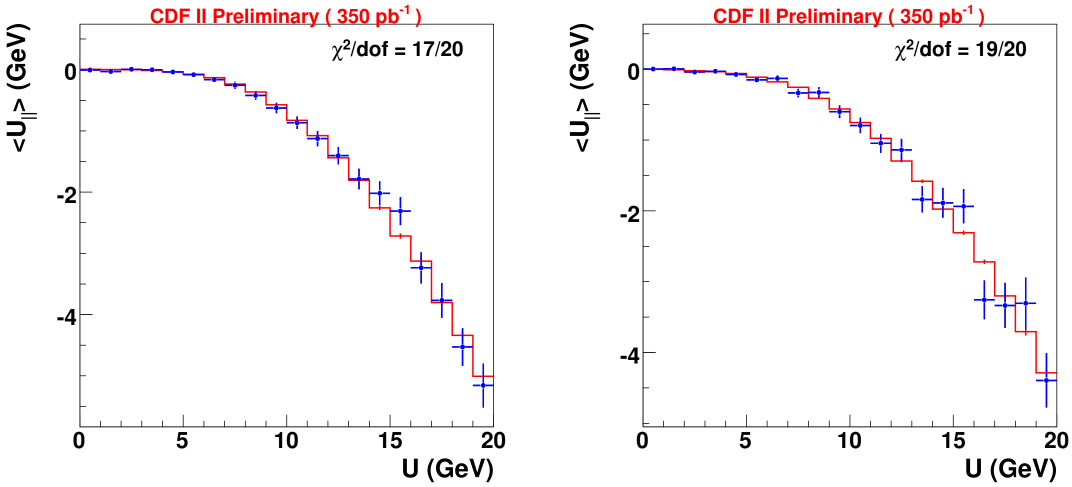

(a) (b)

Figure 51: Variation of the mean of $U_{||}$ with U for (a) W $\rightarrow e\nu$ and (b) W $\rightarrow \mu\nu$ data compared to the simulation.

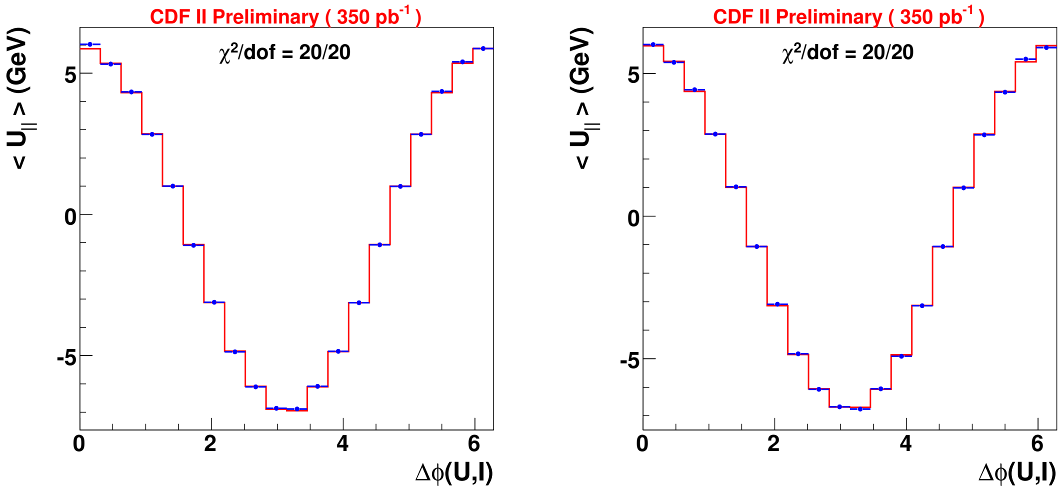

(a) (b)

Figure 52: Variation of the mean of $U_{||}$ with $\Delta\phi$ $(U,\ell^{\pm})$ for (a) W $\rightarrow$ eν and (b) W $\rightarrow$ $\mu\nu$ data compared to the simulation.

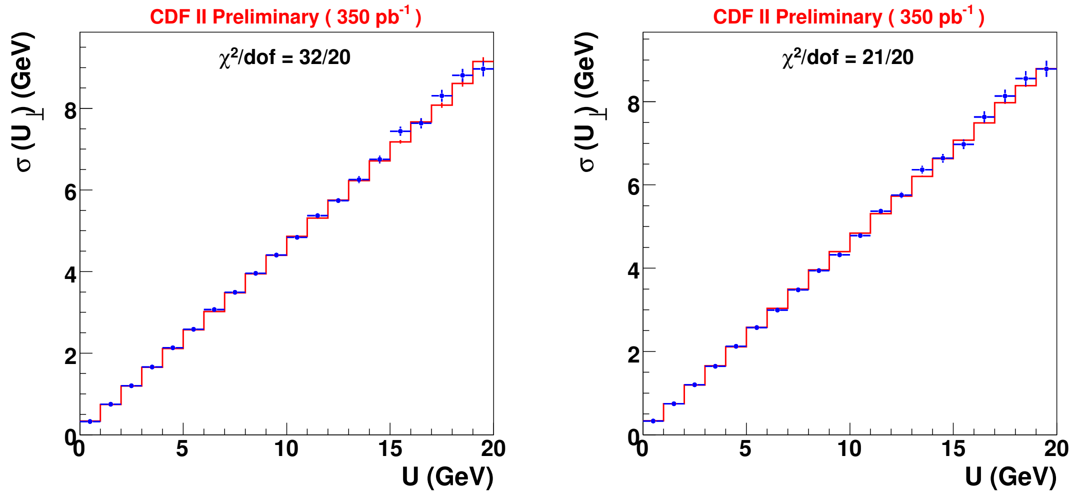

(a) (b)

Figure 53: Variation of the RMS of $U_\perp$ with U for (a) W $\rightarrow$ eν and (b) W $\rightarrow$ $\mu\nu$ data compared to the simulation.

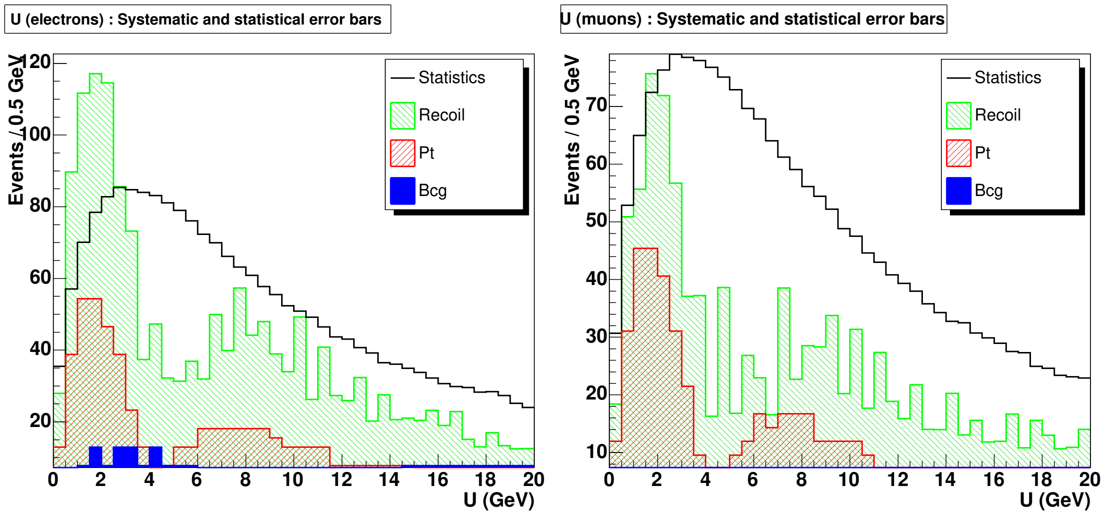

(a) (b)

Figure 54: The U distribution shape uncertainties due to statistics, recoil parameter determination, p_T^Z parameterisation and backgrounds for (a) $\mathrm{W} \to e\nu$ and (b) $\mathrm{W} \to \mu\nu$.

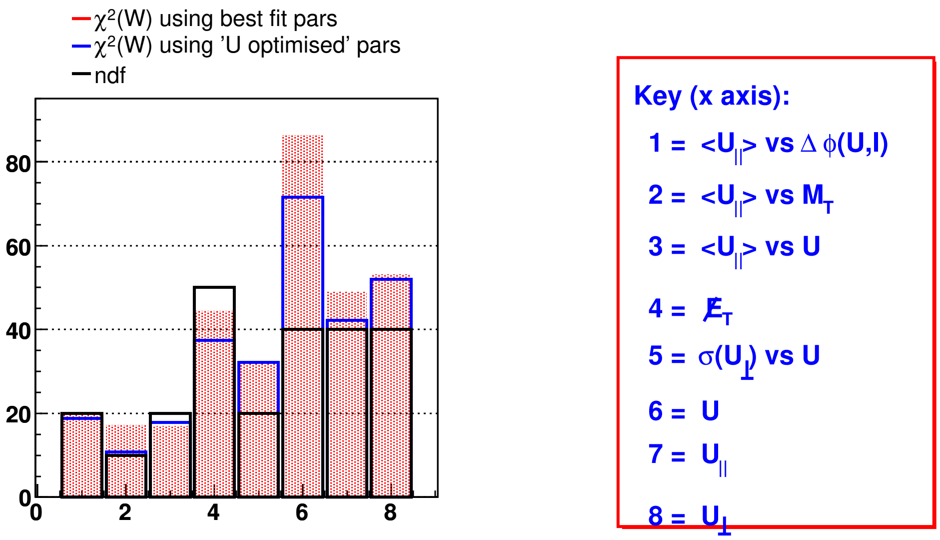

Figure 55: The effect on the χ^2 of the key $\mathrm{Z} \rightarrow e^+e^-$ distributions when using the recoil parameters optimised on the U distribution.

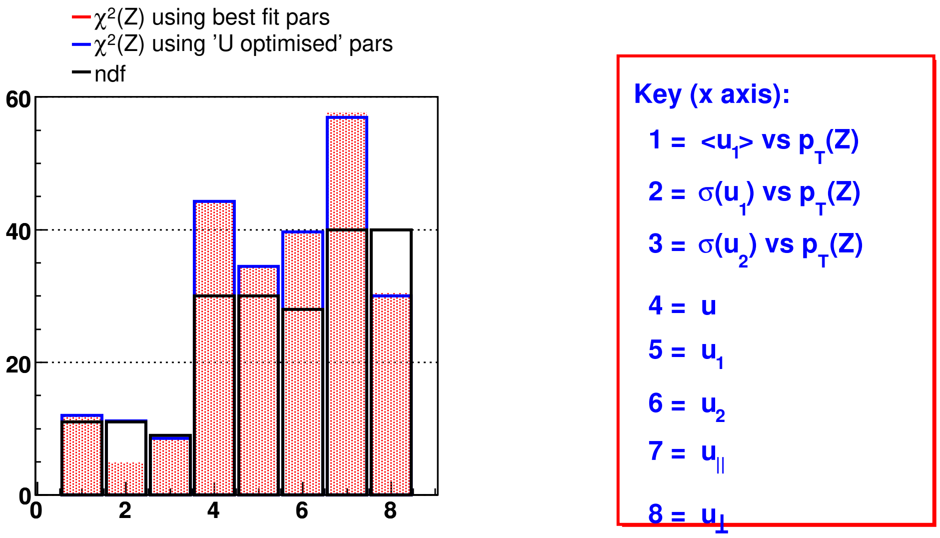

Figure 56: The effect on the χ^2 of the key $\mathrm{W} \rightarrow e\nu$ distributions when using the recoil parameters optimised on the U distribution.

12 Backgrounds

Backgrounds in the W data affect the M_T line-shape and can therefore bias the fitted Γ_W. The background normalisations and M_T distributions are obtained and added to the Monte Carlo templates used in the Γ_W fit.

The backgrounds to both $W \to e\nu$ and $W \to \mu\nu$ events fall into two categories: electroweak and non-electroweak. Electroweak backgrounds consist of $W \to \tau\nu$ events where the τ decays to an electron or a muon and Z/γ^* events where the Z/γ^* decays leptonically. These backgrounds are found using CdfSim. The signal and background processes are generated and passed through the W event selection The relative acceptance is combined with the relative cross-section to give the expected background. For $W \to \tau\nu$ backgrounds the cross-section is the same as signal events. For Z/γ^* backgrounds the events are generated with $M_{Z/\gamma^*} > 20$ GeV, but the denominator in the acceptance ratio only includes events with $66 < M_{Z/\gamma^*} <116$ GeV. The cross-section for Z/γ^* production with $66 < M_{Z/\gamma^*} <116$ GeV is effectively the same as the cross-section for pure Z production, making it possible to use the NNLO calculation of the ratio between the $W \to \ell\nu$ and $Z \to \ell^+\ell^-$ cross-sections: $R = 10.67 \pm 0.15$ [44]. The uncertainty on R gives an uncertainty on the measured backgrounds. As described in Section 2 a veto on an additional $p_T > 20$ GeV track is made in the W event selection. This veto is modelled in CdfSim, how-ever CdfSim is known to over-estimate the forward tracking efficiency. A scale-factor (ratio between the tracking efficiency in data and that in CdfSim) has been measured [45] and is applied to the vetoed tracks in CdfSim. The scale factor is 0.661 ± 0.013 for tracks with $R_{COT} < 83$ cm and $0.754 + (0.0017 \pm 0.0006)\times R_{COT}$ for tracks with $83 < R_{COT} < 132$ cm. The uncertainty on these numbers gives an uncertainty on the measured background, which will be denoted SF.

12.1 Electroweak Backgrounds: Muons

12.1.1 $Z \to \mu^+\mu^-$ Background

$Z \to \mu^+\mu^-$ events where only one of the muons is reconstructed in the detector can mimic $W \to \mu\nu$ events. The missing momentum due to the missing muon leg will give a high $\not\!\!E_T$ measurement. The background is found to be $(5.66 \pm 0.08_{R} \pm 0.02_{STAT} \pm 0.18_{SF})\%$. Figure 57 shows the M_T distribution of background $Z \to \mu^+\mu^-$ events using CdfSim. Due to limited statistics the distribution is fitted with a Landau in the region $90 < M_T < 200$ GeV, the M_T distribution added to the M_T templates then consists of the histogram in the region $50 < M_T < 90$ GeV and the Landau function in the region $90 < M_T < 200$ GeV. The uncertainty on the width, summarised in Table 35 for the different M_T^{cut} values, comes from using the M_T distribution and background normalisation obtained when the

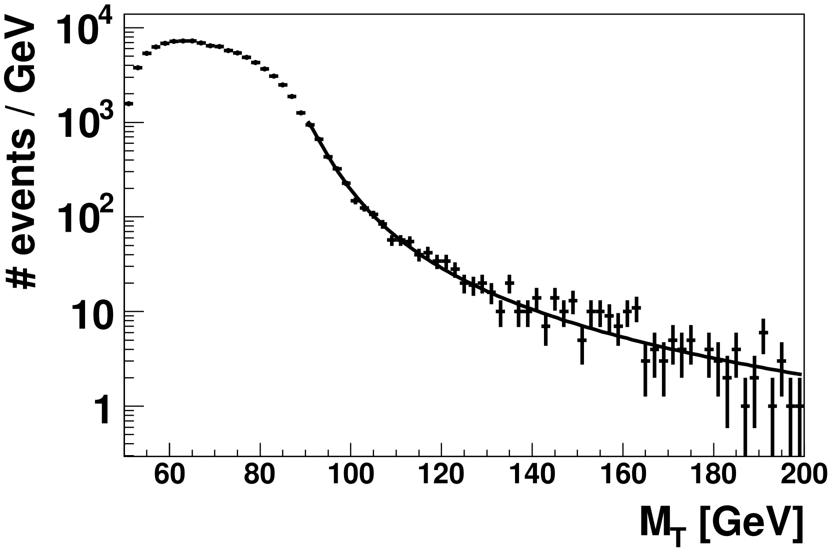

Figure 57: The distribution of M_T in $Z \to \mu^+\mu^-$ events found from CdfSim. The distribution is fitted with a Landau in the region $90 < M_T < 200$ GeV.

track efficiency scale-factor is varied within its uncertainty.

M_T^{cut} [GeV]	$\Delta\Gamma_W$
80	16 MeV
85	17 MeV
90	14 MeV
100	5 MeV
110	3 MeV

Table 35: Systematic uncertainties on Γ_W due to the $Z \to \mu^+\mu^-$ background.

12.1.2 $Z \to \tau^+\tau^-$ Background

$Z \to \tau^+\tau^-$ events where one of the τs decays to a $\mu\nu$ pair can mimic $W \to \mu\nu$ events. The background is found to be $(0.115 \pm 0.002_{\mathrm{R}} \pm 0.001_{\mathrm{STAT}})\%$. The uncertainty from the forward tracking scale-factor is negligible. The M_T distribution, shown in Figure 58(a), is taken from CdfSim. The effect on Γ_W due to the $Z \to \tau^+\tau^-$ background amount and shape is negligible for all fit ranges.

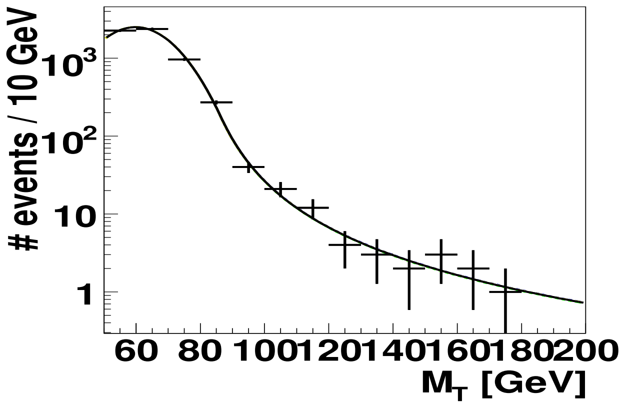

(a)

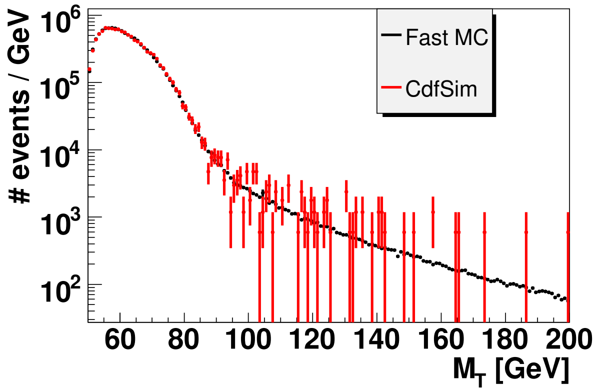

(b)

Figure 58: (a) The distribution of M_T in $Z \rightarrow \tau^+\tau^-$ events found from CdfSim. The distribution is fitted with a Gaussian in the region $50 < M_T < 85$ GeV and a Landau in the region $85 < M_T < 200$ GeV. (b) The distribution of M_T in $W \rightarrow \tau\nu$ events from CdfSim and the fast Monte Carlo.

12.1.3 $W \rightarrow \tau\nu$ Background

$W \rightarrow \tau\nu$ events where the τ decays to a $\mu\nu$ pair can mimic $W \rightarrow \mu\nu$ events. A background of $(1.98 \pm 0.01_{\mathrm{STAT}})\%$ is found from CdfSim. The $W \rightarrow \tau\nu$ background can also be found in the same way from the fast Monte Carlo, where a background of 1.98% is also found. Figure 58(b) shows the M_T distribution in $W \rightarrow \tau\nu$ events obtained from CdfSim and the fast simulation. The fast simulation distribution is used in the Γ_W fits due to the larger statistics and the CdfSim distribution is used to establish a systematic uncertainty. The effect on Γ_W due to the $W \rightarrow \tau\nu$ background normalisation and shape is negligible for all fit ranges.

12.2 Electroweak Backgrounds: Electrons

12.2.1 $Z \rightarrow e^+e^-$ Background

$Z \rightarrow e^+e^-$ events where only one of the electrons is reconstructed in the detector can mimic $W \rightarrow e\nu$ events. If the other electron goes into an un-instrumented region of the detector a high $\not{E}_T$ could be measured. The background is found to be $(0.167 \pm 0.002_{\mathrm{R}} \pm 0.003_{\mathrm{STAT}} \pm 0.005_{\mathrm{SF}})\%$. Figure 59 shows the M_T distribution, also taken from CdfSim. The effect on Γ_W due to the $Z \rightarrow e^+e^-$ background normalisation and shape (taken from the fit parameter uncertainties and by varying the track efficiency scale-factor) is negligible for all fit ranges.

12.2.2 $Z \rightarrow \tau^+\tau^-$ Background

$Z \rightarrow \tau^+\tau^-$ events where one of the τs decays to a $e\nu$ pair can mimic $W \rightarrow e\nu$ events. The background is found to be $(0.123 \pm 0.001_{\mathrm{R}} \pm 0.001_{\mathrm{STAT}})\%$. The uncertainty from the forward tracking scale-factor is negligible. Figure 60(a) shows the M_T distribution, also taken from CdfSim. The effect on Γ_W due to the $Z \rightarrow \tau^+\tau^-$ background normalisation and shape (taken from the fit parameter uncertainties) is negligible for all fit ranges.

12.2.3 $W \rightarrow \tau\nu$ Background

$W \rightarrow \tau\nu$ events where the τ decays to a $e\nu$ pair can mimic $W \rightarrow e\nu$ events. This background is found with CdfSim by generating $W \rightarrow e\nu$ and $W \rightarrow \tau\nu$ events and passing them through the $W \rightarrow e\nu$ event selection. A background of $2.04 \pm 0.01_{\mathrm{STAT}}\%$ is found. The $W \rightarrow \tau\nu$ background can be found in the same way from the fast Monte Carlo, where a background of 2.01% is found. Thus $2.04 \pm 0.03\%$ is taken as the background, which covers both measurements. Figure 60(b) shows the M_T distribution in $W \rightarrow \tau\nu$ events obtained from CdfSim and the fast simulation. The fast simulation distribution is used due to the larger statistics. The difference between the two is taken a systematic. The effect on Γ_W due to the $W \rightarrow \tau\nu$ background normalisation is negligible for all fit ranges. Table 36 summarises $\Delta\Gamma_W$ due to the $W \rightarrow \tau\nu$ shape.

$M_T^{\rm cut}$ [GeV]	$\Delta\Gamma_W$
80	3 MeV
85	3 MeV
90	3 MeV
100	5 MeV
110	8 MeV

Table 36: Systematic uncertainties on Γ_W due to the W $\rightarrow \tau\nu$ background.

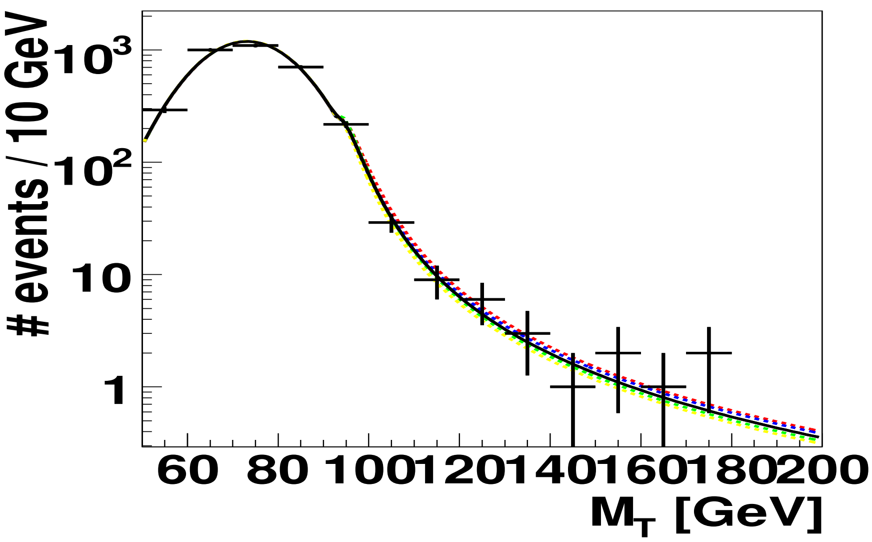

Figure 59: The distribution of M_T in Z $\rightarrow e^+e^-$ events found from CdfSim, fitted to Gaussian in the region $M_T < 95$ GeV and a Landau in the region $M_T > 95$ GeV.

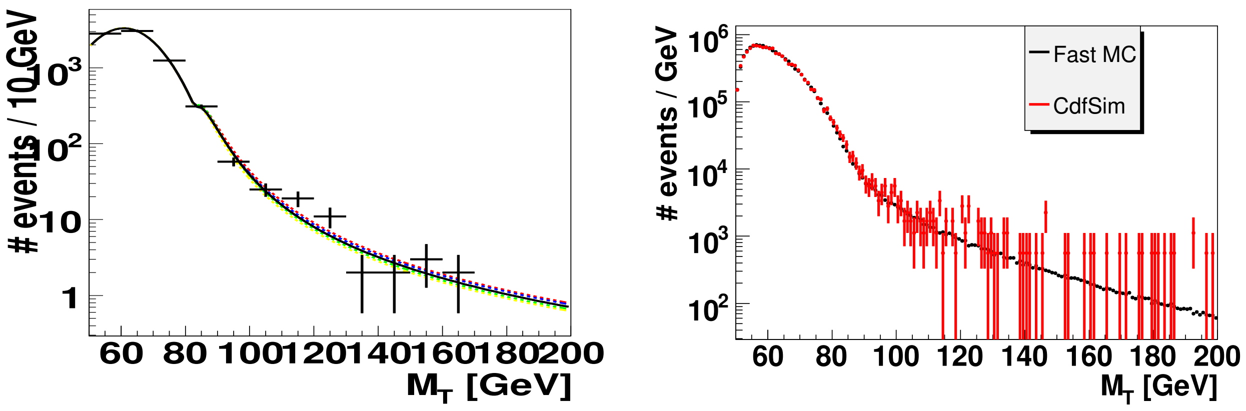

(a) (b)

Figure 60: (a) The distribution of M_T in $Z \rightarrow \tau^+\tau^-$ events found from CdfSim. The distribution is fitted with a Gaussian in the region $50 < M_T < 83$ GeV and a Landau in the region $83 < M_T < 200$ GeV. (b) The distribution of M_T in $W \rightarrow \tau\nu$ events from CdfSim and the fast Monte Carlo.

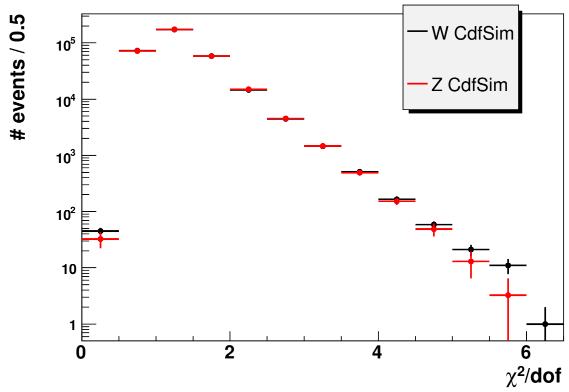

(a)

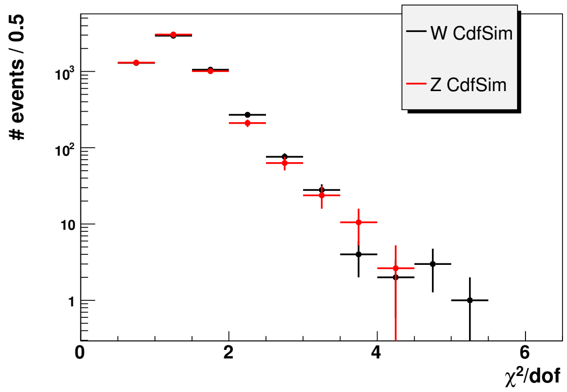

(b)

Figure 61: The χ^2_{track}/dof distribution for muons in CdfSim W $\rightarrow \mu\nu$ and Z $\rightarrow \mu^+\mu^-$ events for (a) tracks with silicon hits and (b) tracks without silicon hits.

12.3 Decay in-flight Background

Kaons and pions produced in p$\bar{\text{p}}$ collisions decay into a $\mu\nu$ pair 63.4% and 99.99% of the time respectively. The decay length for kaons is $c\tau = 3.7$ m and that for pions is $c\tau = 7.8$ m. If such a meson decays within the COT, a track with a kink at the point of the decay will be reconstructed. Although the p_T of muons in such events is usually much lower than that of muons in W $\rightarrow \mu\nu$ events, it is possible that the kink in the track gives a fake high p_T measurement. This mis-measurement can also lead to a high measured $\not{E}_T$.

Decay in-flight muons will tend to have a large d_0 as well as a large χ^2_{track}/dof due to the kink in the track. The amount of decay in-flight background is found by fitting the χ^2_{track}/dof distribution in the candidate sample to that expected from pure W $\rightarrow \mu\nu$ events added to that expected from decay in-flight events. The fraction of decay in-flight events is varied and the χ^2 of the fit is minimised. The fractional background after making the χ^2_{track}/dof cut is then found. This is done separately for muon tracks with and without silicon hits. Z $\rightarrow \mu^+\mu^-$ events, where the level of background is negligible, are used to get the χ^2_{track}/dof distribution of muons in W $\rightarrow \mu\nu$ events. In order to demonstrate that the χ^2_{track}/dof distribution in W $\rightarrow \mu\nu$ muons is sufficiently described by the χ^2_{track}/dof distribution in Z $\rightarrow \mu^+\mu^-$ muons, Figure 61 shows the distribution for Z $\rightarrow \mu^+\mu^-$ and W $\rightarrow \mu\nu$ events in CdfSim.

A sample rich in decay in-flight events is selected by reversing the d_0 cut in the W $\rightarrow \mu\nu$ sample. Figure 62 shows the mean χ^2_{track}/dof as a function of d_0 for decay in-flight events,

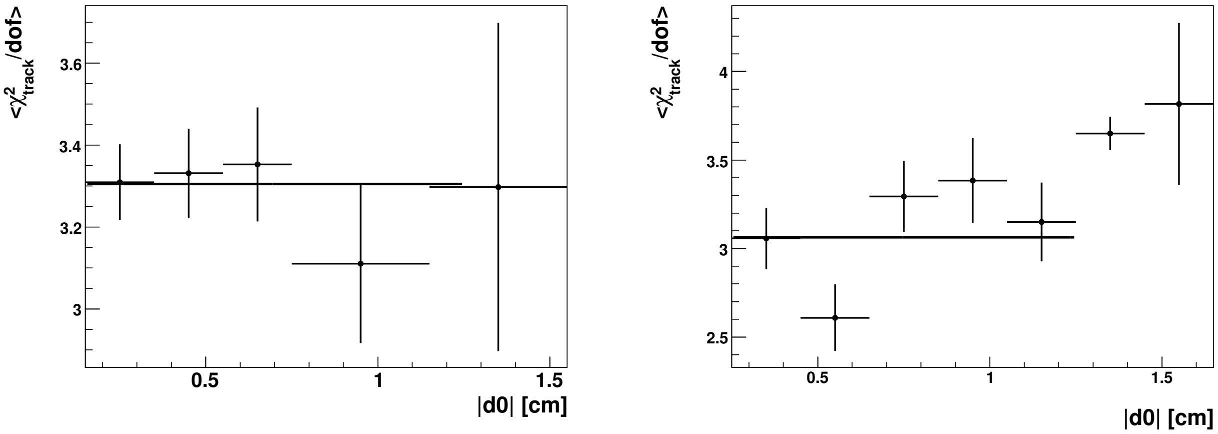

(a) (b)

Figure 62: $<\chi^2_{track}/dof>$ versus d_0 for muons in the W $\rightarrow \mu\nu$ event sample without χ^2_{track}/dof or d_0 cuts applied for (a) tracks with silicon hits and (b) tracks without silicon hits. The distributions have been fitted with a first order polynomial to show that they are consistent with flat in the region used to select decay in-flight events. $<\chi^2_{track}/dof>$ in the signal region is 1.27.

which are defined as events passing all the W $\rightarrow \mu\nu$ cuts except the χ^2_{track}/dof cut and with $d_0 > 0.15(0.25)$ cm for silicon(no silicon) tracks. The cuts $0.15 < |d_0| < 1.25$ cm ($0.25 < |d_0| < 1.25$ cm) are made to select decay in-flight events for tracks with(out) silicon hits since the mean χ^2_{track}/dof is constant within these ranges. The results of the fits, shown in Figure 63, give a background of $(0.113 \pm 0.047)\%$ for tracks with silicon hits and $(0.46 \pm 0.17)\%$ for tracks without silicon hits. 6.2% of events have a muon track with no silicon hits, therefore the total decay in-flight background is $(0.135 \pm 0.045)\%$. This background is measured with respect to W $\rightarrow \mu\nu$ events and all other backgrounds in the sample. After correcting for the other 8.045% backgrounds the decay in-flight background with respect to pure W $\rightarrow \mu\nu$ events is $(0.145 \pm 0.049)\%$.

As well as measuring a value for the fractional decay in-flight background, it is also necessary to obtain the M_T distribution. Figure 64(a) shows the M_T distribution of decay in-flight events selected by relaxing the CMP dx, CMU dx and CMX dx cuts and requiring $0.25 < |d_0| < 0.6$ cm. A Landau functional form is fitted to the distribution: this function is added to the M_T Γ_W templates. In order to account for any bias in the M_T distribution from reversing the d_0 cut, the cut is changed to $0.6 < |d_0| < 1.2$ cm and the procedure is repeated. Figure 64(b) shows the M_T distribution using this d_0 cut. The

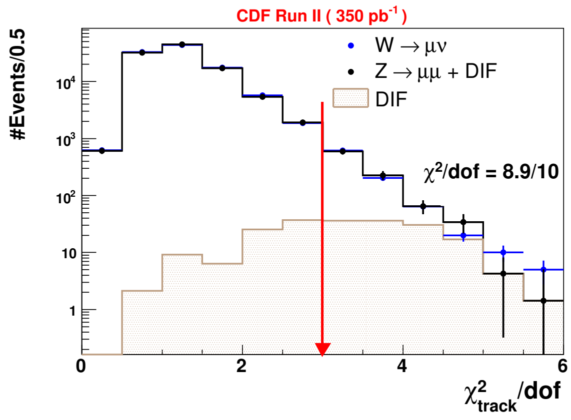

(a)

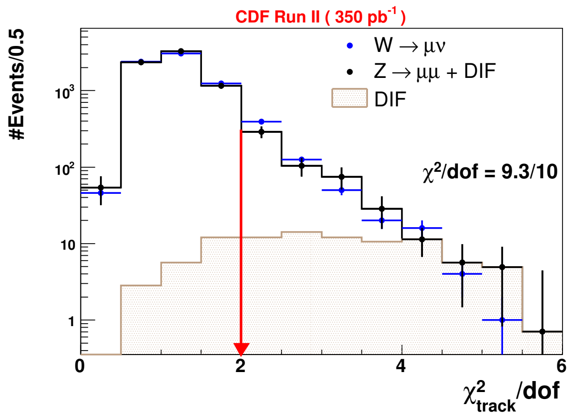

(b)

Figure 63: The distribution of χ^2_{track}/dof in W $\to \mu\nu$ events fitted to that in Z $\to \mu^+\mu^-$ events plus that in decay in-flight events. (a): Tracks with silicon hits, when the χ^2_{track}/dof cut of 3 is made the remaining fractional decay in-flight background is $(0.113 \pm 0.047)\%$. (b): Tracks without silicon hits, when the χ^2_{track}/dof cut of 2 is made the remaining fractional decay in-flight background is $(0.46 \pm 0.17)\%$.

systematic uncertainty on Γ_W due to the decay in-flight background consists of an uncertainty on the background normalisation and an uncertainty on the M_T distribution. The former is found by allowing the background normalisation to vary within its uncertainty when adding the M_T distribution to the templates; the latter is found by allowing the fit parameters of the functional form to vary by their uncertainties (the combination of fit parameter errors that gives the largest deviation to the width is used) and by using the M_T distribution obtained from the varied d_0 cut. Table 37 summarises these uncertainties for the different $\Delta\Gamma_W$ fit ranges.

M_T^{cut} [GeV]	$\Delta\Gamma_W^{\text{norm}}$	$\Delta\Gamma_W^{M_T}$[fit params]	$\Delta\Gamma_W^{M_T}$[d_0 cut]	$\Delta\Gamma_W$[total]
80	15 MeV	8 MeV	6 MeV	18 MeV
85	18 MeV	9 MeV	10 MeV	22 MeV
90	21 MeV	10 MeV	13 MeV	27 MeV
100	29 MeV	15 MeV	23 MeV	40 MeV
110	38 MeV	20 MeV	37 MeV	57 MeV

Table 37: Systematic uncertainties on Γ_W due to the decay in-flight background.

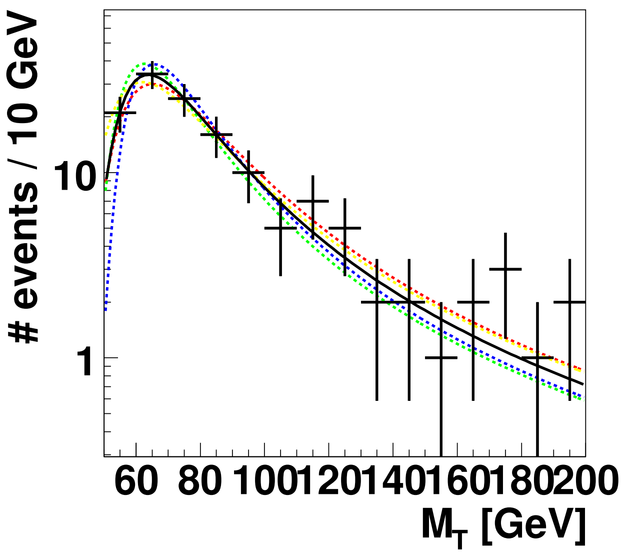

(a)

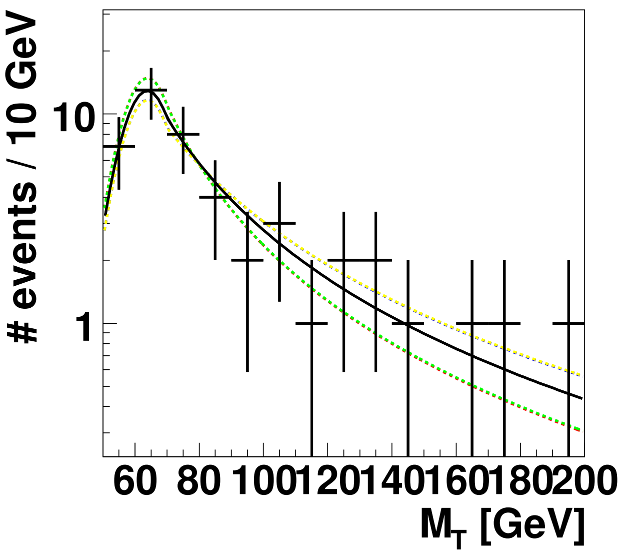

(b)

Figure 64: The distribution of M_T in decay in-flight events selected with: (a) $0.25 < |d_0| < 0.6$ cm (the histogram is fitted with a Landau), and (b) $0.6 < |d_0| < 1.2$ cm (the histogram is fitted with a functional form consisting of a Gaussian in the region $50 < M_T < 70$ GeV and a Landau in the region $70 < M_T < 200$ GeV). The dashed lines show the variations in the function when the parameters are varied within their uncertainties.

12.4 Multi-jet Background: Muons

Multi-jet events, where one of the jets contains or fakes a muon and where there is sufficient mis-measurement of energy in the calorimeter for the $\not{E}_T$ cut to pass, can mimic $\mathrm{W} \rightarrow \mu\nu$ events. The amount of multi-jet background is found by fitting the $\not{E}_T$ distribution, in the region 5–60 GeV, in the candidate sample to that expected from real $\mathrm{W} \rightarrow \mu\nu$ events and other electroweak backgrounds added to that expected from multi-jet events, with the fraction of multi-jet events varying. The $\not{E}_T$ and M_T cuts are removed for this purpose. The fit is performed for events where the muon track has silicon hits, in order to reduce the decay in-flight contamination. The χ^2 of the fit is minimised and the fractional background after making the $\not{E}_T$ cut is found. The $\mathrm{W} \rightarrow \mu\nu$ $\not{E}_T$ distribution is taken from the fast simulation. The other electroweak $\not{E}_T$ distributions are taken from CdfSim. The multi-jet $\not{E}_T$ distribution is taken from events that pass all the $\mathrm{W} \rightarrow \mu\nu$ cuts except the $\mathrm{E_{em}}$ and $\mathrm{E_{had}}$ cuts, which are loosened to their skimming values, and that fail a track isolation cut. The track isolation variable, $\Sigma_{cone0.4}(p_T)$, is the sum p_T of tracks within a cone $\Delta R < 0.4$ and within $|\Delta z_0| < 5$ cm of the muon track. This sample will be referred to as the 'anti-isolated' sample.

The $\not{E}_T$ distribution in the 'anti-isolated' sample is corrected for contamination from $\mathrm{W} \rightarrow \mu\nu$, $\mathrm{Z} \rightarrow \mu^+\mu^-$ and $\mathrm{W} \rightarrow \tau\nu$ events using CdfSim. The number of $\mathrm{W} \rightarrow \mu\nu$ events in the 'anti-isolated' sample is found by normalising the $\mathrm{W} \rightarrow \mu\nu$ CdfSim sample to the $\mathrm{W} \rightarrow \mu\nu$ data in the signal region, after correcting for backgrounds in the data. The number of $\mathrm{Z} \rightarrow \mu^+\mu^-$ and $\mathrm{W} \rightarrow \tau\nu$ events with respect to the number of $\mathrm{W} \rightarrow \mu\nu$ events in the 'anti-isolated' sample given by CdfSim is assumed to be correct.

Since $\not{E}_T$ and isolation may be correlated in multi-jet events, there is a possible bias in the multi-jet $\not{E}_T$ distribution obtained from the 'anti-isolated' sample. In order to take this bias into account the fitting procedure is repeated a number of times with the isolation cut varying. Figure 65(a) shows the $\not{E}_T$ distribution in the 'anti-isolated' sample, before and after correction from decay in-flight and electroweak contamination, when an isolation cut of $\Sigma_{cone0.4}(p_T) < 4$ GeV is used. Figure 65(b) shows the result of the corresponding fit from which a background of $(0.294 \pm 0.008)\%$ is found. Figure 66 shows the obtained fractional background as a function of the anti-isolation cut used to select multi-jet events. The uncertainty on each point comes from:

1. Allowing the fit χ^2 to vary by ± 1.

2. The uncertainty on the amount of electroweak contamination in the 'anti-isolated' sample. This is found by measuring the efficiency of selecting 'anti-isolated' muons in $\mathrm{Z} \rightarrow \mu^+\mu^-$ data and $\mathrm{Z} \rightarrow \mu^+\mu^-$ CdfSim. The ratio of these efficiencies is taken as a correction to the amount of electroweak contamination and the uncertainty on this ratio, from the limited statistics in the data, is taken as an uncertainty on the amount of electroweak contamination.

This distribution is fitted with a quadratic function and extrapolated into the signal region: an anti-isolation cut of 0 GeV. Since the quadratic flattens out in the region < 4 GeV, an anti-isolation cut of 4 GeV is used to select the multi-jet events. The 0.042% difference between the fit results at 4 GeV and 8 GeV, is taken as a systematic uncertainty on the extrapolation down to 0 GeV. Additional systematic uncertainties on the background are found from:

1. The uncertainty on the amount of electroweak contamination in the 'anti-isolated' sample as described above: $\pm$ 0.12%

2. Varying the decay in-flight background fraction within its uncertainty: $\pm$ 0.001%

3. Using CdfSim instead of the fast simulation to get the $\not\!\!E_T$ distribution in signal events: $\pm$ 0.02%

4. The relaxation of the M_T cut when fitting to the $\not\!\!E_T$ distribution. There are 0.06% more events in the W $\rightarrow \mu\nu$ data when the 50 GeV M_T mass cut is relaxed, which is taken as a systematic on the background estimation: $\pm$ 0.06%

The fractional multi-jet background is measured to be (0.29 $\pm$ 0.14) %.

As well as measuring a value of the fractional multi-jet background in W $\rightarrow \mu\nu$ events, it is also necessary to obtain the M_T distribution. Figure 67(a) shows the multi-jet M_T distribution obtained from the 'anti-isolated' sample with an isolation cut of 6 GeV. The distribution has been corrected for contamination from electroweak and residual decay in-flight events. The distribution has been fitted with a Gaussian in the region $50 < M_T < 90$ GeV and a Landau in the region $90 < M_T < 200$ GeV. Since M_T may be correlated with isolation in multi-jet events a systematic uncertainty on the M_T distribution is found from varying the anti-isolation cut from 6–12 GeV. Figure 67(b) shows the M_T fitted function for multi-jet events selected with various anti-isolation cuts. Additional uncertainties come from varying the fit parameters within their uncertainties and varying the amount of electroweak contamination in the 'anti-isolated' sample within its uncertainty Table 38 summarises these uncertainties for the different fit ranges.

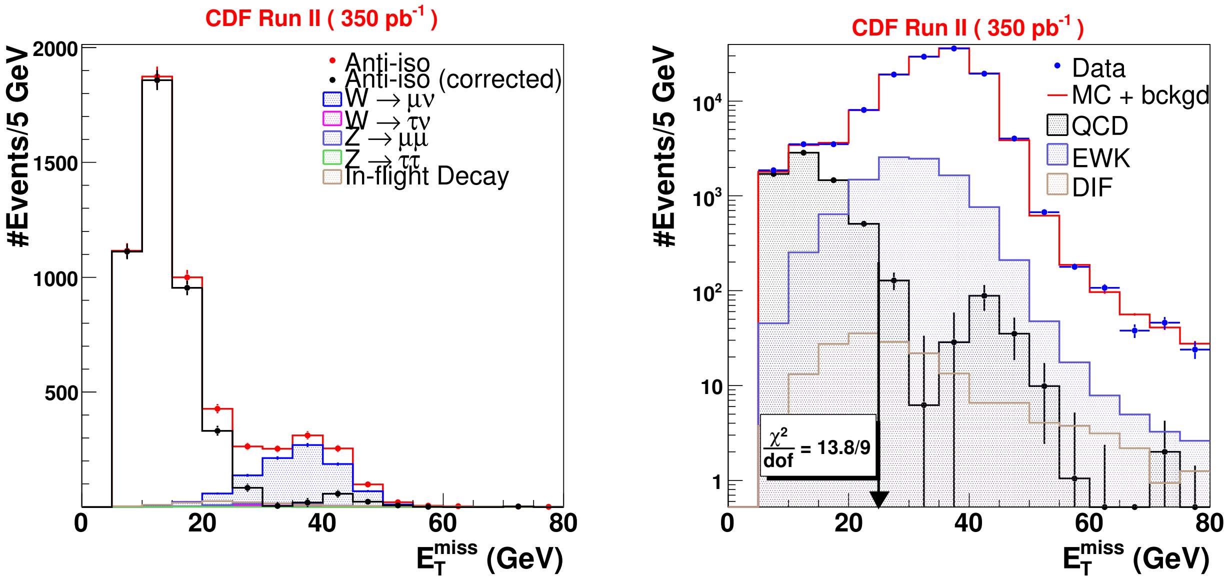

(a) (b)

Figure 65: (a): The $\not\!\!E_T$ distribution in the 'anti-isolated' sample with an anti-isolation cut of 4 GeV. The red histogram shows the distribution before correction from electroweak and decay in-flight contamination. (b): Results of the $\not\!\!E_T$ fit using the multi-jet $\not\!\!E_T$ distribution from (a).

$M_T^{\rm cut}$ [GeV]	$\Delta\Gamma_W^{\rm norm}$	$\Delta\Gamma_W^{M_T}$[fit pars]	$\Delta\Gamma_W^{M_T}$[iso cut]	$\Delta\Gamma_W^{M_T}$[EWK]	$\Delta\Gamma_W$[total]
80	3 MeV	5 MeV	3 MeV	3 MeV	7 MeV
85	3 MeV	5 MeV	5 MeV	3 MeV	8 MeV
90	4 MeV	5 MeV	10 MeV	2 MeV	12 MeV
100	7 MeV	7 MeV	13 MeV	3 MeV	17 MeV
110	9 MeV	9 MeV	16 MeV	4 MeV	21 MeV

Table 38: Systematic uncertainties on Γ_W due to the multi-jet background.

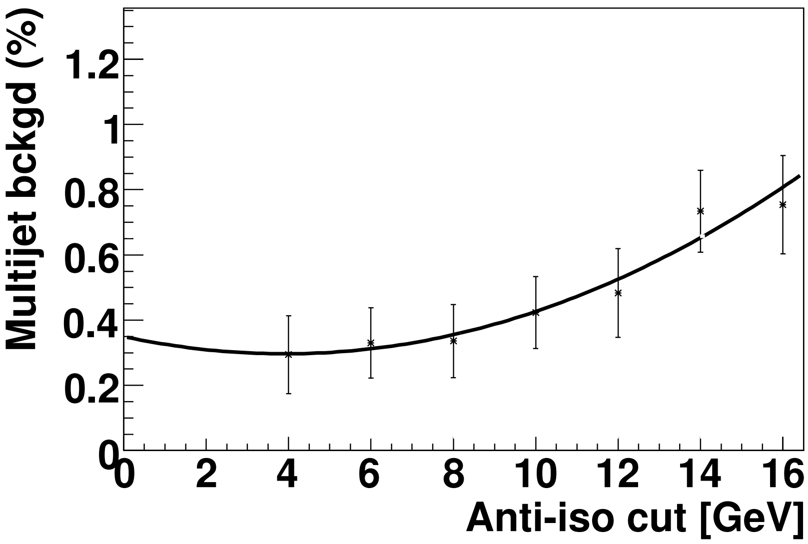

Figure 66: Fitted multi-jet background as a function of the anti-isolation cut used to obtain the multi-jet $\not{E}_T$ distribution.

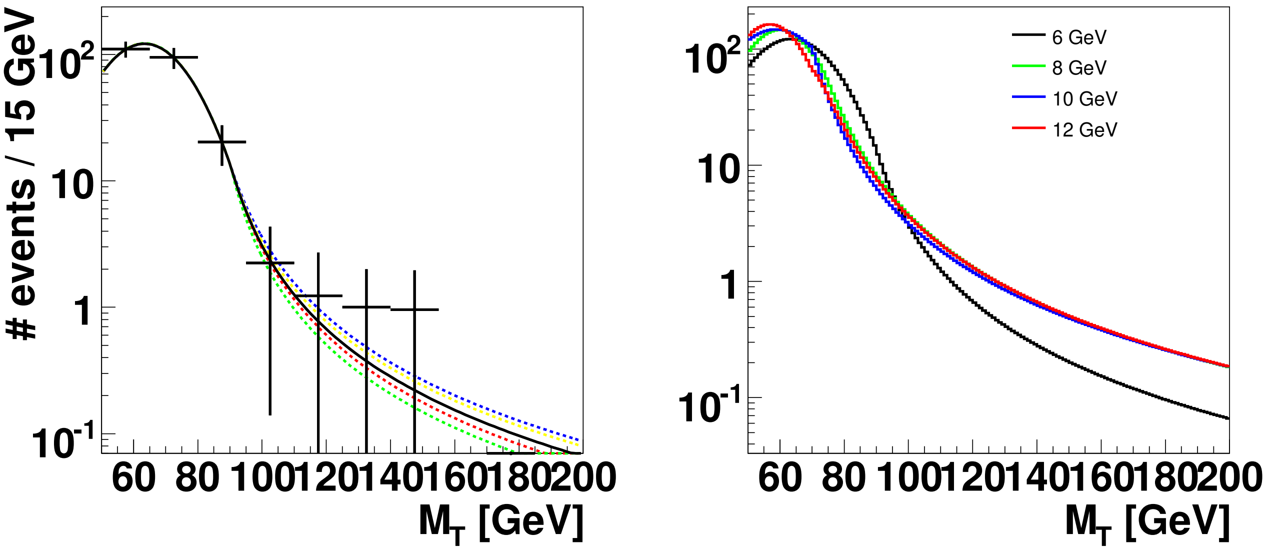

(a) (b)

Figure 67: (a): The M_T distribution in the 'anti-isolated' sample with an anti-isolation cut of 4 GeV. The histogram is fitted with a functional form consisting of a Gaussian in the region $50 < M_T < 90$ GeV and a Landau in the region $90 < M_T < 200$ GeV. The dashed lines show the variations in the function when the parameters are varied within their uncertainties (b): The M_T fitted function for different anti-isolation cuts.

12.5 Multi-jet Background: Electrons

Multi-jet events, where one of the jets contains or fakes an electron and where there is sufficient mis-measurement of energy in the calorimeter to pass the $\not\!\!E_T$ cut can mimic $\mathrm{W} \rightarrow \mathrm{e}\nu$ events. The amount of multi-jet background is found by fitting the $\not\!\!E_T$ distribution in the candidate sample to that expected from real $\mathrm{W} \rightarrow \mathrm{e}\nu$ events and other electroweak backgrounds added to that expected from multi-jet events, with the fraction of multi-jet events varying. The $\not\!\!E_T$ and M_T cuts are removed for this purpose. The χ^2 of the fit is minimised and the fractional background after making the $\not\!\!E_T$ cut is found. The $\mathrm{W} \rightarrow \mathrm{e}\nu$ $\not\!\!E_T$ distribution is taken from the fast simulation. The other electroweak $\not\!\!E_T$ distributions are taken from CdfSim. The multi-jet $\not\!\!E_T$ distribution is taken from a sample of events that pass all the event selection criteria for $\mathrm{W} \rightarrow \mathrm{e}\nu$ events except that:

1. The E/p cut is removed.
2. The $\mathrm{E_{had}/E_{em}}$ cut is relaxed to its skimming value: $\mathrm{E_{had}/E_{em}} < 0.125$.
3. At least two of the following anti-electron cuts are required to pass:
   - $\mathrm{E_{had}/E_{em}} > 0.07$
   - $|\Delta z| > 0.5$ cm
   - $\chi^2_{\mathrm{strip}} > 10$

This sample will be referred to as the ‘anti-electron’ sample.

The $\not\!\!E_T$ distribution in the ‘anti-electron’ sample is corrected for contamination from $\mathrm{W} \rightarrow \mathrm{e}\nu$, $\mathrm{Z} \rightarrow e^+e^-$, $\mathrm{W} \rightarrow \tau\nu$ and $\mathrm{Z} \rightarrow \tau^+\tau^-$ events using CdfSim. The number of $\mathrm{W} \rightarrow \mathrm{e}\nu$ events in the ‘anti-electron’ sample is found by normalising the $\mathrm{W} \rightarrow \mathrm{e}\nu$ CdfSim sample to the $\mathrm{W} \rightarrow \mathrm{e}\nu$ data in the signal region, after correcting for backgrounds in the data. CdfSim is not expected to get the ratio of the number of ‘anti-electrons’ to candidate electrons correct. This ratio can be measured in the $\mathrm{Z} \rightarrow e^+e^-$ data, where the level of multi-jet background is negligible. The first row in Table 39 gives the ratio of ‘anti-electrons’ to candidate electrons in $\mathrm{Z} \rightarrow e^+e^-$ data and CdfSim. The ratio of these ratios is taken as a correction to the number of electroweak events in the ‘anti-electron’ sample and the uncertainty on the ratio gives a systematic uncertainty on the background. Since the $\mathrm{W} \rightarrow \tau\nu$ and $\mathrm{Z} \rightarrow \tau^+\tau^-$ contamination in the ‘anti-electron’ sample is predominantly from τs that decay hadronically, the correction is not applied to $\mathrm{W} \rightarrow \tau\nu$ and $\mathrm{Z} \rightarrow \tau^+\tau^-$ events. An uncertainty on the amount of $\mathrm{W} \rightarrow \tau\nu$ and $\mathrm{Z} \rightarrow \tau^+\tau^-$ contamination of $2 \times$ the uncertainty on $\mathrm{W} \rightarrow \mathrm{e}\nu$ and $\mathrm{Z} \rightarrow e^+e^-$ contamination is used.

Figure 68(a) shows the $\not\!\!E_T$ distribution in the ‘anti-electron’ sample, before and after correction from electroweak contamination. Figure 68(b) shows the result of the fit. A multi-jet background of $(1.35 \pm 0.01_{\mathrm{STAT}})\%$ is found.

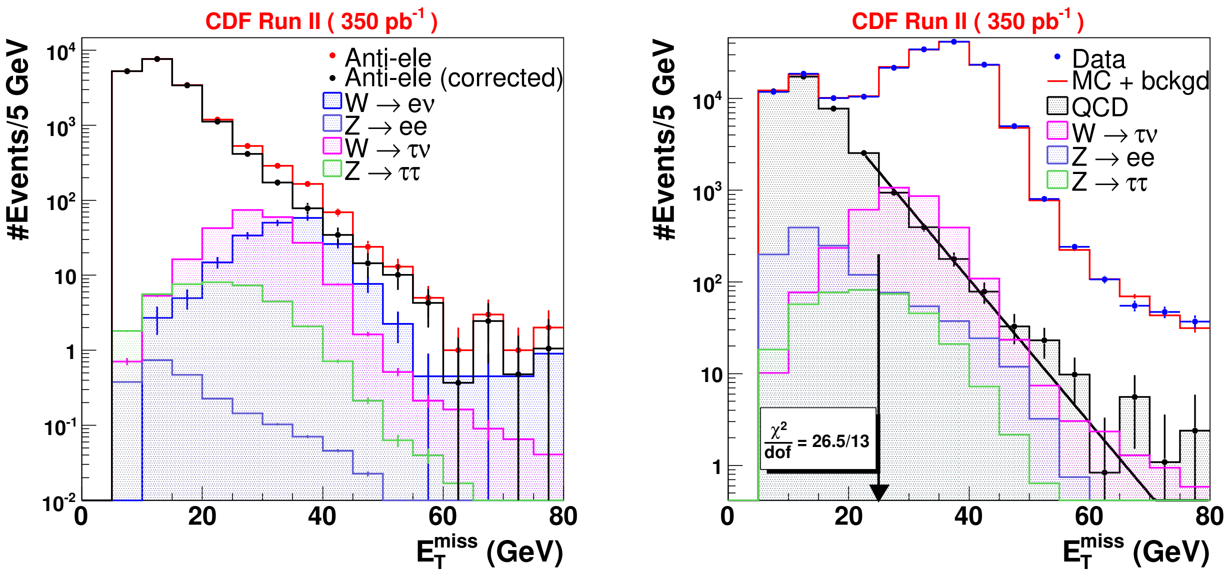

(a) (b)

Figure 68: (a) The $\not\!\!E_T$ distribution in the 'anti-electron' sample. The red histogram shows the distribution before correction from electroweak contamination. (b) Results of the $\not\!\!E_T$ fit using the multi-jet $\not\!\!E_T$ distribution from (a).

Anti-electron definition	ratio in data	ratio in CdfSim	ratio of ratios
Standard	$(0.17 \pm 0.05)\%$	$(0.068 \pm 0.009)\%$	2.50 ± 1.25
$\mathrm{E_{had}/E_{em}} > 0.07$	$(1.20 \pm 0.11)\%$	$(2.32 \pm 0.05)\%$	0.52 ± 0.05
$\chi^2_{\mathrm{strip}} > 10$	$(4.66 \pm 0.28)\%$	$(2.88 \pm 0.06)\%$	1.62 ± 0.10

Table 39: The ratio of 'anti-electrons' to candidate electrons for different anti-electron definitions in $Z \to e^+e^-$ data and CdfSim. The number of 'anti-electrons' in $Z \to e^+e^-$ events is found by requiring one of the electron legs to pass all the standard electron ID cuts and counting the number of events where the other electron is an 'anti-electron'. This number is then divided by the number of candidate electrons in the $Z \to e^+e^-$ sample (i.e. twice the number of candidate events.) The ratio found in the data is corrected to take into account residual background in the 'anti-electron' sample. Any excess in the number of 'anti-electron' events that have same-sign charge electrons in the data with respect to CdfSim is taken as the number of background events and a 100% uncertainty is attributed to this number.

Anti-electron definition	background
Standard	$(1.35 \pm 0.01_{\mathrm{STAT}} \pm 0.17_{\mathrm{EWK}})\%$
$\mathrm{E_{had}/E_{em}} > 0.07$	$(1.49 \pm 0.01_{\mathrm{STAT}} \pm 0.14_{\mathrm{EWK}})\%$
$\chi^2_{\mathrm{strip}} > 10$	$(1.13 \pm 0.01_{\mathrm{STAT}} \pm 0.17_{\mathrm{EWK}})\%$

Table 40: The multi-jet background obtained from different 'anti-electron' definitions. The uncertainties are from the statistical fit uncertainty and from the amount of electroweak contamination in the 'anti-electron' sample.

It is possible that the 'anti-electron' cuts bias the $\not\!\!E_T$ distribution in multi-jet events. In order to account for this bias the multi-jet sample is obtained by varying the 'anti-electron' definition and the fitting procedure is repeated. The 'anti-electron' definition is changed by applying each of the 'anti-electron' cuts, except Δz, in turn. The Δz cut is not used due to low statistics. Table 39 shows the correction to the number of electroweak events in the 'anti-electron' sample for the different 'anti-electron' definitions obtained, as described above, from $Z \to e^+e^-$ events. Table 40 shows the obtained fitted background for the different 'anti-electron' definitions. The largest deviation on the obtained background comes from applying the χ^2_{strip} 'anti-electron' cut. This 0.22% difference is taken as a systematic uncertainty on the background.

Systematic uncertainties on the background are found from :

1. The uncertainty on the amount of electroweak contamination in the 'anti-electron' sample: $\pm$ 0.17%.

2. Varying the cuts used to obtain the 'anti-electron' sample: $\pm$ 0.22%.

3. Using CdfSim instead of the fast simulation to get the $\not\!\!E_T$ distribution in signal events: $\pm$ 0.01%

4. The relaxation of the M_T cut when fitting to the $\not\!\!E_T$ distribution. There are 0.05% more events in the W $\rightarrow$ eν data when the 50 GeV M_T mass cut is relaxed, which is taken as a systematic on the background estimation: 0.05%

The measured multi-jet background is therefore (1.35 ± 0.26)%.

As well as measuring a value of the fractional multi-jet background in W $\rightarrow$ eν events, it is also necessary to obtain the M_T distribution. A modified 'anti-electron' sample is used to get the M_T distribution, where an additional cut, E/p < 3, is applied. This is because multi-jet events in the very high E/p tail have a different M_T distribution. Figure 69(a) shows the 'anti-electron' M_T distribution, which has been corrected for contamination from electroweak events. The distribution has been fitted with a Gaussian in the region $50 < M_T < 70$ GeV and a Landau in the region $70 < M_T < 200$ GeV. The 'anti-electron' cuts are varied to investigate any biases on M_T due to the reversed cuts. Figure 69(b) shows the M_T fitted function for multi-jet events selected with different 'anti-electron' cuts. The biggest difference in M_T comes from the distribution obtained by reversing the $\mathrm{E_{had}/E_{em}}$ cut. this difference is taken as a systematic uncertainty. Uncertainties on the M_T distribution come from :

1. Using different 'anti-electron' cuts to select the multi-jet sample.

2. Varying the amount of electroweak contamination within its uncertainty obtained from Z $\rightarrow e^+e^-$ events.

3. Varying the fit parameters within their uncertainties.

Table 41 summarises these uncertainties for the different $\Delta\Gamma_W$ fit ranges.

M_T^{cut} [GeV]	$\Delta\Gamma_W^{\text{norm}}$	$\Delta\Gamma_W^{M_T}$[fit pars]	$\Delta\Gamma_W^{M_T}$[EWK]	$\Delta\Gamma_W^{M_T}$[anti-ele]	$\Delta\Gamma_W$[total]
80	11 MeV	14 MeV	5 MeV	25 MeV	31 MeV
85	11 MeV	14 MeV	5 MeV	25 MeV	31 MeV
90	15 MeV	16 MeV	6 MeV	22 MeV	32 MeV
100	22 MeV	21 MeV	12 MeV	25 MeV	41 MeV
110	26 MeV	27 MeV	10 MeV	30 MeV	49 MeV

Table 41: Systematic uncertainties on Γ_W due to the multi-jet background.

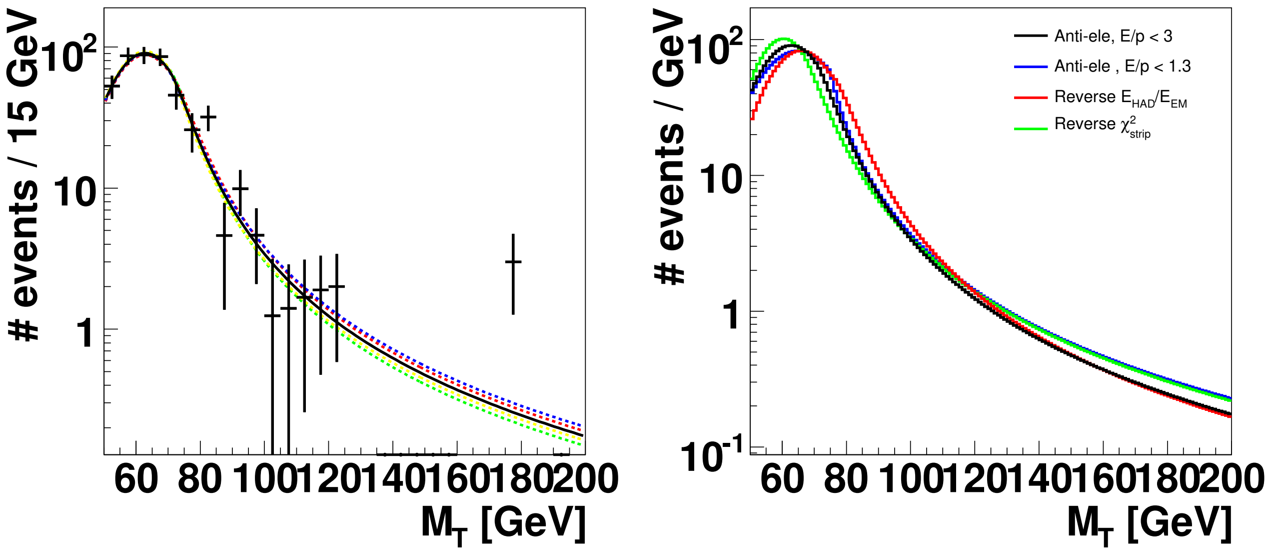

(a) (b)

Figure 69: (a): The multi-jet M_T distribution obtained from the 'anti-electron' sample, corrected for electroweak contamination. The histogram is fitted with a functional form consisting of a Gaussian in the region $50 < M_T < 70$ GeV and a Landau in the region $70 < M_T < 200$ GeV. The dashed lines show the variation in M_T when the Landau parameters are varied within their uncertainties (b): The M_T fitted function for different 'anti-electron' cuts.

12.6 Backgrounds: Summary

The number of background events in both the muon and electron decay channels are summarised in Table 42 for the total event sample as well as the fit region 90 < M_T< 200 GeV. Figure 70 shows the M_T distributions for all the backgrounds in both channels.

Channel	W $\rightarrow \mu\nu$		W $\rightarrow e\nu$	
M_T region	50 - 200	90 - 200	50 - 200	90 - 200
Events	108808	2619	127432	3426
W $\rightarrow \tau\nu$	2021	17	2557	21
Z $\rightarrow \ell^+\ell^-$	6003	216	205	17
Z $\rightarrow \tau^+\tau^-$	115	2	151	3
Multi-jet	291	10	1680	99
decay in-flight	145	40		

Table 42: The number of background events in the total event sample and the fit region for W $\rightarrow \mu\nu$ and W $\rightarrow e\nu$ events.

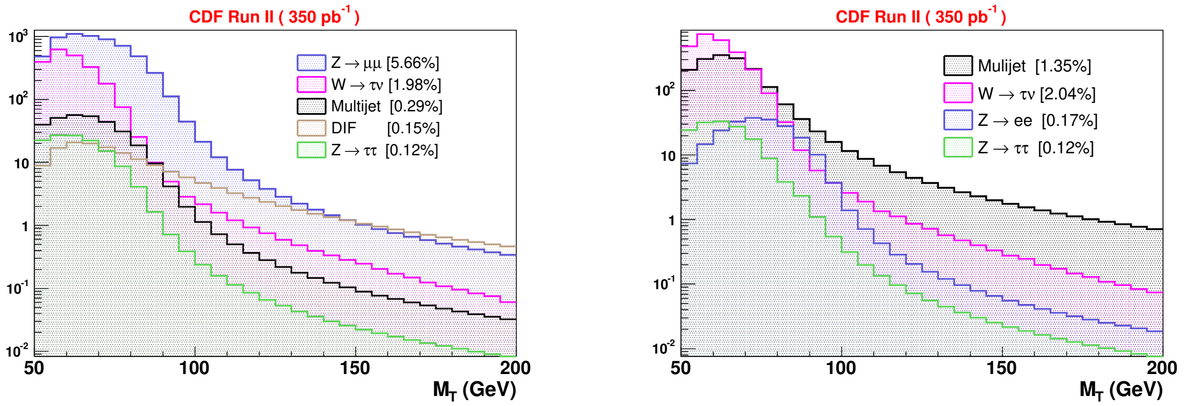

(a) (b)

Figure 70: The M_T distribution of backgrounds in (a) W $\rightarrow \mu\nu$ events and (b) W $\rightarrow e\nu$ events.

13 W Mass

The uncertainty on Γ_W due to the value of the W mass used as an input to the fast simulation is found by varying the inputted mass by its experimental uncertainty: 26 MeV [46]. The uncertainties are summarised in Table 43 for the different fit regions.

M_T^{cut} [GeV]	$\Delta\Gamma_W[M_W]$
80	18 MeV
85	17 MeV
90	9 MeV
100	4 MeV
110	2 MeV

Table 43: Systematic uncertainties on Γ_W due to the inputted W mass.

14 Summary of Systematic Uncertainties

The systematic uncertainties that have been calculated in the preceding chapters are summarised in Table 44 for the different fit regions. The statistical uncertainty obtained from the binned maximum-likelihood fits for Γ_W is also shown and the total uncertainty is calculated. The value $M_T^{\text{cut}} = 90$ GeV gives the smallest total uncertainty for both the electron and muon channels and therefore this is used for Γ_W fits.

		electron					muon				
M_T^{cut} [GeV]		80	85	90	100	110	80	85	90	100	110
PDF		21	22	20	21	26	21	23	20	23	27
Lepton ID		13	13	10	8	8	7	7	6	2	1
Acceptance		3	3	3	3	3	4	4	4	4	4
Backgrounds	$Z \to \ell^+\ell^-$	0	0	0	0	0	16	17	14	5	3
	$W \to \tau\nu$	3	3	3	5	8	0	0	0	0	0
	multi-jet	31	31	32	41	49	7	8	12	17	21
	decay in-flight						18	22	27	40	57
momentum	scale						29	27	17	8	5
	resolution						29	27	21	11	5
	non-Gaussian						17	17	16	13	10
calorimeter	scale	29	27	17	7	4					
	resolution	46	43	31	11	4					
	non-linearity	12	13	12	10	6					
	material scale	3	3	2	1	0					
	simulation	13	13	13	13	13					
Electroweak		15	14	10	6	6	4	6	6	6	6
Recoil		60	59	54	38	19	53	51	49	30	14
W p_T		8	8	7	7	6	8	8	7	7	6
W mass		18	17	9	4	2	18	17	9	4	2
statistics		54	54	60	78	103	60	61	67	90	116
total		110	107	99	101	120	100	99	98	109	135

Table 44: Systematic and statistical uncertainties on Γ_W for the electron and muon channels for five different fit ranges [MeV].

15 Fit Results

The W width is extracted from a binned maximum-likelihood fit to the M_T distribution in the region 90–200 GeV. Background distributions are added to the Monte Carlo templates, which are then normalised to the data in the region 50–90 GeV. Figures 71(a) and 71(b) show the Γ_W fits in the muon and electron channels respectively. We obtain the following results :

$$1948 \pm 67_{\mathrm{STAT}} \pm 79_{\mathrm{SYST}} \text{ MeV} \tag{31}$$

and

$$2118 \pm 60_{\mathrm{STAT}} \pm 71_{\mathrm{SYST}} \text{ MeV} \tag{32}$$

for muons and electrons respectively. We use the Best-Linear-Unbiased-Estimator (BLUE) method [47] to combine these results and obtain the final result :

$$2032 \pm 73 \text{ MeV} \quad . \tag{33}$$

This combination yields a χ^2 of 1.6 which gives a probability of 20% that the two channels are compatible. This result is in good agreement with the Standard Model prediction of 2093 $\pm$ 2 MeV[1] as well as the current world average of direct measurements: 2147 $\pm$ 60 MeV[48]. This is the world's best single direct width measurement. The uncertainty of 73 MeV can be compared with the combined LEP2 result which has an uncertainty of 80 MeV.

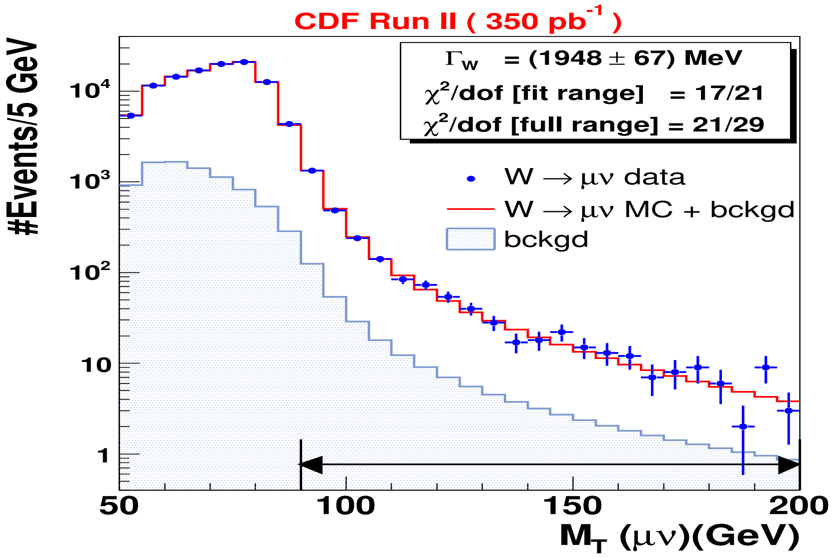

(a)

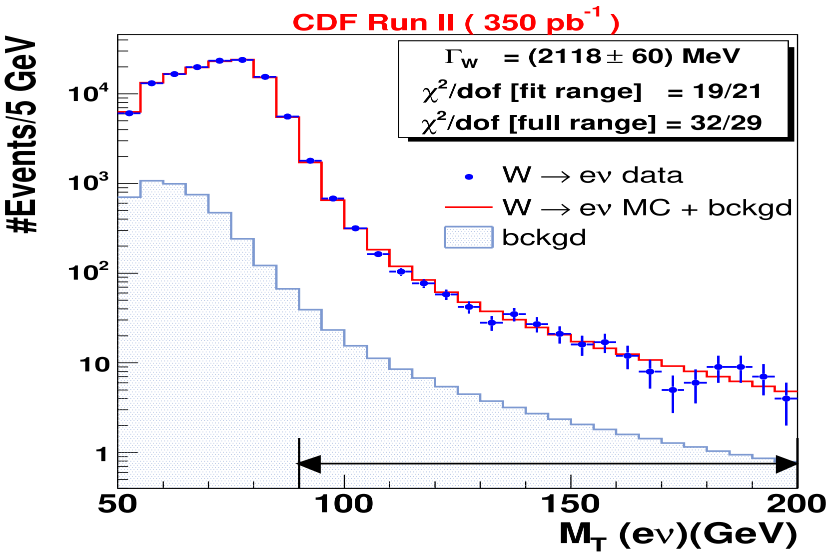

(b)

Figure 71: The M_T fits for the Γ_W for (a) W $\rightarrow \mu\nu$ and (b) W $\rightarrow e\nu$. The arrow indicates the fit region.

16 Cross-checks

16.1 Vary M_T Fit Region

As a cross-check the fits are done for different values of M_T^{cut}. The expected statistical fluctuation in the fitted Γ_W value is found from 225 Monte Carlo pseudo-experiments where Monte Carlo 'data' histograms are made with the same number of events as the data samples. The expected systematic shift from the uncertainty in the recoil parameters is found by sampling the recoil parameter covariance matrix 250 times (as explained in Section 11) and plotting the difference in the fitted Γ_W for the different M_T^{cut} values. This distribution is then fitted with a Gaussian and the width of the Gaussian is taken as the expected shift. The expected systematic shift from the rest of the systematic effects is found by taking the difference between the systematic uncertainty for each M_T^{cut} pair. Tables 45 and 46 summarise the expected shifts as well as the shifts observed in the data and the significance of the shift for electrons and muons respectively.

M_T^{cut} pair	stat	syst recoil	syst other	total	observed	sigma
80 vs 90	25	12	20	34	51	1.5
80 vs 100	54	27	42	74	26	0.4
80 vs 110	91	38	59	115	22	0.2
90 vs 100	55	20	23	63	24	0.4
90 vs 110	79	41	41	98	72	0.7
100 vs 110	62	17	20	67	48	0.7

Table 45: Expected and observed shifts in width from different fit regions (W $\rightarrow \mu\nu$).

M_T^{cut} pair	stat	syst recoil	syst other	total	observed	sigma
80 vs 90	22	15	23	36	35	1.0
80 vs 100	55	36	47	82	171	2.1
80 vs 110	83	50	58	113	186	1.6
90 vs 100	56	24	26	66	136	2.1
90 vs 110	78	39	38	95	151	1.6
100 vs 110	54	22	13	60	15	0.3

Table 46: Expected and observed shifts in width from different fit regions (W $\rightarrow$ eν).

16.2 W Mass Fits

As a cross check we perform fits for the W mass to the M_T distribution in the region $65 < M_T < 100$ GeV. We obtain the following results :

$$80410 \pm 39_{\mathrm{STAT}} \text{ MeV} \tag{34}$$

and

$$80463 \pm 37_{\mathrm{STAT}} \text{ MeV} \tag{35}$$

for $\mathrm{W} \rightarrow \mu\nu$ and $\mathrm{W} \rightarrow \mathrm{e}\nu$ respectively. This can be compared to the current world average 80398 ± 25 MeV. Both numbers are consistent with each other and with the world average at the 1.5σ level with only the statistical uncertainties considered.

16.3 Charge Splits

Detector biases may affect positively and negatively charged leptons differently. The width fits are therefore performed for the two sub-samples separately. The results are shown in Table 47, they are compatible in both the electron and muon channels.

	Negative charge Γ_W	Positive charge Γ_W	σ
$\mathrm{W} \rightarrow \mathrm{e}\nu$	$2130 \pm 86_{\mathrm{STAT}}$ MeV	$2107 \pm 86_{\mathrm{STAT}}$ MeV	0.2
$\mathrm{W} \rightarrow \mu\nu$	$1910 \pm 93_{\mathrm{STAT}}$ MeV	$1989 \pm 97_{\mathrm{STAT}}$ MeV	0.6

Table 47: Fitted Γ_W for negatively and positively charged leptons separately and the σ difference between the two using statistical uncertainties only.

16.4 Charged Lepton p_T and $\not{E}_T$ Fits

As a cross check of the fits to the M_T distribution, fits for Γ_W to the charged lepton p_T and the $\not{E}_T$ are also performed. The best fitting distributions compared to the data are shown in Figures 72 and 73 for the p_T and $\not{E}_T$ fits respectively.

The p_T fits yield $2024 \pm 95_{\mathrm{STAT}}$ MeV and $2068 \pm 83_{\mathrm{STAT}}$ MeV in the muon and electron channels respectively. These results respectively have a 31% and 22% probability of being compatible with the M_T fits. This probability is obtained (using the BLUE method) from the expected statistical deviations only, which are found from Monte Carlo pseudo-experiments so that the correlations are treated properly. Since only statistical uncertainties are considered, this is an under-estimate of the true probability as the systematic uncertainties for the M_T and p_T fits have some un-correlated components.

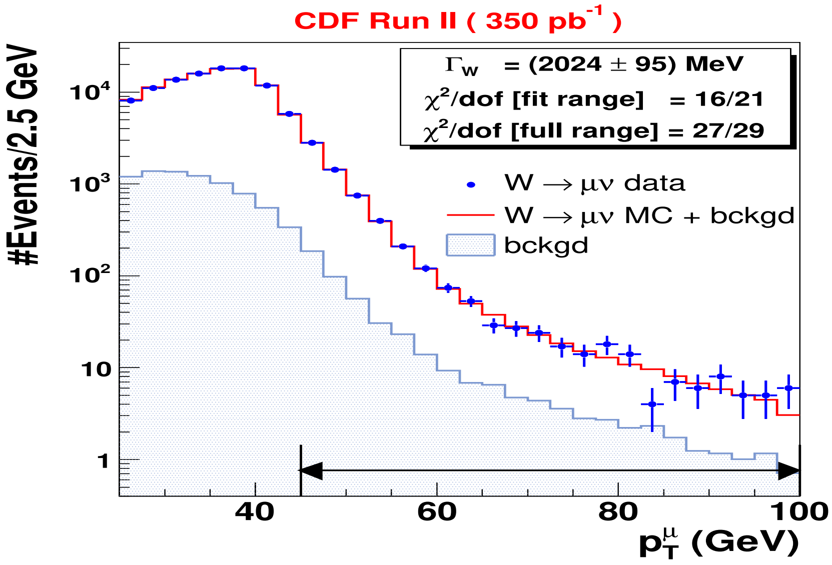

(a)

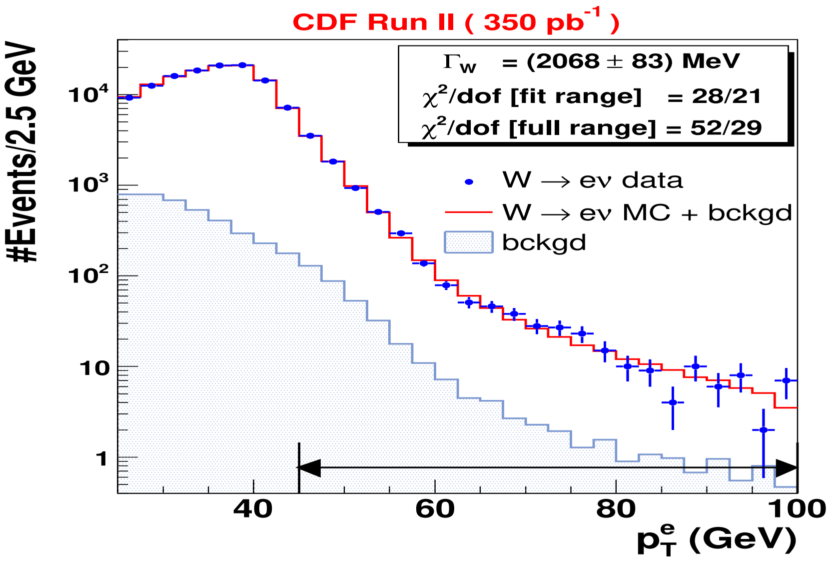

(b)

Figure 72: The p_T fits for the Γ_W for (a) W $\rightarrow \mu\nu$ and (b) W $\rightarrow e\nu$. The arrow indicates the fit region.

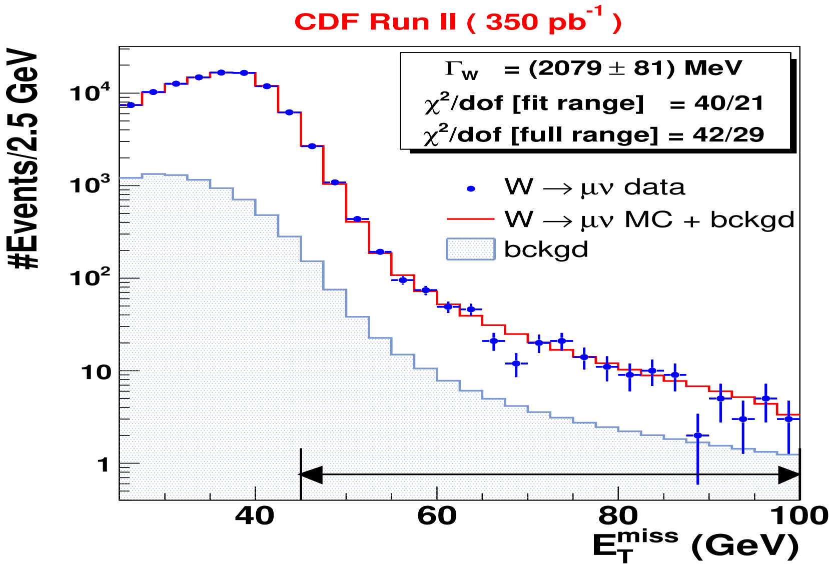

(a)

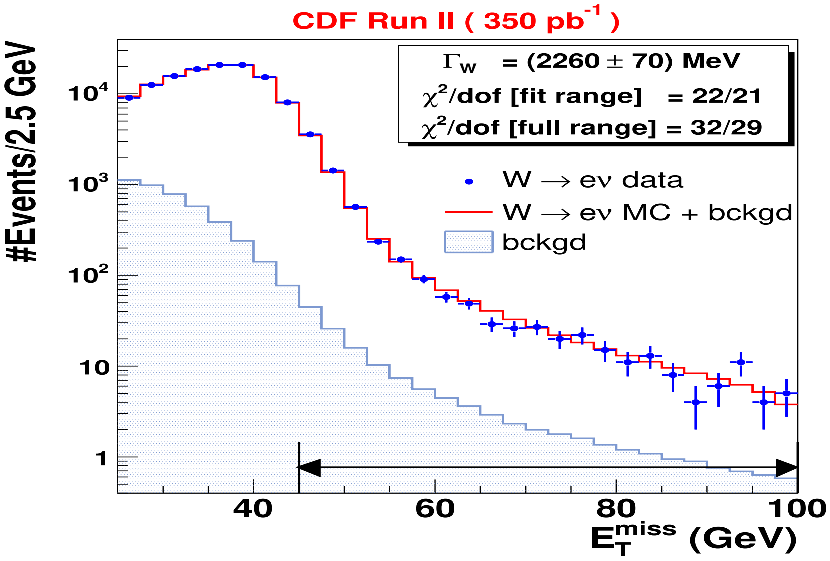

(b)

Figure 73: The $\not\!\!E_T$ fits for the Γ_W for (a) W $\rightarrow \mu\nu$ and (b) W $\rightarrow e\nu$. The arrow indicates the fit region.

The $\not\!\!E_T$ fits yield $2079 \pm 81_{\mathrm{STAT}} \pm 56_{\mathrm{RECOIL}}$ MeV and $2260 \pm 70_{\mathrm{STAT}} \pm 62_{\mathrm{RECOIL}}$ MeV in the muon and electron channels respectively. These results respectively have a 10% and 9% probability of being compatible with the M_T fits. This probability is obtained from the expected statistical and recoil error deviations only, which are found from Monte Carlo pseudo-experiments. This is therefore an under-estimate of the true probability since the other systematic uncertainties for the M_T and $\not\!\!E_T$ fits have some un-correlated components.

References

[1] W.-M. Yao *et al.*, J. Phys. G **33** (2006) 1 (PDG-2006)

[2] Anyes Taffard, CDF-NOTE-6255 (2003).

[3] UA1 collaboration.

[4] F.A. Berends, R. Kleiss, J.P. Revol, J.P. Vialle, Z. Phys. C **27** 155 (1985); F.A. Berends, R. Kleiss, Z. Phys. C **27** 365 (1985).

[5] J. Pumplin, D. R. Stump, J. Huston, H. L. Lai, P. Nadolsky and W. K. Tung, JHEP **0207** (2002) 012.

[6] A. D. Martin, R. G. Roberts, W. J. Stirling and R. S. Thorne, Eur. Phys. J. C **4** (1998) 463.

[7] J. M. Campbell, J. W. Huston, and W. J. Stirling, Rep. Prog. Phys. **70**, 89 (2007).

[8] A. D. Martin, R. G. Roberts, W. J. Stirling and R. S. Thorne, Phys. Lett. B **604**, 61 (2004) [arXiv:hep-ph/0410230].

[9] E. Barberio, Z. Was, Comput. Phys. Comm. **79** 291 (1994); E. Barberio, B. van Eijik, Z. Was, Compu. Phys. Comm.**66** 115 (1991).

[10] U. Baur and D. Wackeroth, Phys. Rev. D **70**, 073015 (2004).

[11] C. Balazs, C.P. Yuan, Phys. Rev. D56, 5558 (1997).

[12] F. Landry, R. Brock, P. M. Nadolsky, and C. P. Yuan, Phys. Rev. D **67**, 073016 (2003).

[13] B. Abbott et al., Phys. Rev. D **61**, 032004 (2000).

[14] F. Abe et al., Phys. Rev. Lett. **67**, 2937 (1991)

[15] T. Affolder et al., Phys. Rev. Lett. **84**, 845 (2000).

[16] M. Lancaster, CDF-NOTE-4770 (1998).

[17] P.B. Arnold, R.P. Kauffman, Nucl. Phys. B **349** 38 (1991);
P.B. Arnold, M. Reno, Nucl. Phys. B **319** 37 (1989);
P.B. Arnold, M. Reno, R.K Ellis, Phys. Rev. D**40** 912 (1989)

[18] W.T. Giele, S. Keller, Phys. Rev. D **57**, 4433 (1998).

[19] W. K. Sakumoto, CDF-NOTE-7324 (2004).

[20] K. Rinnert, CDF-NOTE-5846 (2002).

[21] W.-M. Yao *et al.*, J. Phys. G **33** (2006) 1 (PDG-2006), Eq. 27.1.

[22] W.-M. Yao *et al.*, J. Phys. G **33** (2006) 1 (PDG-2006), Eq. 27.2.

[23] W.-M. Yao *et al.*, J. Phys. G **33** (2006) 1 (PDG-2006), Sec. 27.2.2; http://pdg.lbl.gov/AtomicNuclearProperties/substances/atomic_nuclear/muonloss_014.pdf .

[24] W.-M. Yao *et al.*, J. Phys. G **33** (2006) 1 (PDG-2006), Eq. 27.26.

[25] W.-M. Yao *et al.*, J. Phys. G **33** (2006) 1 (PDG-2006), Eq. 27.25.

[26] GEANT-3 manual, http://wwwasdoc.web.cern.ch/wwwasdoc/pdfdir/geant.pdf, p.253-254. Note that there are errors in the documentation and what is actually implemented is based on the GEANT-3 source code itself, subroutine `GDRELE`.

[27] W.-M. Yao *et al.*, J. Phys. G **33** (2006) 1 (PDG-2006), Eq. 27.28.

[28] W.-M. Yao *et al.*, J. Phys. G **33** (2006) 1 (PDG-2006), Eq. 27.27.

[29] K. Yasuoka *et al.*, "Response Maps of the CDF Central Electromagnetic Calorimeter with Electrons", Nucl. Instr. Meth. **A**267 (1988) 315.

[30] P. Fernandez, CDF-NOTE-8400, (2006). The E/p plots in Figure 3 are used to infer the hadronic calorimeter response.

[31] S. Klein, "Suppression of Bremsstrahlung and Pair Production due to Environmental Factors", Rev. Mod. Phys. **71** (1999) 1501; hep-ph/9802442.

[32] Cross section data for photons incident on silicon can be found at : http://physics.nist.gov/PhysRefData/Xcom/Text/XCOM.html .

[33] A description of the Klein-Nishina formula can be found at : http://geant4.web.cern.ch/geant4/UserDocumentation/UsersGuides/PhysicsReferenceManual/html/node26.html .

[34] Y. Ishizawa and J. Nielsen, CDF-NOTE-7401 (2005).

[35] D. Hoffman, Y. Kim, J. Nielsen, L. Tompkins, G. Veramendi, CDF-NOTE-6234 (2004).

[36] V. Martin, CDF-NOTE-7031 (2004).

[37] V. Martin, CDF-NOTE-7367 (2005).

[38] W. D. Dagenhart, CDF-NOTE-8471 (2006).

[39] J. Goldstein, S. Harper and P. Renton, CDF-NOTE-8062 (2006). The efficiency plots were kindly provided by Sam Harper using the method described in the above note.

[40] L. Nodulman, CDF-NOTE-6728 (2004).

[41] D. Amidei et al., CDF-NOTE-6681 (2004).

[42] L. Nodulman, CDF-NOTE-8425 (2006).

[43] P.M. Fernandez , CDF Note in preparation. Talk in simulation meeting, Sep 21st 2006.

[44] W. L. van Neerven and E. B. Zijlstra, Nucl. Phys. B **382** (1992) 11.

[45] C. Hays, private communication: CDF note in preparation.

[46] C. Hays, B. Jayatilaka, A. Kotwal, L. Nodulman, O. Stelzer-Chilton, W. Trischuk, I. Vollrath, CDF-NOTE-7104 (2006).

[47] L. Lyons, D.Gibaut, P.Clifford, Nucl. Instr. Meth. A **270**,110 (1988).

[48] hep-ex/0612034